TÜBİTAK

Turkish Journal of Earth Sciences

http://journals.tubitak.gov.tr/earth/

Research Article

Turkish J Earth Sci
(2013) 22: 32-60
© TÜBİTAK
doi:10.3906/yer-1104-9

Magmatic processes at the volcanic front of Central Mexican Volcanic Belt: Sierra de Chichinautzin Volcanic Field (Mexico)

Fernando VELASCO-TAPIA[1,*], Surendra P. VERMA[2]

[1]Facultad de Ciencias de la Tierra, Universidad Autónoma de Nuevo León, Ex-Hacienda de Guadalupe, Carretera Linares-Cerro Prieto km 8, Linares, N.L., 67700, Mexico

[2]Departamento de Sistemas Energéticos, Centro de Investigación en Energía, Universidad Nacional Autónoma de México, Privada Xochicalco s/n, Col. Centro, Temixco, Mor., 62580, Mexico

Received: 18.04.2010 • **Accepted:** 27.05.2011 • **Published Online:** 04.01.2013 • **Printed:** 25.01.2013

Abstract: The Sierra de Chichinautzin (SCN) volcanic field is considered one of the key areas to understand the complex petrogenetic processes at the volcanic front of the Mexican Volcanic Belt (MVB). New as well as published major- and trace-element and Sr and Nd isotopic data are used to constrain the magma generation and evolution processes in the SCN. From inverse and direct modelling, combined $^{87}Sr/^{86}Sr$ and $^{143}Nd/^{144}Nd$ data, and use of multi-dimensional log-ratio discriminant function based diagrams and other geological and geophysical considerations, we infer that mafic magmas from the SCN were generated by partial melting of continental lithospheric mantle in an extensional setting. Inverse modelling of primary magmas from the SCN further indicates that the source region is not depleted in high-field strength elements (HFSE) compared to large ion lithophile elements (LILE) and rare-earth elements (REE). The petrogenesis of evolved magmas from the SCN is consistent with the partial melting of the continental crust facilitated by influx of mantle-derived magmas. Generally, an extensional setting is indicated for the SCN despite continuing subduction at the Middle America Trench.

Key Words: geochemistry, subduction, extension, multi-dimensional discrimination diagrams, isotopes, inverse modelling, direct modelling

1. Introduction

The theory of plate tectonics has provided a framework for the study of the different styles and geochemical characteristics of past and present igneous activity (Stock 1996; Kearey *et al.* 2009). At least four distinct tectonic environments have been established in which magmas may be generated. These are: (a) destructive plate margin setting (island and continental arcs), (b) continental intra-plate setting (extensional and rift zones), (c) oceanic intra-plate setting (ocean islands), and (d) constructive plate margin setting (mid-ocean ridges and back-arc spreading centres). However, despite deviations from the conventional rigid plate hypothesis (vertical motions, deformation in plate interiors or limitations on the sizes of plates; Stock 1996; Keith 2001), an unambiguous petrogenetic-tectonic model, though very much needed, is difficult to establish in tectonically complex zones, such as the Mexican Volcanic Belt (MVB, Figure 1).

The MVB is a major province, about 1000 km long and 50–300 km wide, of Miocene to present-day volcanism in southern Mexico (e.g., Robin 1982; Gómez-Tuena *et al.* 2007a). It has also been called a large igneous province (LIP, Sheth 2007). It comprises more than 8000 individual volcanic structures, including stratovolcanoes, monogenetic cone fields, domes and calderas (Robin 1982). Uniquely, the MVB is oriented at an angle of about 15–20° with respect to the Middle America Trench (MAT, Figure 1, Molnar & Sykes 1969). In particular, in the central MVB (C-MVB) continuing subduction of the Cocos oceanic plate under the North American continental plate and the subalkaline character of most of the lavas, a classic subduction-related magmatic arc model has been suggested as appropriate. However, several geological, geophysical and geochemical features of the C-MVB pose problems with this simple model and have motivated a debate about the magma genesis and origin of this controversial magmatic province (e.g., Shurbet & Cebull 1984; Márquez *et al.* 1999a; Verma 1999, 2000, 2002, 2004, 2009; Sheth *et al.* 2000; Ferrari *et al.* 2001; Ferrari 2004; Blatter *et al.* 2007; Mori *et al.* 2009).

A basic problem of the subduction hypothesis is related to the lack of a well-defined Wadati-Benioff zone (Pacheco

* Correspondence: velasco@fct.uanl.mx

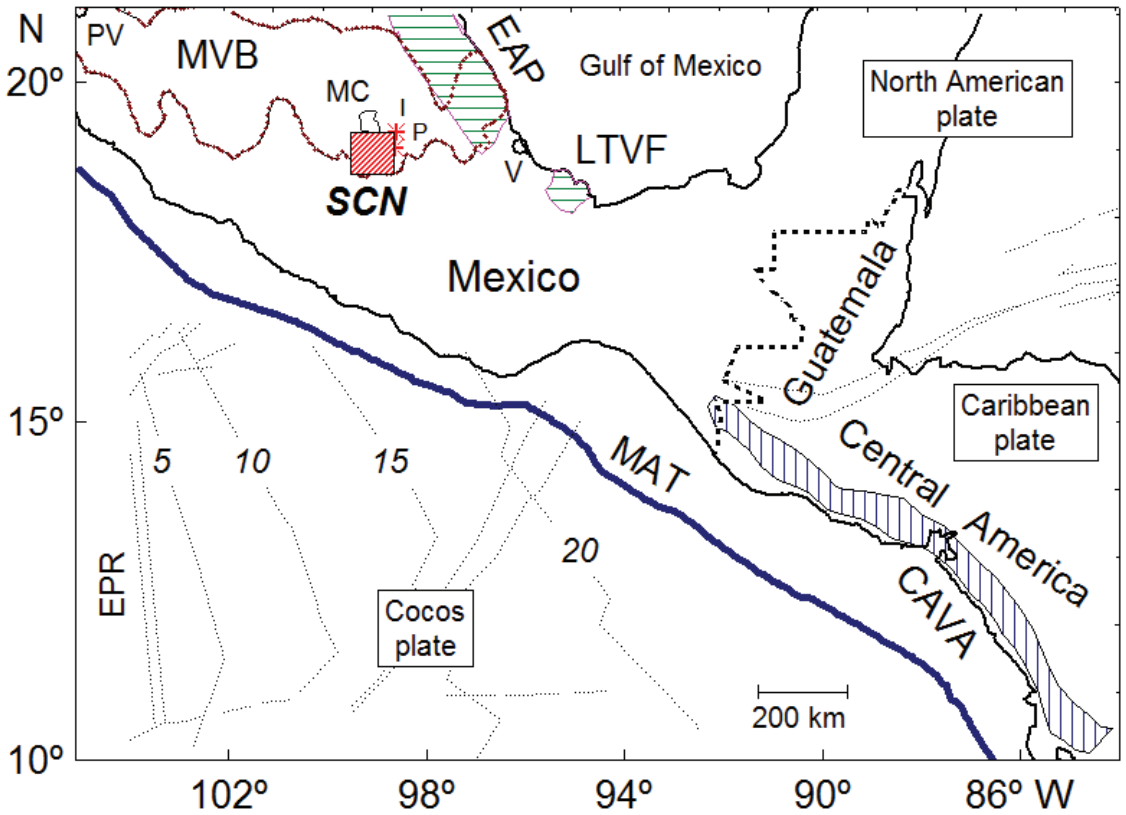

Figure 1. Location of the Sierra de Chichinautzin (SCN) volcanic field at the volcanic front of the central part of the Mexican Volcanic Belt (MVB). This Figure (modified from Verma 2002) also includes the approximate location of the Eastern Alkaline Province (EAP), Los Tuxtlas Volcanic Field (LTVF), and Central American Volcanic Arc (CAVA). Other tectonic features are the Middle America Trench (MAT, shown by a thick blue curve) and the East Pacific Rise (EPR, shown by a pair of dashed-dotted black lines). The traces marked by numbers 5 to 20 on the oceanic Cocos plate give the approximate age of the oceanic plate in Ma. Locations of Iztaccíhuatl (I) and Popocatépetl stratovolcanoes (P; from which crustal xenoliths were analysed by Schaaf *et al.* 2005), are also shown. Cities are: PV– Puerto Vallarta, MC– Mexico City, and V– Veracruz.

& Singh 2010 and references therein). The volcanic front of the C-MVB is about 300 km from the MAT (Verma 2009) whereas, in spite of numerous attempts and a very dense seismic network, the subducted Cocos plate is seismically poorly defined beyond the Pacific coast of Mexico and can only be traced to about 40 km depth at a distance of about 240 km from the trench (Pacheco & Singh 2010). Thus, the presence of the subducted slab can only be inferred from the MAT up to about 60 km away from the C-MVB volcanic front. Recently, subhorizontal subduction has been inferred by Pérez-Campos *et al.* (2008), Husker & Davis (2009), and Pacheco & Singh (2010) from seismic data obtained from a dense network. The quasi-horizontal subduction and a very shallow subducted slab (at most at about 40 km depth; Figure 5 in Pacheco & Singh 2010) are not thermodynamically favourable conditions for magma generation (Tatsumi & Eggins 1993). Husker & Davis (2009) assumed a slab temperature model to interpret the seismic data and inferred tomography and thermal state of the Cocos plate, meaning that the results from this circular argument, especially the thermal regime, would depend directly on the basic assumptions. Futhermore, these authors ignored the geochemical and isotopic constraints for basic magmas from the C-MVB (e.g., Verma 1999, 2000, 2002, 2004; Velasco-Tapia & Verma 2001a, b). Similarly, Pérez-Campos *et al.* (2008) did not take into consideration these geochemical and isotopic constraints in their geological interpretation of the seismic data.

The diminution or even cessation of arc-related volcanism observed in the south-central Andes has been related to subhorizontal subduction of the Nazca plate (Kay *et al.* 1987; Martinod *et al.* 2010). Steeper subduction angles are commonly observed in many arcs (Doglioni *et al.* 2007; Schellart 2007). For example, average slab

dip angles in the Tonga, Kermadec, New Hebrides and Marianas arcs vary from about 50° to almost 90° (Schellart 2005).

Unlike the south-central Andes and in spite of the peculiarities of subhorizontal subduction and an undefined Benioff zone, widespread volcanism occurs along the entire MVB. Extrapolation of the subducted Cocos plate to greater depths, without any solid seismic evidence, was proposed to overcome this problem (Pardo & Suárez 1995; Pérez-Campos *et al.* 2008), although this solution has already been criticized in the literature (Sheth *et al* 2000; Verma 2009). The slab is imagined to be broken and to plunge vertically into the mantle and, interestingly, it is done artificially, without any direct seismic evidence, after bringing it close to the volcanic front of the C-MVB (Pérez-Campos *et al.* 2008; Husker & Davis 2009).

In a magnetotelluric study of southern Mexico (two-dimensional inversion) by Jödicke *et al.* (2006), fluid release from the subhorizontal subducted Cocos plate and consequent partial melting of the crust beneath the MVB were inferred to explain the volcanism. Several questions remain to be answered, such as the inadequacy of a two-dimensional solution of a clearly three-dimensional Earth, which are as follows: (i) the assumption of the presence of subducted slab beneath the MVB without any seismic evidence; (ii) the release of subduction fluids from the plate at 40 km depth (this extremely shallow depth is now inferred by Pacheco & Singh 2010) and their subhorizontal travel through 60 km to the MVB volcanic front; and (iii) the inability of the magnetotelluric model to explain the presence of SCN mafic magmas presumably derived from the lithospheric mantle (Verma 2000, 2002, 2004; Velasco-Tapia & Verma 2001a, b). Why could the fluids not have originated either in the lithospheric mantle or in the continental crust, or both? Sheth *et al.* (2000) proposed that the mantle beneath the MVB is heterogeneous and contains kilometre-scale domains of vein-free peridotite and peridotite with veins of phlogopite or amphibole, or both phases, which could release the required fluids. This could be a more plausible model in the light of the most recent seismic evidence and interpretation (Pacheco & Singh 2010).

The study of mafic rocks located along the entire MVB has revealed rift-like isotopic and geochemical signatures, associated with partial melting of an upwelling heterogeneous mantle source and eruption of magma in an extensional setting with incipient or well-established rifting (e.g., Luhr *et al.* 1985, 1989; Verma 2009; Luhr 1997; Márquez *et al.* 2001; Velasco-Tapia & Verma 2001a, b). Alternative hypotheses also suggested to explain the origin of the MVB volcanism, include those related to a plume model (Moore *et al.* 1994; Márquez *et al.* 1999a), to extensional tectonics (Sheth *et al.* 2000; Márquez *et al.* 2001; Velasco-Tapia & Verma 2001a, b), or to detachment of the lower continental crust (Mori *et al.* 2009).

In this context, the Sierra de Chichinautzin volcanic field (SCN, Figure 2; Márquez *et al.* 1999a, b; Wallace & Carmichael 1999; Velasco-Tapia & Verma 2001a, b; Meriggi *et al.* 2008) represents one of the key areas in which to study the origin and evolution of the magmatism within the MVB for the following reasons: (1) the SCN marks the front of the central MVB (Figure 1) and, if the volcanism is related to subduction, the geochemistry of all rocks should display clear relationships with the subducted Cocos plate (see Verma 2009); (2) ^{14}C age determinations of palaeosols and organic matter interbedded between SCN volcanics have always given ages younger than 40,000 years (Velasco-Tapia & Verma 2001a) and consequently, the processes related to the origin of magmas could still be active beneath this area; (3) the geochemical and Sr, Nd, and Pb isotopic composition of the descending slab is known in this part of the trench from previous studies (Verma 2000); (4) new multi-dimensional tectonic discrimination diagrams based on log-ratio transformed variables with statistically correct methodology (Aitchison 1986) and linear discriminant analysis (LDA) are available for the discrimination of four main tectonic settings (see Verma 2010); and (5) a wide variety of magmas from basalt and trachybasalt to dacite and trachydacite exist (Velasco-Tapia & Verma 2001b), which enable us to investigate the geochemical and isotopic characteristics of the magmatic sources as well as processes controlling the magmatic evolution.

To improve our understanding of the processes controlling the origin of magmas in the SCN volcanic field, we compiled new as well as published geochemical and isotopic data on rocks that cover the compositional range observed in this monogenetic field. The compiled rocks were classified into different geochemical types applying the total-alkali versus silica (TAS) diagram (Le Bas *et al.* 1986) in the correct way, i.e., after adjusting Fe-oxidation ratio (Middlemost 1989) on an anhydrous basis and to 100 %m/m, and were grouped according to their phenocryst assemblages. We used our extensive geochemical and isotopic database to evaluate different petrological mechanisms for the origin and evolution of the diversity of SCN magmas. We also resorted to inverse modelling of primary magmas to establish the source characteristics, as well as direct modelling of all SCN magmas to infer the petrogenetic processes.

2. Sierra de Chichinautzin: geological setting

Several authors have described the stratigraphy (Cretaceous to Recent) and volcanic activity in the SCN and surrounding region (e.g., Martín del Pozzo 1982; Swinamer 1989; Vázquez-Sánchez & Jaimes-Palomera

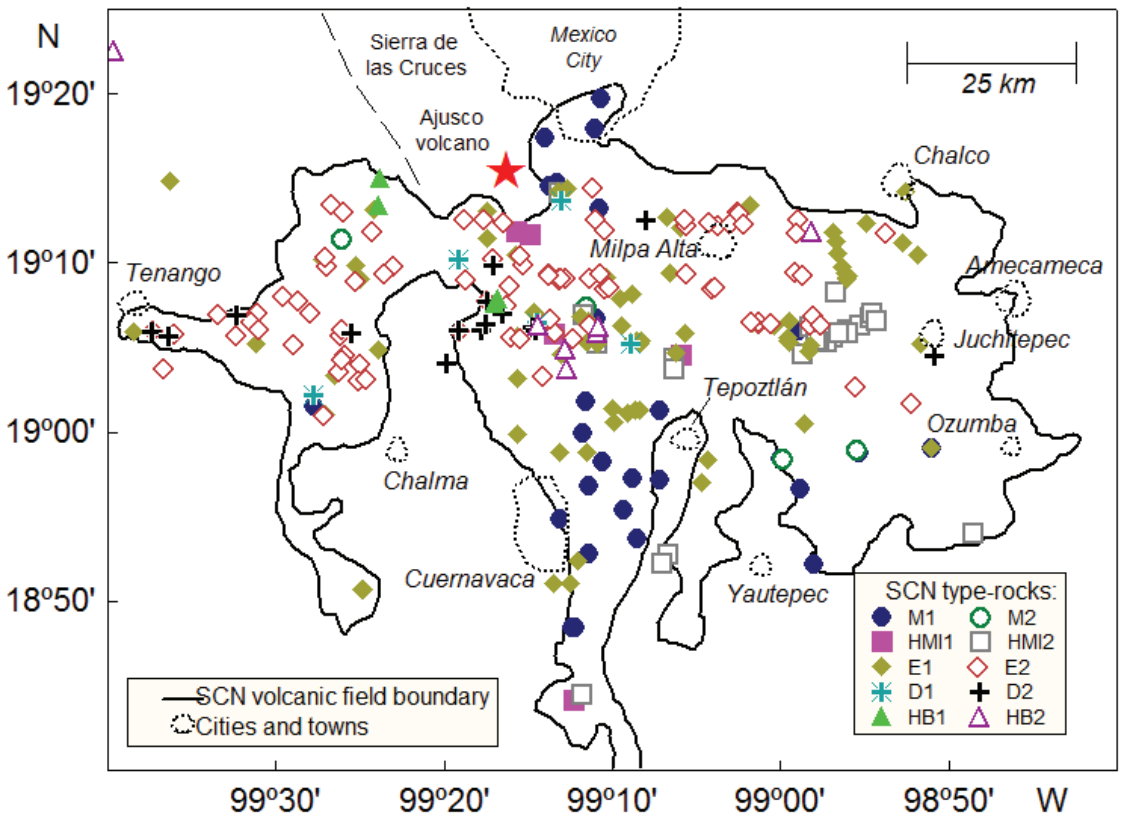

Figure 2. Trace of the Sierra de Chichinautzin (SCN) volcanic field and the schematic location of the sampling sites according to the petrographic and geochemical rock-types: *M1*– near primary mafic magmas; *M2*– mafic magmas evolved by fractional crystallisation; *E1*– evolved magmas with an ol + opx ± cpx ± plg mineralogical assemblage; *E2*– evolved magmas with an opx ± cpx + plg mineralogical assemblage; *HMI*– high magnesium intermediate magmas; *HB1*– high-Ba magma with low Nb; *HB2*– high-Ba magma with high Nb; *DISQ*– D1 and D2 magmas with abundant textural evidence of mineralogical disequilibrium. This Figure (modified from Verma 1999) also includes the approximate location of the Sierra de Las Cruces, Ajusco volcano, and important cities and towns in the area.

1989; Mooser *et al.* 1996; Márquez *et al.* 1999b; García-Palomo *et al.* 2000; Siebe *et al.* 2004; Meriggi *et al.* 2008).

A calcareous marine to shelf facies sequence was deposited in central Mexico during the Cretaceous (Fries 1960). Rocks from this sequence include massive limestone with black chert lenses, beds of gypsum, massive to thickly bedded limestones, greywacke interbedded with limonite and shale beds. This ~3000-m-thick Cretaceous sedimentary sequence was folded and uplifted during the Laramide orogenic event (Fries 1960) and later intruded by granitic or granodioritic dykes dated at 50±10 Ma (De Cserna *et al.* 1974). The Eocene–Oligocene stratigraphy that overlies the Cretaceous sequence consists of calcareous conglomerates, lava flows, sandstones, volcanic siltstones, and lacustrine deposits up to 500 m thick.

The sedimentary sequence is unconformably overlain by about 38 to 7.5 Ma rhyolite, rhyodacite, dacitic lava flows and pyroclastic flow deposits (Morán-Zenteno *et al.* 1998; García-Palomo *et al.* 2002), and by Pliocene to Holocene volcanism in Las Cruces, Ajusco and Chichinautzin (Delgado-Granados & Martin del Pozzo 1993). Late Pliocene to Early Pleistocene andesitic to dacitic flows and associated pyroclastic deposits of Las Cruces (Figure 2) are dated approximately at 3.6 to 1.8 Ma (Fries 1960; Sánchez-Rubio 1984; Mora Alvarez *et al.* 1991; Delgado-Granados & Martin del Pozzo 1993; Osete *et al.* 2000; García-Palomo *et al.* 2002). During the younger eruptive period, the Ajusco volcano (Figure 2) was formed by extrusion of several andesitic domes, one of which was dated at about 0.39 Ma (Mora Alvarez *et al.* 1991). Late Pleistocene–Holocene volcanic activity (<40,000 years; Bloomfield 1975; Córdova *et al.* 1994; Delgado *et al.* 1998; Velasco-Tapia & Verma 2001a) in central MVB has been named the Chichinautzin eruption period, characterised by monogenetic activity generating scoria cones and shield volcanoes with associated lava flows.

The SCN (Figure 2) comprises over 220 Quaternary monogenetic volcanic centres, covering approximately 2400 km^2 (98°40'–99°40'W, 18°30'–19°30'N; Márquez *et al.* 1999b). Summit elevations in the SCN reach ~3700 m compared with ~2200 m elevation in the southern sector of the Basin of Mexico and ~1500 m in the Cuernavaca Basin (Wallace & Carmichael 1999). Márquez *et al.* (1999b) pointed out that the SCN can be interpreted as the southernmost structural domain of a group of six parallel E–W-oriented tectonic structures, which show active N–S extension and a strike-slip component. The tectonic setting in the SCN has been confirmed, for example, by the analysis of focal mechanism of the Milpa Alta earthquake (very shallow depth of ~ 12 km), that was interpreted as an E–W normal faulting event with a significant (50%) sinistral strike-slip component (UNAM & CENAPRED Seismology Group 1995). Based on the interpretation of reflection seismic transects and detailed geologic mapping, Mooser *et al.* (1996) recognised an Oligocene basin crossing the SCN from N to S, called the Mixhuca basin. Additionally, these authors reported three other Pleistocene basins in the region (denominated by them from north to south as the Mexico, Tlalli-Santa Catarina and Chichinautzin-Izta-Malinche basins), with an inferred east–west orientation. These basins could represent a widespread manifestation of both E–W and N–S extension in the SCN area (Velasco-Tapia & Verma 2001b).

The central MVB is characterised by pervasive E–W normal faults with a left-lateral strike- slip component, some of which are seismically active (Johnson & Harrison 1990; Suter *et al.* 1992, 1995; Ego & Ansan 2002). Taking into account the geometry of regional graben-type structures, Márquez *et al.* (2001) suggested that extensional rates increase to the west. The tectonic scenario is complemented by active N–S to NNW-striking normal faults, related to the southern continuation of the Basin and Range Province (Henry & Aranda-Gomez 1992). The monogenetic volcanism in this part of the MVB appears to be related to E–W and N60°E-oriented extensional faults (Alaniz-Alvarez *et al.* 1998).

Extensional stress conditions in the SCN could provoke crustal weakening and facilitate the formation and eruption of monogenetic volcanoes. This model is consistent with geophysical observations indicating the existence of a low density (3.29 g/cm^3) and low velocity (Vp= 7.6 km/s) mantle layer at the base of the crust (at ~40 km depth) beneath the central MVB (Molina-Garza & Urrutia-Fucugauchi 1993; Campos-Enríquez & Sánchez-Zamora 2000). A pronounced gravity low is observed over the entire MVB, and especially beneath its central region (< –200 mGal Bouguer anomaly; Molina-Garza & Urrutia-Fucugauchi 1993). Consequently, several authors (Fix 1975; Gomberg & Masters 1988; Molina-Garza & Urrutia-Fucugauchi 1993) have suggested the existence of an anomalous low density, low velocity, partially molten mantle layer at the base of the crust (~40 km), being an atypical feature of continental arcs (Tatsumi & Eggins 1993). Additionally, Márquez *et al.* (2001) proposed a two-layer crustal stretching model (brittle and ductile domains) to explain the southward migration of volcanic activity. These layers are separated at an upper crustal level (depth ~10 km) by a zone of simple shear decoupling, at the brittle-ductile transition zone. The overall movement which occurs above this zone is southwards.

3. Analytical methods and results

SCN volcanic rocks were collected from outcrops or road-cuts, avoiding any possible alteration. Samples were jaw crushed and splits were pulverised in an agate bowl for geochemical analysis. Major elements were analysed in ten samples (Appendix A1)* by X-ray fluorescence spectrometry (XRF) at Laboratorio Universitario de Geoquímica Isotópica (LUGIS)–UNAM. These measurements were carried out on fused glass discs using a Siemens sequential XRF SRS 3000 (with a Rh tube and 125 mm Be window) equipment. Sample preparation, measuring conditions, and other details about the calibration curves (applying a regression model considering errors on both axes) and precision and accuracy estimates were reported by Guevara *et al.* (2005). Precision for major elements ranged between 0.5 and 5%. Sixteen different geochemical reference materials (GRM) were run to assess the analytical accuracy, providing results within 1–10% of GRM recommended values.

Additionally, the major and trace element compositions of other twenty-five samples (Appendix A1 and A2) were determined by ActLabs laboratories, Canada, following the '4 LithoRes' methodology. The sample was fused using a lithium metaborate-tetraborate mixture. The melt produced by this process was completely dissolved with 5% HNO_3. Major elements were analysed in the resulting solution by inductively coupled plasma-optical emission spectrometry (ICP-OES), with an analytical accuracy of <6%. Trace element analyses were done by inductively coupled plasma-mass spectrometry (ICP-MS). The analytical reproducibility ranged between 5 and 12%.

Sr and Nd isotope analyses (Appendix A3) were performed at Laboratorio Universitario de Geoquímica Isotópica (LUGIS)–Universidad Nacional Autónoma de México. Analyses were carried out on a Finnigan MAT-262 thermal ionisation mass spectrometer (TIMS). Repeated analyses of SRM987 Sr standard (n= 208) and La Jolla Nd standard (n= 105) gave average values of 0.710233±17 and 0.511880±21, respectively. The analytical errors for $^{87}Sr/^{86}Sr$ and $^{143}Nd/^{144}Nd$ measured ratios are directly quoted for each sample (Appendix A3).

* The appendices can be found at http://journals.tubitak.gov.tr/earth/issues/yer-13-22-1/yer-22-1-2-1104-9.pdf

Analytical data for minerals were obtained from thin-sections of selected samples, using the WDS JXA-8900 JEOL microprobe system of Centro de Microscopía Electrónica, Universidad Complutense de Madrid, Spain (Appendix A4–10). The experimental conditions were 15 kV and 20 nA, for establishing an electronic beam of ~1 mm. The apparent concentrations were automatically corrected for atomic number (Z), absorption (A), and fluorescence (F) effects internally in the ZAFJEOL software. The calibration of the microprobe system was carried out using reference minerals from the Smithsonian Institution (Jarosewich *et al.* 1980). The analytical accuracy was ~2% on average for each analysis.

The structural formula for each analysed mineral was estimated following a standard procedure that includes the calculation of atomic proportions of each element and the distribution of these proportions among the available sites in the silicate structure, with fixed number of oxygens (Deer *et al.* 1997). The problem of estimating Fe^{+3} content in spinels was solved by applying the stoichiometric criteria proposed by Droop (1987). Pyroxene and amphibole structural formulae were calculated using the computer programs developed by Yavuz (1999, 2001). However, compositional contrasts from core to rim were studied in zoned crystals by means of profile analysis and scanning probe microanalysis (SEM) images.

4. Database and initial data handling

New geochemical (major and trace element data; Appendix A1 and A2) and isotopic data (Appendix A3) for magmas from the SCN were compiled. Also included were data for mafic and evolved magmas reported previously by Swinamer (1989), Rodríguez Lara (1997), Delgado *et al.* (1998), Wallace & Carmichael (1999), Verma (1999, 2000), Velasco-Tapia & Verma (2001b), García-Palomo *et al.* (2002), Martínez-Serrano *et al.* (2004), and Siebe *et al.* (2004). Thus, the database included information on 289 samples from the SCN.

Similarly, major and trace element data were also compiled for the Central American Volcanic Arc (CAVA, Figure 1) related to the subduction of the same Cocos oceanic plate beneath the Caribbean plate. This database enabled us to compare and contrast the geochemistry of the SCN with a classic arc (CAVA), particularly using the new log-ratio discriminant function based multi-dimensional diagrams (Verma *et al.* 2006; Verma & Agrawal 2011). The sources for these data were as follows: Carr (1984); Hazlett (1987); Reagan & Gill (1989); Carr *et al.* (1990); Walker *et al.* (1990, 2001); Bardintzeff & Deniel (1992); Cameron *et al.* (2002); Agostini *et al.* (2006); Alvarado *et al.* (2006); Bolge *et al.* (2006) and Ryder *et al.* (2006). Data from the rest of the MVB were not considered here, because they had been studied elsewhere (e.g., Verma 2009; Verma *et al.* 2011).

Rock classification was based on the total alkali-silica (TAS) scheme (Figure 3; Le Bas *et al.* 1986) on an anhydrous 100% adjusted basis and Fe_2O_3/FeO ratios assigned according to the rock type (Middlemost 1989). All computations (anhydrous and iron-oxidation ratio adjustments, and rock classifications) were automatically done using the SINCLAS computer program (Verma *et al.* 2002).

To compute and report central tendency and dispersion parameters, mean and standard deviation estimates were used after ascertaining that the individual parameter values were drawn from normal populations free of statistical contamination. To check this, a computer program was used to apply all single-outlier type discordancy tests at a strict 99% confidence level (DODESSYS by Verma & Díaz-González 2012).

5. Geochemical and mineralogical composition

This section presents the geochemical, isotopic (Appendix A1–3), and mineralogical (Appendix A4–10) characteristics of different types of SCN magmas (Figures 3–6). The interpretation of these data will be presented in the next section.

5.1. Mafic magmas

Approximately 15% of magmas that constitute the SCN database have $(SiO_2)_{adj}$ < 53% and Mg# [100*Mg/(Mg + Fe^{+2})] = 64–72 (mafic magmas, *M*). Note that we are not using mafic magmas as synonymous of basic magmas, because the latter have been defined as $(SiO_2)_{adj}$ < 52% (Le Bas *et al.* 1986). The upper limit of 53% was used mainly because we wanted to have a number of samples for inverse modelling that might provide statistically significant results.

The mafic magmas are usually porphyritic or microcrystalline with < 25% of phenocryst content. Phenocrysts are of euhedral olivine with inclusions of chromiferous spinel, and plagioclase. However, in many samples, plagioclase occurs only as microphenocrysts. The groundmass consists of these minerals, plagioclase being the main component; opaque minerals (titanomagnetite, ilmenite) are also present. In many samples both phenocrysts and groundmass plagioclase show a preferred flow orientation. Additionally, some rocks show circular or elongated vesicles (6–10% in volume).

Representative core analysis and structural formulae for olivine, spinel and plagioclase in SCN mafic magmas are reported in Velasco-Tapia & Verma (2001b). Olivine phenocrysts show an average core composition of $Fo_{85.9\pm2.5}$ (n= 48). Rims of most olivine phenocrysts show small variations in composition (0.2 to 4.0 in %Fo) compared to the core data, although some phenocrysts showed greater differences (17%). Olivine compositional data are consistent

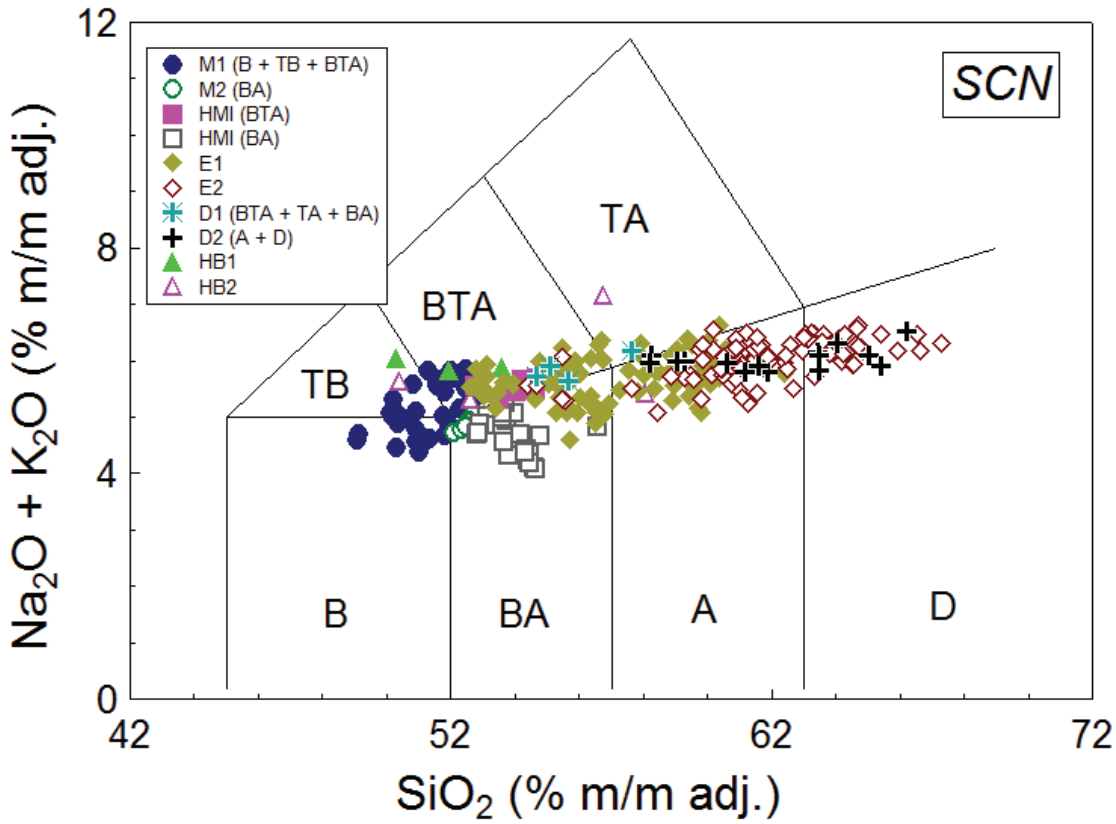

Figure 3. Total alkali–silica diagram (TAS; Le Bas *et al.* 1986) for SCN magmas, based on recalculated major-element whole-rock concentrations normalized to 100% volatile-free with Fe_2O_3/FeO after Middlemost (1989) from SINCLAS computer program (Verma *et al.* 2002). Field names: B– basalt; BA– basaltic andesite; A– andesite; D– dacite; TB– trachybasalt; BTA– basaltic trachyandesite; TA– trachyandesite. Rock-type labels are the same as Figure 2.

with those previously reported by Wallace & Carmichael (1999) and Márquez & De Ignacio (2002). Chromiferous spinel inclusions are characterised by typical compositions of inverse structure Fe/(Fe+Mg)= 0.54±0.06, Cr/(Cr+Al)= 0.49±0.05, and Fe^{+3}/Fe= 0.35±0.05 (n= 25). However, it is not possible to assign specific names, as all specimens are situated in the central part of the $MgAl_2O_4$–$MgCr_2O_4$–$FeCr_2O_4$–$FeAl_2O_4$ prism (Haggerty 1991). Plagioclase is present as small euhedral phenocrysts, without optical zoning, of labradorite composition ($An_{59.8\pm4.7}$; n= 29).

Using the TAS diagram (Figure 3; Le Bas *et al.* 1986), *M* magmas are classified as B, TB, BTA, and BA. All rocks show LREE (light rare-earth elements) enriched chondrite-normalised patterns (Figure 4a), being reflected by $[La/Yb]_N$ (chondrite-normalised) ratios of 5.1±0.9 (n= 18, range= 3.6–6.8), without a negative Eu anomaly. MORB-normalised multi-element plots of these magmas show enrichment in large ion lithophile elements (LILE) and lack high field strength element (HFSE) significant negative anomalies (Figure 5a). *M*-type magmas display $^{87}Sr/^{86}Sr$ ratios from 0.70348 to 0.704302 (n= 12), whereas $^{143}Nd/^{144}Nd$ ratios covers a narrow interval from 0.51279 to 0.51294 (n= 11). All samples fall within the 'mantle array' (Faure 1986) in the $^{87}Sr/^{86}Sr$–$^{143}Nd/^{144}Nd$ diagram (Figure 6a).

5.2. Evolved magmas

Evolved SCN rocks, $(SiO_2)_{adj}$ > 53%, are usually porphyritic or microcrystalline with <26% of phenocrysts, of which some have circular or elongated vesicles reaching 6–10% of total volume. However, some lava domes (for example, Tabaquillo or Lama) have phenocryst content as high as 50%. Groundmass mainly consists of plagioclase, pyroxenes, and magnetite. Based on their mineralogical assemblage of phenocrysts, SCN evolved magmas are divided into two groups: (a) *E1*: ol + opx ± cpx ± plg; and (b) *E2:* opx ± cpx + plg.

Euhedral olivine crystals in *E1* magmas have a similar composition ($Fo_{84.1\pm3.1}$; n= 24; Appendix A4) as observed in specimens included in *M*-type magmas, although their rims are more enriched in iron ($Fo_{77.3\pm5.2}$; n= 17). Spinel inclusions are abundant in olivine, being slightly more chromiferous (Cr/[Cr + Al]= 0.57±0.07, n= 17; Appendix

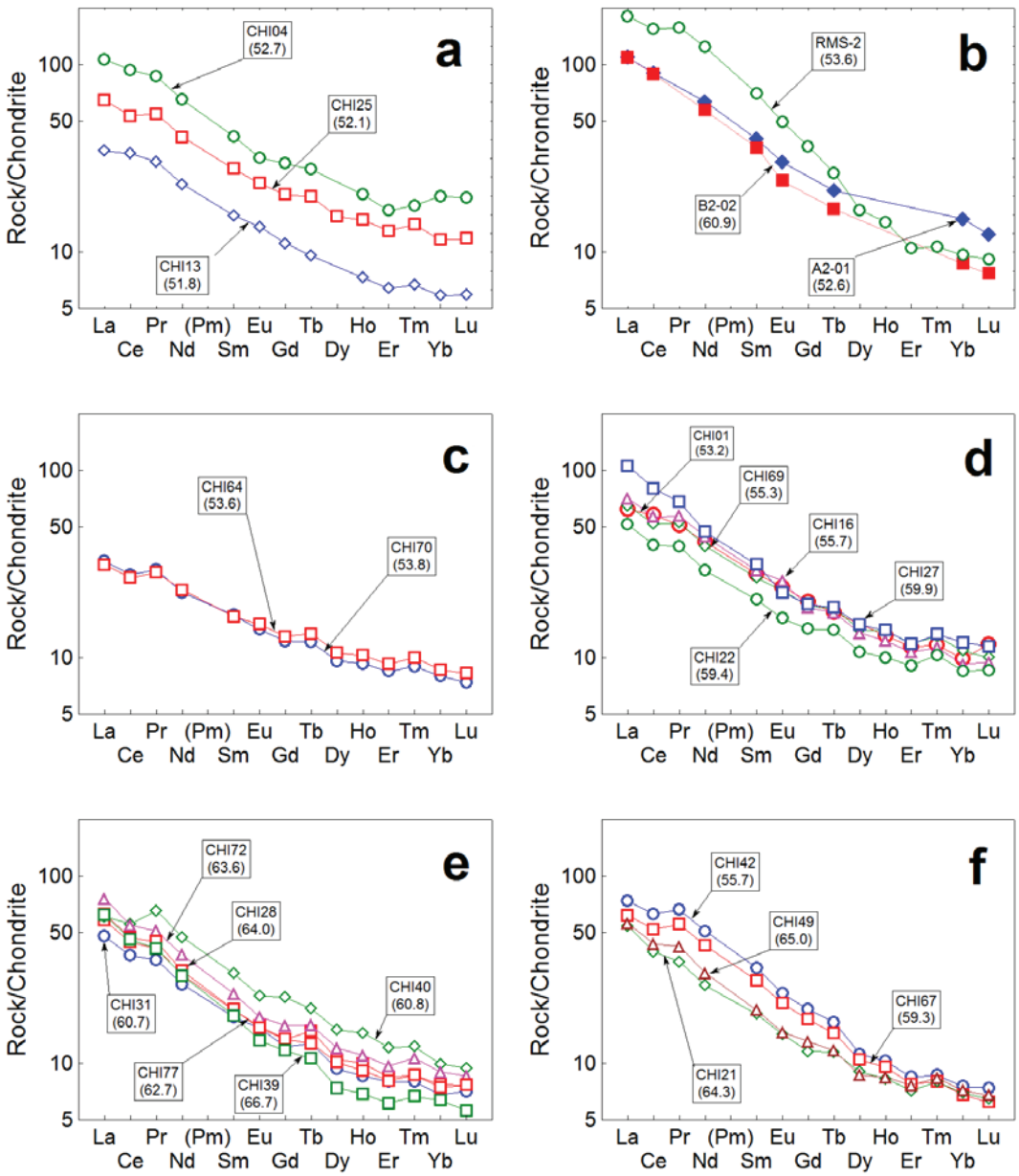

Figure 4. Chondrite-normalised REE diagrams for SCN magmas: (**a**) mafic magmas; (**b**) high-Ba magmas; (**c**) high-magnesium intermediate magmas; (**d**) evolved magmas with an ol + opx ± cpx ± plg mineralogical assemblage; (**e**) evolved magmas with an opx ± cpx + plg mineralogical assemblage; and (**f**) disequilibrium magmas. The adjusted $\%SiO_2 - (SiO_2)_{adj}$ is reported for each sample. Chondrite data ($mg.g^{-1}$) from Haskin *et al.* (1968) and Nakamura (1974): La= 0.329, Ce= 0.865, Pr= 0.112, Nd= 0.63, Sm= 0.203, Eu= 0.077, Gd= 0.276, Tb= 0.047, Dy= 0.343, Ho= 0.07, Er= 0.225, Tm= 0.03, Yb= 0.22, and Lu= 0.0339.

A5) than those in the *M*-magmas. Orthopyroxenes (enstatite) are typically subhedral to euhedral, usually displaying normal zoning with a homogeneous composition (cores: $En_{81.1\pm1.5}$, n= 14; rims: $En_{80.6\pm1.4}$, n= 12; Appendix A6). Clinopyroxenes (augite: En_{47}; Appendix A7) appear only in the groundmass. Plagioclases are labradorite, comparable to plagioclases in *M*-type magmas ($An_{59.6\pm4.5}$, n= 14; Appendix A8). *E1* magmas are distributed in the BTA, BA, TA, and A fields on the TAS diagram (Figure 3), with $(SiO_2)_{adj}$= 53.0–62.4 and Mg#= 52–74 (n= 90). These rocks show LREE-enriched patterns and lack or display a very small negative Eu anomaly (Figure 4d). $[La/Yb]_N$ ratios displayed by these magmas (7.0±1.6, n= 19) are significantly higher compared to the *M* magmas.

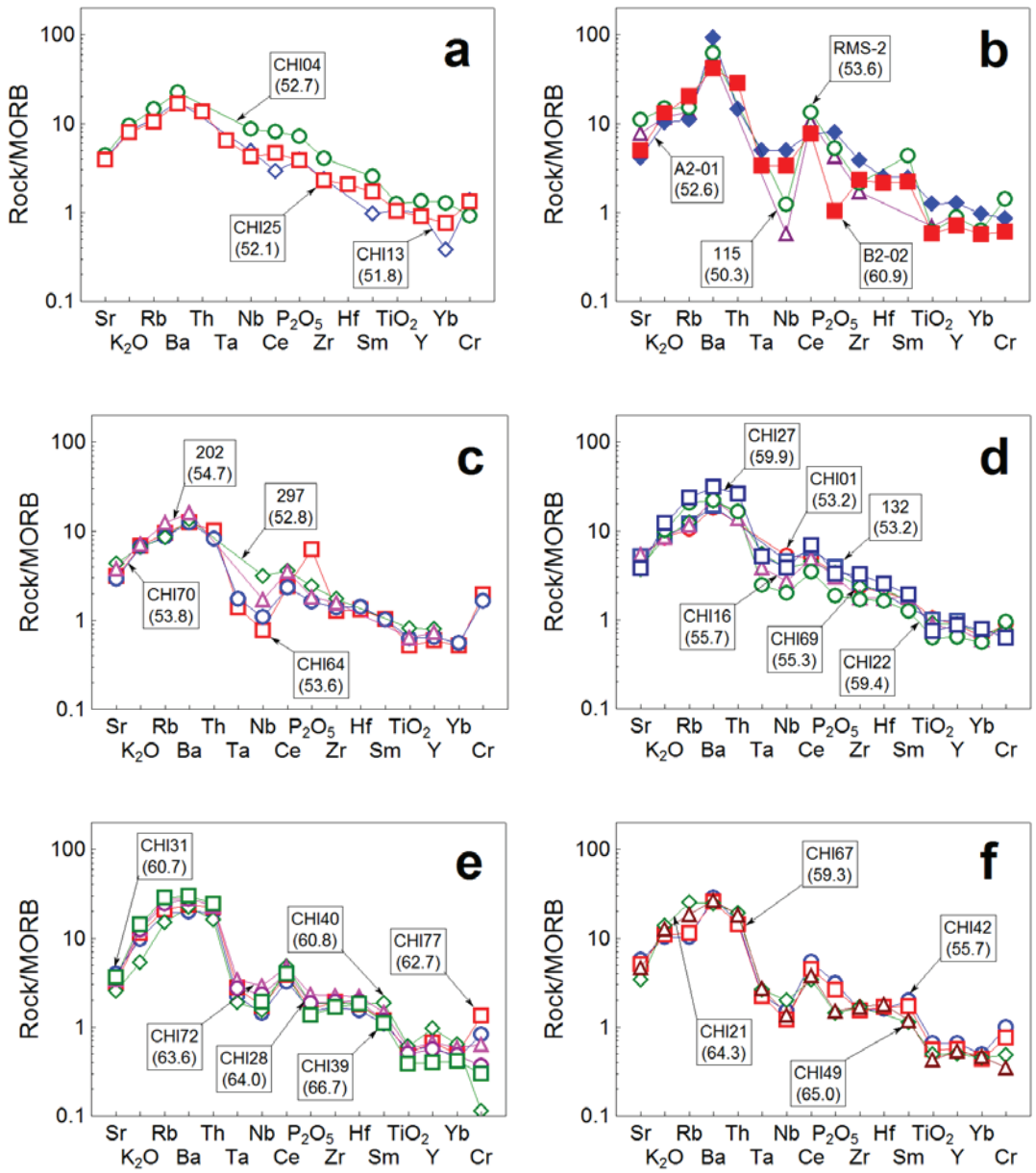

Figure 5. N-MORB-normalised multi-element diagrams for SCN magmas: (**a**) mafic magmas; (**b**) high-Ba magmas; (**c**) high-magnesium intermediate magmas; (**d**) evolved magmas with an ol + opx ± cpx ± plg mineralogical assemblage; (**e**) evolved magmas with an opx ± cpx + plg mineralogical assemblage; and (**f**) disequilibrium magmas. The adjusted $\%SiO_2 - (SiO_2)_{adj}$ is reported for each sample. N-MORB data (%m/m for major-oxides and $mg.g^{-1}$ for trace elements) from Pearce (1982): Sr= 120, K_2O= 0.15%, Rb= 2, Ba= 20, Th= 0.20, Ta= 0.18, Nb= 3.5, Ce= 10, P_2O_5= 0.12%, Zr= 90, Hf= 2.40, Sm= 3.3, TiO_2= 1.5, Y= 30, Yb= 3.4, and Cr= 250.

Multi-element MORB-normalised diagrams are similar to those showed by *M* magmas with the exception of a slightly negative Nb anomaly (Figure 5d). The statistical comparison of *E1* with *M* magmas reveals that (a) significantly higher contents of four LILE (K, Cs, Rb, and Ba), one HFSE (Hf) and two actinide-HFSE (Th and U); (b) similar concentrations for REE (La-Lu), one LILE (Sr), and two HFSE (Zr and Ta); and (c) significantly lower Nb and Y contents.

Felsic *E2* magmas are mainly pyroxene-phyric andesites and dacites ($(SiO_2)_{adj}$= 55.4–67.3, Mg#= 49.5–71.5; n= 96), sometimes showing clots of ortho > clinopyroxene.

Augitic and enstatitic pyroxenes are normally zoned, both displaying a narrow compositional range for cores (opx: $En_{82.7\pm3.1}$, n= 45, Appendix A6; cpx: $En_{46.3\pm2.1}Wo_{43.3\pm1.3}$, n= 28, Appendix A7), with changes of 6–10% in %En for rims. However, some specimens also contain pyroxene phenocrysts showing slightly reverse zoning (opx in CHI02, Appendix A6; cpx in CHI71, Appendix A7). Plagioclase phenocrysts display a narrow compositional range ($An_{59.5\pm3.9}$, n= 12). Felsic *E2* magmas have REE ($[La/Yb]_N$= 8.1±1.4, n= 49; Figure 4e) and MORB-normalised multi-element (Figure 5e) patterns similar to those of *E1* magmas. Compared to *M* magmas, *E2* magmas have: (a) significantly higher concentrations for three LILE (Ba, Rb, and Cs) and actinide-HFSE (Th and U); (b) similar compositions for LREE (La-Nd, except Ce), Dy, Hf and Sr; and (c) significantly lower contents for Ce, MREE (Sm-Tb), HREE (Ho-Lu), and four HFSE (Nb, Ta, Y, and Zr). It is remarkable that *E2* magmas with somewhat higher silica levels — $(SiO_2)_{adj}$= 61.8±2.5 (n= 96) show significantly higher contents only for Ba, Cs, Rb, and actinide-HFSE (Th and U) compared to *E1* magmas — $(SiO_2)_{adj}$= 57.0±2.5 (n= 90).

Sr isotope ratios of the evolved magmas display significant variations over their SiO_2 range (*E1*: 0.7036–0.7048; *E2*: 0.7037–0.7047). Nd isotope ratios range from 0.5127 to 0.5130 and show a well-defined negative correlation with Sr isotope ratios (Figure 6b). Generally, $^{87}Sr/^{86}Sr$ and $^{143}Nd/^{144}Nd$ fall within the 'mantle array' field, overlapping with the high $^{143}Nd/^{144}Nd$ side of the Mexican lower crust (Patchett & Ruiz 1987; Ruiz *et al.* 1988a, b; Roberts & Ruiz 1989; Schaaf *et al.* 1994).

5.3. High-Mg intermediate magmas

Intermediate magmas with relatively high contents of MgO (*HMI*) have been emitted from some volcanic centres of the SCN, most of them situated in the W area (Figure 2). As *M* magmas, these rocks are also usually porphyritic, with <20% vol. % phenocrysts in a glassy matrix. Phenocrysts are predominantly euhedral olivine, plagioclase, and occasionally orthopyroxene. The groundmass is largely made of small plagioclase microcrystals.

Euhedral olivine cores have compositions of $Fo_{88.5\pm1.4}$ (n= 17), being slightly more mafic than those in *M*-type magmas (Appendix A4). In general, there is little change in the forsterite proportion throughout the olivine crystals (0.1–4.0%). The phenocrysts contain numerous chromiferous spinel inclusions of inverse structure (Appendix A5), with a composition of Fe/(Fe + Mg)= 0.52±0.08, Cr/(Cr + Al)= 0.563±0.020, and Fe^{+3}/Fe= 0.322±0.031 (n= 15). Moderately zoned labradoritic plagioclase phenocrysts also occur, although with more calcic cores (n= 9; $An_{64.2\pm1.4}$; Appendix A8) compared to those in *M* magmas.

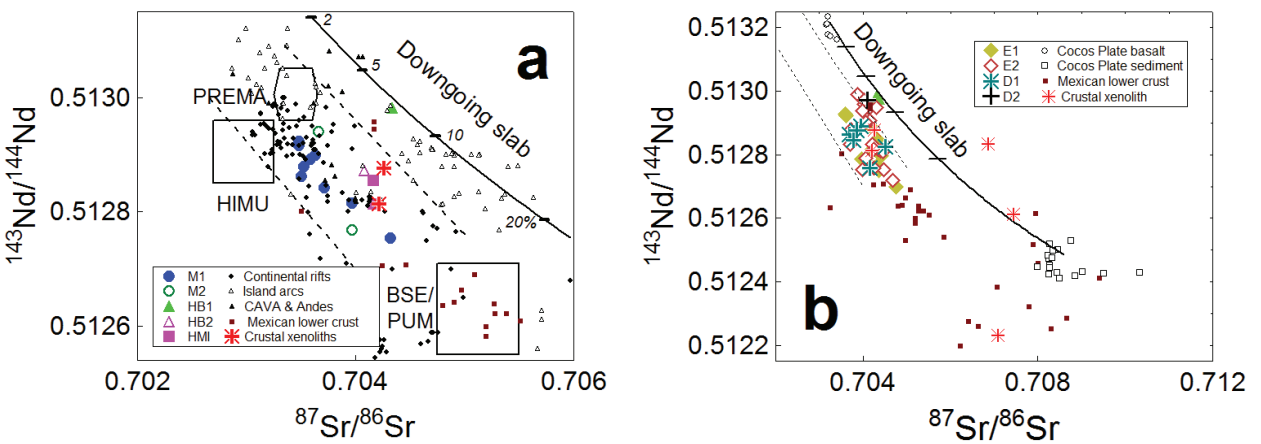

Figure 6. $^{87}Sr/^{86}Sr$-$^{143}Nd/^{144}Nd$ plot for the SCN magmas and their comparison with other tectonic areas, mantle and crustal reservoirs, and the descending slab. The symbols used are shown as inset in each Figure. The "Mantle-array" (dashed lines) is included for reference (Faure 1986). (**a**) The mafic, high-Ba, and high-Mg intermediate SCN rocks are compared with primitive rocks (Mg# > 63, $\%SiO_2$ adj < 52) from continental rifts including extension-related areas as well as from island and continental arcs including the northern CAVA. All mantle components named after Zindler & Hart (1986) are: BSE– bulk silicate earth or PUM– primitive uniform mantle reservoir; PREMA– prevalent mantle composition; HIMU– high U/Pb mantle component. Also included is the mixing line (thick solid curve) of two-component mixing of altered basalts and sediments from the 'Downgoing slab' or Cocos plate (Verma 2002) The numbers (2–20%) indicate the %m/m of the sediment component in the mixture. Note the shift towards the 'Downgoing slab' shown by numerous arc magmas. (**b**) The high-Ba, evolved, and disequilibrium SCN rocks are compared with the Mexican lower crust (Patchett & Ruiz 1987; Ruiz *et al.* 1988a, b; Roberts & Ruiz 1989; Schaaf *et al.* 1994), crustal xenoliths from Popocatépetl near the SCN (Schaaf *et al.* 2005), and altered basalt and sediments from the subducting Cocos plate ('Downgoing slab'; Verma 2000). The basalt-sediment mixing curve is the same as in (**a**).

According to the nomenclature of Le Bas *et al.* (1986), the *HMI* magmas are classified as BTA and BA (*HMI1* and *HMI2* respectively in Figure 3), having $(SiO_2)_{adj}$= 52.7–56.6%, $(MgO)_{adj}$= 6.5–10.2% and Mg#= 66–76 (n= 32). All rocks show enrichment in light REE, a gradual slope change which leads to a nearly flat pattern in heavy REE (Figure 4c; $[La/Yb]_N$= 5.1±1.0, n= 7, range= 3.6–6.4), and a negligible Eu anomaly. MORB-normalised multi-element plots (Figure 5c) display a pattern characterised by enrichments in LILE (Sr, K, Rb, and Ba) and depletion of HFSE (Nb, Ta, and Ti), which contrasts with the observed patterns for *M* magmas. Moreover, two LREE (La and Ce), three MREE (Sm, Eu, and Tb), Sr, and five HFSE (Hf, Nb, Ta, Y, and Zr) concentrations in *HMI* rocks are statistically lower than the *M* magmas, whereas the differences in composition of the rest of the incompatible elements are not statistically significant. However, *HMI* magmas have $^{87}Sr/^{86}Sr$ (0.70390–0.70416) and $^{143}Nd/^{144}Nd$ (0.51281–0.51285) ratios (n= 3) nearly comparable with those displayed by *M* magmas.

5.4. Two types of high-Ba magmas

In the SCN mafic emissions are characterised by a high concentration of Ba compared to *M* magmas and the other rock-types. This group, designated here as *HB1,* comprises one TB and three BTA ($(SiO_2)_{adj}$= 52.1±1.4; MgO= 9.0±0.9, Mg#= 74.5±0.5), erupted in the NW part of the monogenetic field, and not near the volcanic front.

In statistical comparison with *M* magmas at the same SiO_2 level (BTA and BA), the *HB1* group shows the following characteristics: (a) significantly higher concentrations of LREE (La-Nd), MREE (Sm-Gd), LILE (K, Rb, Ba, and Sr) and actinide-type HFSE (Th and U); (b) similar contents of MREE (Tb and Dy), HREE (Ho-Lu) and three HFSE (Zr, Hf, and Y); and (c) significantly lower composition of two HFSE (Ti and Nb). Chondrite-normalised REE patterns for *HB1* are LREE enriched (Figure 4b; $[La/Yb]_N$ ~18.4), whereas a significant Nb depletion with respect to Ba and Ce is observed on a MORB-normalised multi-element diagram (Figure 5b). The BTA RMS-2 (Martínez-Serrano *et al.* 2004) shows higher $^{87}Sr/^{86}Sr$ and similar $^{143}Nd/^{144}Nd$ isotopic ratios compared to *M* mafic rocks, with a shift towards the right of the mantle array (Figure 6a).

A second group of high-Ba magmas (*HB2*) occurs in the central part of SCN (Figure 2). This group includes a variety of magma types (TB, BTA, TA, and A; $(SiO_2)_{adj}$= 50.4–61.7, Mg#= 61.2–71.0, Figure 3), which show high concentrations of Ba (715-1830 $mg.g^{-1}$) and light REE (La= 23–58 $mg.g^{-1}$; $[La/Yb]_N$= 7.3–12.0; Figure 4b), accompanied by relatively high contents of HFSE (Nb= 8–19 $mg.g^{-1}$; Zr= 249–344 $mg.g^{-1}$; Figure 5b). However, compared to *E2* magmas at the same SiO_2 level, *HB2* rocks have significantly lower La, Ce, and Ba contents.

5.5. Disequilibrium magmas (DISQ)

The *DISQ* group comprises rocks that range widely in $(SiO_2)_{adj}$ (54.7–66.2; BTA to D; n= 20) and Mg# (51–73), but with the two following distinctive features: (a) abundant textural evidence of mineralogical disequilibrium, such as coexisting Fo-rich olivine and quartz with pyroxene reaction rims and disequilibrium textures in plagioclase with oscillatory or more complex zoning and twinning; and (b) the occurrence of hydrous minerals (biotite, amphibole), absent in the other rock groups. Similar mineralogical characteristics have been reported in the evolved magmas erupted by the neighbouring stratovolcanoes Iztaccíhuatl (Nixon 1988a, b) and Popocatépetl (Straub & Martin del Pozzo 2001), which were interpreted as the result of mixing between mafic (derived from mantle) and felsic (derived from crust) magmas. Consequently, such a scenario can also be hypothesised for the SCN. See the Discussion section below.

Unzoned or slightly normally zoned olivine phenocrysts of the *DISQ* group have cores of $Fo_{83.9±3.4}$ (n= 17; Appendix A4). Orthopyroxene (enstatite) cores have compositions ($En_{82.4±3.6}$, n= 18; Appendix A6) comparable to those observed in other rock groups. Clinopyroxenes exhibit a varied morphology that includes euhedral, subeuhedral or skeletal crystals, showing an augitic composition ($En_{45.0±1.8}Wo_{44.5±1.6}$; n= 18; Appendix A7). In some samples, pyroxenes with normal and reversed zoning (e.g., opx: CHI08, CHI49, and CHI63, Appendix A6; cpx: CHI21, Appendix A7) are present. Several rounded quartz grains show hypersthene reaction rims (CHI11, $En_{70}Fs_{27}$). Compared to other rock groups, plagioclase cores in *DISQ* magmas vary more in composition ($An_{54±13}$, n= 15). In some cases, as dacite CHI09, the plagioclases of groundmass display a bimodal composition (An_{20} and An_{60}). Some dacitic thick lava flows, such as Lama CHI10 and Tabaquillo CHI79, include abundant large plagioclase phenocrysts (2–4 mm in length) characterised by concentric oscillatory zoning with the cores more calcic than the rims (Appendix A9). Additionally, these magmas contain hydrated minerals, amphibole (edenite, tschermakite, and hastingsite; Márquez & De Ignacio 2002) and brown biotite (annite; Appendix A10), strongly altered to iron oxides.

DISQ magmas show LREE-enriched patterns with either a very small or no negative Eu anomaly (Figure 4f). $[La/Yb]_N$ ratios displayed by these magmas are somewhat higher than mafic magmas (7.1±1.7, n= 9). MORB-normalised multi-element plots are characterised by relatively enriched LILE and depleted HFSE (Figure 5f), comparable with the *E1* and *E2* patterns and contrasting with those observed in *M* magmas. Note that, in this group, REE, LILE and HFSE concentrations diminish with increasing $(SiO_2)_{adj}$ (Figures 4f & 5f). Statistically, trace

element compositions in *DISQ* magmas are comparable with those shown by felsic *E2* magmas, except for La, Rb and Ta (more concentrated in *E2*) and Sr (with high content in *DISQ*). The Sr (0.7037–0.7045; n= 7) and Nd (0.5128–0.5130; n= 7) isotopic ratios of *DISQ* magmas are within the range defined by evolved magmas from SCN and the Mexican lower crust and crustal xenoliths from the Popocatépetl stratovolcano located near the SCN (Figure 6b).

6. Discussion

6.1. Origin of the mafic magmas

(1) SCN near-primary magmas – Following Luhr (1997), 35 samples of *M* magma were identified with geochemical characteristics of near-primary magmas (*M1:* $(SiO_2)_{adj}$= 49.0–52.7%, $(MgO)_{adj}$= 7.0–9.3%, Mg#= 64.1–72.7): basalt (12 samples); trachybasalt (8); and basaltic trachyandesite (15). Average compositions of these magma types are reported in Appendix A11.

(2) Trace element ratios (subduction vs mantle signature) – In addition to relatively high Mg#, *M1* magmas do not show significant HFSE (Nb and Ta) depletion compared to LILE (Rb, Ba and Sr) (Figure 5a). These magmas also have low Ba/Nb (< 30), Sr/P (< 0.45), Rb/La (<1.3), and Cs/Th (< 0.5) ratios (Figure 7a, b), similar to those observed in most rocks from continental rifts and break-up areas (e.g., Verma 2006). This behaviour contrasts with that exhibited by island and continental arcs (Hawkesworth *et al.* 1991; Tatsumi & Eggins 1993; Verma 2002).

SCN near-primary magmas show significantly small negative Nb anomalies (expressed as $[Nb/Nb^*]_{Primitive\text{-}mantle}$ defined by Verma (2006); Appendix A12; mean or median

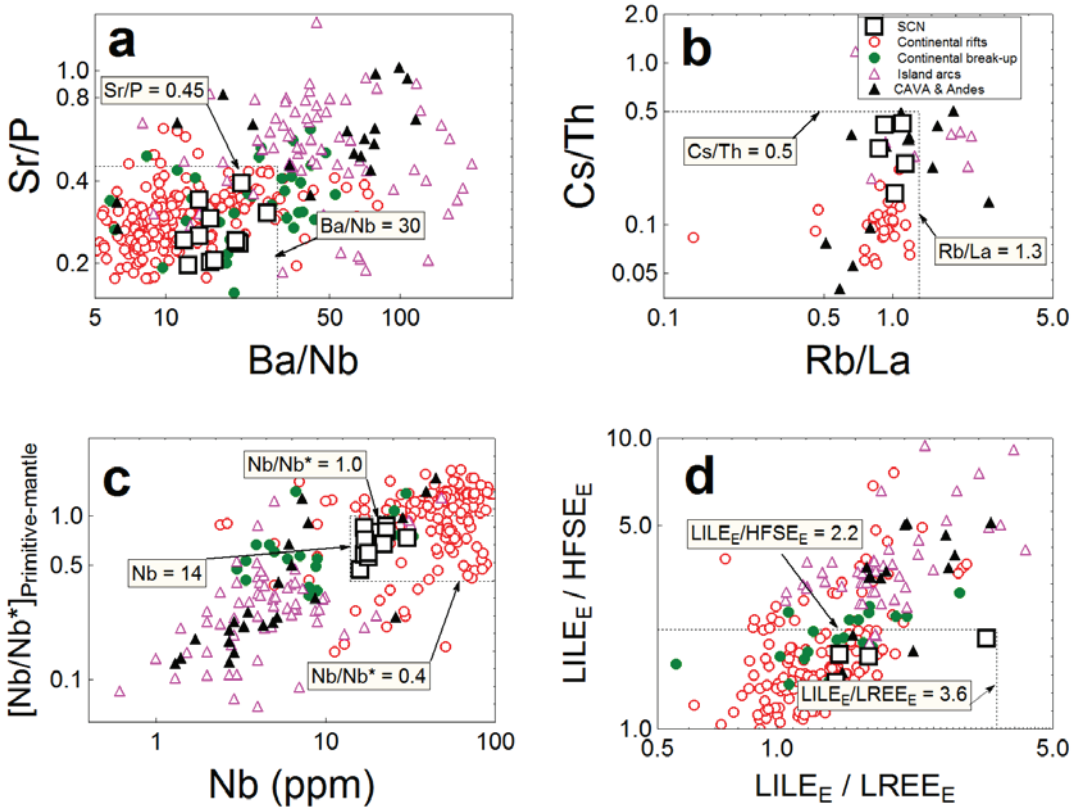

Figure 7. Four binary diagrams constructed using slab-sensitive or mantle-sensitive parameters (Verma 2006) for near primary mafic magmas from the SCN (open squares) and their comparison with similar rocks from continental rifts, including extension-related areas and continental break-up regions, as well as from island and continental arcs including the CAVA and Andes. Dotted lines in different diagrams give approximate reference values for the fields occupied by the SCN mafic rocks. (**a**) Slab-sensitive Ba/Nb–slab sensitive Sr/P (therefore, both parameters are likely to have high values for arcs); (**b**) slab-sensitive Rb/La–slab sensitive Cs/Th; (**c**) mantle sensitive Nb-$[Nb/Nb^*]_{Primitive\ mantle}$, where $[Nb/Nb^*]_{Primitive\ mantle}$ is a quantitative measure of Nb anomaly defined as the ratio of actually measured Nb concentration of a sample normalized with respect to primitive mantle and the average value of primitive mantle-normalized concentrations of Ba and La in the same sample (primitive mantle values were from Sun & McDonough 1989); and (**d**) slab-sensitive $[LILE_E/LREE_E]$–slab sensitive $[LILE_E/HFSE_E]$ where subscript E refers to bulk silicate earth-normalised values, $LILE_E = (K_E + Rb_E + Ba_E + Sr_E)/4$, $LREE_E = (La_E + Ce_E + Nd_E)/3$, and $HFSE_E = (Nb_E + Zr_E + Ti_E + P_E)/4$. All concentrations data in $mg.g^{-1}$ were normalized against bulk silicate earth values (E) given by McDonough & Sun (1995).

value ~0.69; 95% and 99% confidence limits of 0.61–0.77 and 0.58–0.81, respectively), which are similar to those in extension-related areas (Figure 7c). For comparison, island and continental arc magmas have $[Nb/Nb^*]_{Primitive-mantle}$ mean or median values of ~0.06–0.32 (Appendix A12; 95% and 99% confidence limits within the range ~0.03–0.47 and ~0.01-0.60, respectively). A negative Nb anomaly is also a common characteristic of primitive rocks from rifts, extension-related regions, and continental break-up areas (Figure 7c and Appendix A12) although its value is different from that in arcs. Furthermore, in arcs the negative Nb anomaly is accompanied by low Nb contents (generally < 10 $mg.g^{-1}$; Verma 2006). Additionally, the *M1* magmas have $LILE_E/HFSE_E < 2.2$, comparable to extension and continental break-up magmas (Figure 7d; Verma 2004, 2006). Three samples of mafic magmas from the SCN (not included in our database) reported by Schaaf *et al.* (2005), also have geochemical characteristics similar to the *M1* magmas.

(3) Discrimination diagrams – Major and trace element signatures have been widely used in conventional discrimination diagrams to identify different tectonic settings (e.g., Pearce & Cann 1973; Shervais 1982; Meschede 1986; Cabanis & Lecolle 1989). However, the application of these older geochemical diagrams has been criticised (Verma 2010) on the basis of the following reasons: (a) the discrimination only uses bi- or tri-variate data drawn from 'closed' arrays; (b) the diagrams were generally constructed using a limited geochemical database; (c) they do not incorporate proper statistical treatment for compositional data (Aitchison 1986); (d) most such diagrams discriminate only broadly grouped settings, such as within-plate that combines continental rift basalt (CRB) and OIB settings; and (e) the boundaries in most tectonic discrimination diagrams are drawn by eye (Agrawal 1999).

All objections were in fact overcome in three sets of discriminant function based multi-dimensional diagrams (Verma *et al.* 2006; Agrawal *et al.* 2008; Verma & Agrawal 2011), in which natural-logarithm transformed ratios were used for LDA. These newer diagrams have been successfully used for the study of different areas (e.g., Srivastava *et al.* 2004; Rajesh 2007; Sheth 2008; Polat *et al.* 2009; Slovenec *et al.* 2010; Zhang *et al.* 2010). The results of their application to the SCN are summarised in Figure 8a–e for Verma *et al.* (2006) diagrams for major-elements and Figure 9a–e for Verma & Agrawal (2011) diagrams for the so called immobile elements – $(TiO_2)_{adj}$, Nb, V, Y, and Zr. For the other set of immobile elements (La, Sm, Yb, Nb, and Th), the set of diagrams proposed by Agrawal *et al.* (2008) could not be used, because complete data were available for only one mafic rock sample from the SCN. The results from Figure 8a–e show high success rates of 93% to 100% for the SCN as a continental rift setting and 76–80% for CAVA as an arc setting (Appendix A13). For Verma & Agrawal (2011) diagrams (Figure 9a–e) only four basic rock samples from the study area were available with complete data, although they indicated a continental rift setting. For CAVA an arc setting is fully confirmed (Appendix A13).

In a study of the SCN, Siebe *et al.* (2004; their figure 13) plotted data for mafic rocks in two conventional bivariate discrimination diagrams and, although clearly a within plate setting was indicated, these authors refrained from commenting on their results. How could these results for mafic magmas be explained by their preferred subduction-related model?

(4) Isotopic constraints – On a $^{87}Sr/^{86}Sr$ – $^{143}Nd/^{144}Nd$ diagram (Figure 6a), *M1* magmas plot in the same field as the primitive rocks from continental rifts and extension-related areas as well as island and continental arcs. Altered basalts and sediments from the subducting Cocos plate ('Downgoing slab'; Verma 1999) are included in the graph to show that slab composition (basalt-sediment mixing curve) plots considerably to the right of SCN near-primary magmas. These results contradict the conventional subduction-related models such as those proposed by Wallace & Carmichael (1999). In contrast, CAVA magmas (Carr *et al.* 1990) fall in an area to the right of the 'mantle array', closer to the basalt-sediment mixing curve for the Cocos plate. This shift towards the right of the 'mantle array' has been reported in many others arcs, as discussed by Verma (2006), such as Izu-Bonin arc (Taylor & Nesbitt 1998), Kamchatka arc (Kepezhinskas 1995), Lesser Antilles arc (Thirwall *et al.* 1997), South Sandwich island arc (Hawkesworth *et al.* 1977), Sunda arc (Hoogewerff *et al.* 1997), and Tonga-Kermadec arc (Gamble *et al.* 1995). This isotopic shift has also been detected in metabasaltic rocks from the Franciscan subduction complex (Nelson 1995) and altered oceanic basalts (Verma 1992).

The involvement of the 'Downgoing slab' in the genesis of the SCN *M1* magmas is also not favoured by the amount of sediment necessary to reproduce their isotopic ratios. In fact, SCN near-primary magmas require ~5–20% of sediments to mix with altered slab basalts in order to cover the observed range of $^{143}Nd/^{144}Nd$, but $^{87}Sr/^{86}Sr$ data cannot be explained by such a mixing process (Figure 6a). Further, mixing calculations have indicated that the isotope geochemistry of most arc magmas can be explained by incorporating ≤–3% of sediment component (White & Dupré 1986). Additionally, Righter *et al.* (2002) pointed out that it is problematic to explain a fluid transport process from the slab beneath the MVB considering the low Re and Cl contents and low $^{187}Os/^{188}Os$ ratios observed in MVB primary magmas. Finally, it is not possible to reproduce the isotopic ratios observed in SCN near-

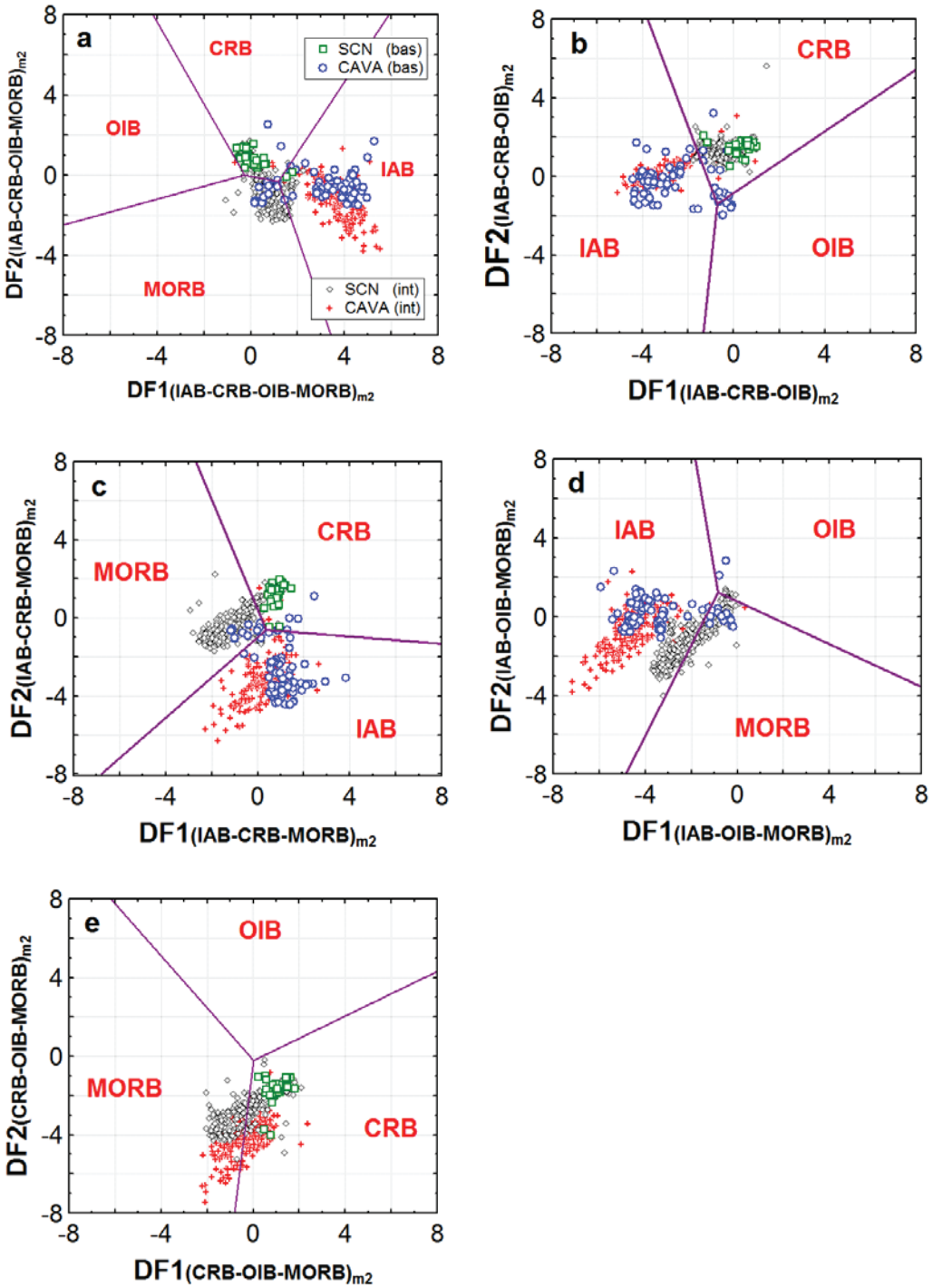

Figure 8. Five discriminant function diagrams, based on linear discriminant analysis (LDA) of $\log_e$-transformation of major-element ratios (Verma *et al.* 2006), for SCN and CAVA basic (*bas*) magmas with $(SiO_2)_{adj} < 52\%$. The percent given next to the tectonic setting name represents the percent success obtained by these authors during the testing stage of these diagrams. (**a**) Island arc (IAB)–Continental rift (CRB)–Ocean island (OIB)–Mid-Ocean ridge (MORB) diagram; (**b**) Island arc (IAB)–Continental rift (CRB)–Ocean island (OIB) diagram; (**c**) Island arc (IAB)–Continental rift (CRB)– Mid-Ocean ridge (MORB) diagram; (**d**) Island arc (IAB)–Ocean island (OIB)–Mid-Ocean ridge (MORB) diagram; (**e**) Continental rift (CRB)–Ocean island (OIB)–Mid-Ocean ridge (MORB) diagram. Note that all diagrams indicate a "continental rift" tectonic setting for the SCN magmas. All diagrams also include SCN and CAVA intermediate (int) magmas $(52 < (SiO_2)_{adj} < 63)$, showing their differences in DF1 and DF2 parameters. Note that the inclusion of intermediate rocks is simply for highlighting the differences between these two provinces and not for identifying their probable tectonic setting.

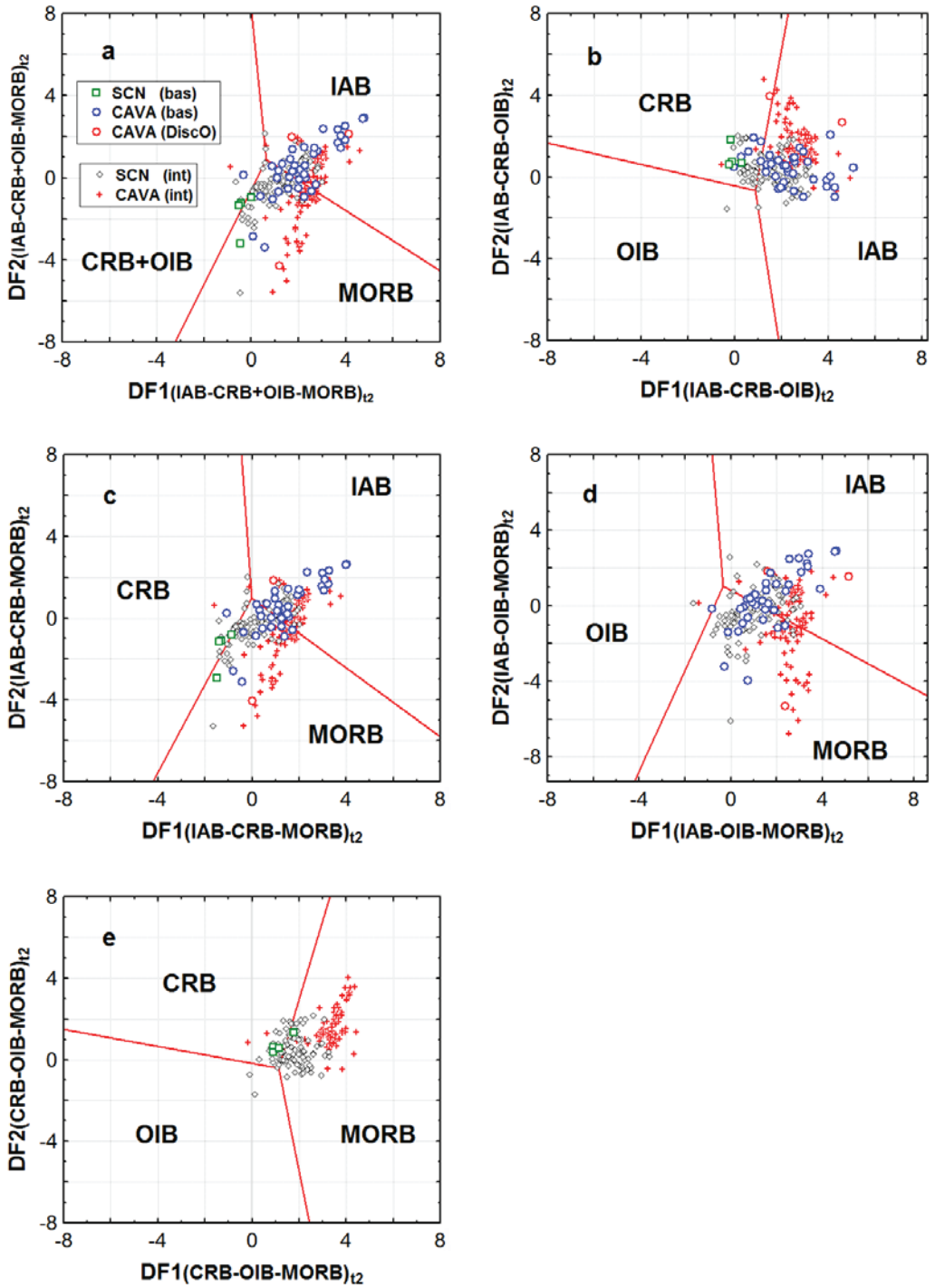

Figure 9. Five discriminant function diagrams, based on linear discriminant analysis (LDA) of $\log_e$-transformation of element ratios (Verma & Agrawal 2011), for SCN and CAVA basic (*bas*) magmas with $(SiO_2)_{adj}$ < 52%; where DiscO are CAVA data detected as discordant values by single-outlier detection tests DODESSYS; Verma & Díaz-González 2012). (**a**) Island arc (IAB)–Continental rift (CRB)+Ocean island (OIB)–Mid-Ocean ridge (MORB) diagram; (**b**) Island arc (IAB)–Continental rift (CRB)–Ocean island (OIB) diagram; (**c**) Island arc (IAB)–Continental rift (CRB)–Mid-Ocean ridge (MORB) diagram; (**d**) Island arc (IAB)–Ocean island (OIB)–Mid-Ocean ridge (MORB) diagram; and (**e**) Continental rift (CRB)–Ocean island (OIB)–Mid-Ocean ridge (MORB) diagram. All diagrams also include SCN and CAVA intermediate (int) magmas (52% < $(SiO_2)_{adj}$ < 63%), showing their differences in DF1 and DF2 parameters. Note that the inclusion of intermediate rocks is simply for highlighting the differences between these two provinces and not for identifying their probable tectonic setting.

primary magmas by considering a direct (slab melting) or indirect (fluid transport to the mantle) participation of the subducted Cocos plate.

(5) Spinel inclusions in olivine – Unlike Mg and Fe^{+2} in spinel trapped in olivine, magmatic abundances of trivalent (Al, Cr) and tetravalent (Ti) cations undergo very little, if any, change during post-entrapment re-equilibration because of their low diffusivity in olivine. For this reason, these cations have been used to discriminate between spinels that crystallised from different magmas in different geodynamic settings (Kamenetsky *et al.* 2001).

SCN chromian spinel inclusions in olivine phenocrysts have lower Cr/(Cr + Al) ratios (0.49±0.05; n=25; Figure 10a) compared to arc volcanic rocks, including boninites (>0.6), but similar or slightly lower than OIB (0.5–0.65; Dick & Bullen 1984; Kamenetsky *et al.* 2001). Also, SCN spinel inclusions display, in general, greater TiO_2 contents that those observed in subduction-related magmas (Figure 10b), reflecting a non-depleted source in HFSE.

(6) Partial melting (PM) model of lithospheric mantle – The failure of the slab-involvement model, as documented from geochemical, mineralogical, and isotopic constraints, suggests that the SCN near-primary magmas were generated solely in the underlying mantle. Following the criteria of Pearce & Peate (1995), trace-element ratios (Nb/Y ~0.65; Ti [in % m/m]/Yb ($mg.g^{-1}$) ~0.37; Th/Yb ~0.68; Zr/Yb ~ 80) indicate an enriched mantle source for SCN *M1* magmas, compared to N-MORB (Nb/Y ~0.083; Ti [in % m/m]/Yb ($mg.g^{-1}$) ~0.25; Th/Yb ~0.039; Zr/Yb ~ 24) or even E-MORB (Nb/Y ~0.29; Ti [in % m/m]/Yb ($mg.g^{-1}$) ~0.25; Th/Yb ~0.25; Zr/Yb ~ 31) compositions (Sun & McDonough 1989).

Trace element concentration data for near-primary *M1* magmas were used to develop a partial melting inversion model, in order to establish the 'average' geochemical characteristics of heterogeneous lithospheric mantle beneath the SCN. This approach was previously applied in the SCN by Velasco-Tapia & Verma (2001b), although based on a smaller number of samples and elements, as well as in other localities of the MVB (Verma 2004) and in the Los Tuxtlas volcanic field (LTVF, Figure 1, Verma 2006). The selected samples probably show olivine fractionation, as reflected by the variation of Ni content (117–200 $mg.g^{-1}$; Appendix A11), although the amount of fractionation may not be too large. About 5–15% removal of olivine could easily model the observed Ni concentration in the *M1* magmas from a primary magma in equilibrium with a peridotitic source. However, as a result of mineral/liquid partition coefficients <<1 for a typical upper mantle mineral assemblage (olivine, orthopyroxene, clinopyroxene, and spinel), this process will not produce any significant effect in the abundance of highly incompatible trace-elements or, more importantly, in their ratios (Rollinson 1993). Note

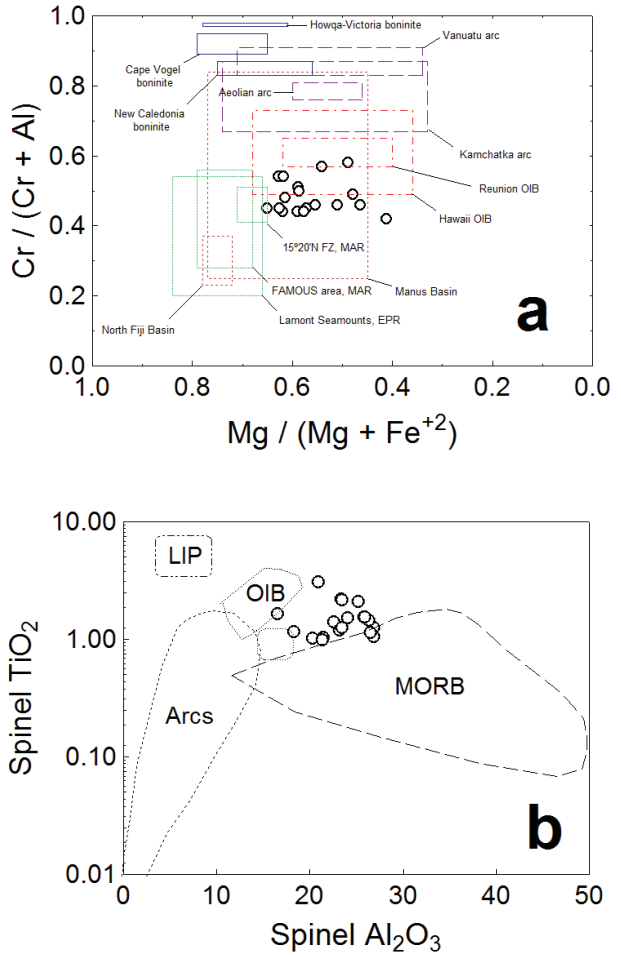

Figure 10. Compositional relationships in spinel inclusions in olivine ($Fo_{85.9\pm2.5}$) from SCN mafic magmas. **(a)** Cr/(Cr + Al) and Mg/(Mg + Fe^{+2}) ratios (in mol). For comparison, the diagram also includes spinel data from different geodynamic settings (Arc, Ocean Island, and Mid-Ocean ridge; Dick & Bullen 1984; Kamenetsky *et al.* 2001). (**b**) Al_2O_3 and TiO_2 (in %m/m). Discrimination between Mid-Ocean ridge (MORB), Arc, Ocean Island (OIB), and Large igneous province (LIP) tectonic settings (Kamenetsky *et al.* 2001).

that the inverse model assumes that the peridotitic source is uniform with respect to trace element concentrations (Hofmann & Feigenson 1983). Although this requirement is not easily met, similar radiogenic isotopic ratios of primary magmas would suggest a relative homogeneity of the source region. The SCN *M1* magmas display $^{87}Sr/^{86}Sr$ ratios of 0.70369±0.00027 (n= 10) and $^{143}Nd/^{144}Nd$= 0.51286±0.00005 (n= 9). Finally, an additional assumption in the inversion model is that melting occurs in an invariant condition, which in theory will give constant primary melt major element composition. The average SiO_2 (anhydrous 100% adjusted) concentration of the selected samples is 51.2±0.9 (n= 38). This relatively small variation in major

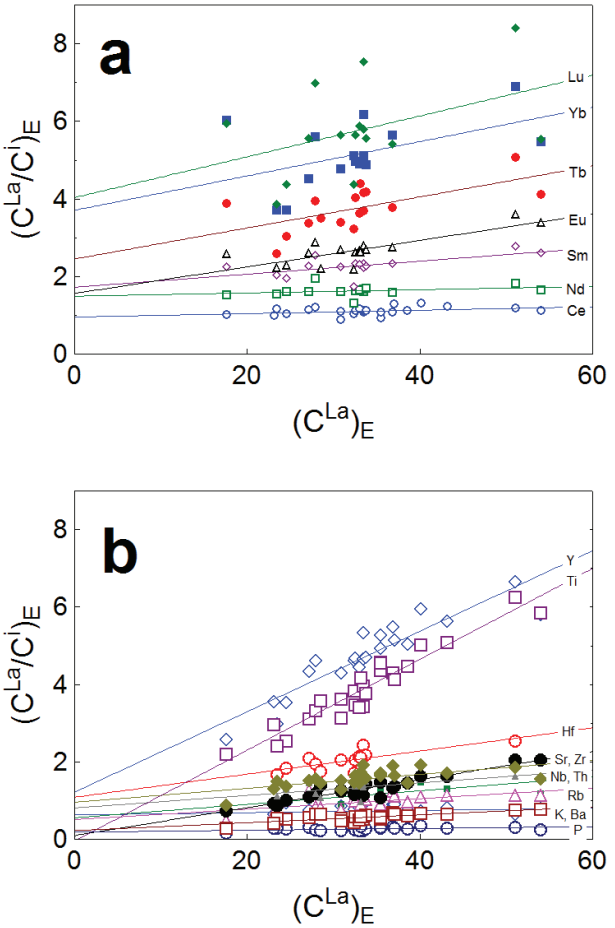

Figure 11. Inverse modelling $(C^{La}/C^{i})_E$ – $(C^{La})_E$ diagrams for SCN near primary magmas following the methodology proposed by Hofmann & Feigenson (1983). Subscript *E* refers to normalization with respect to silicate earth: concentration values used were those estimated by McDonough & Sun (1995). (**a**) Rare-earth elements (Ce to Lu) and (**b**) Large-ion lithophile elements (LILE): K, Rb, Ba, and Sr; High-field strength elements (HFSE): P, Nb, Th, Zr, Hf, Ti, and Y.

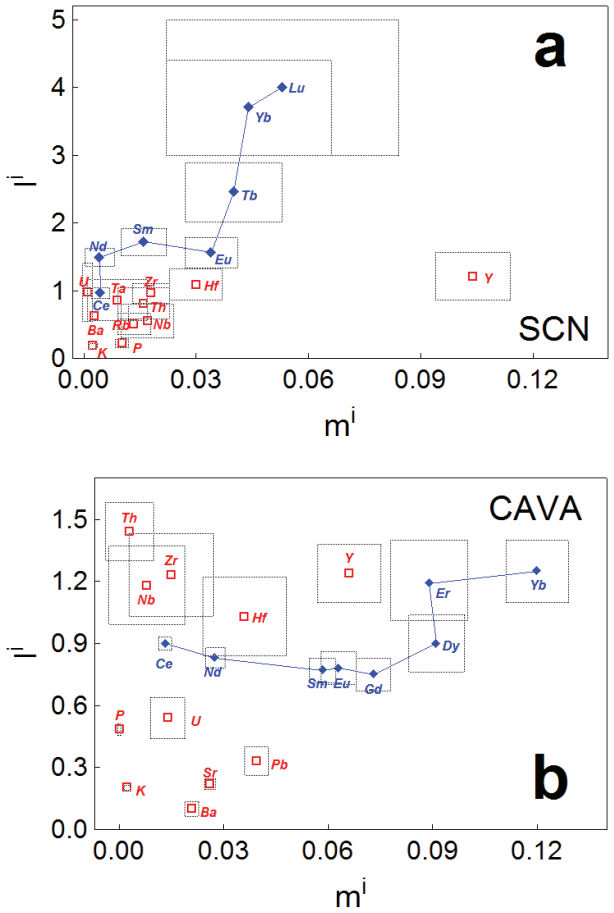

Figure 12. Diagrams of m^i – I^i (slope – intercept) for near primary magmas from (**a**) SCN and (**b**) CAVA (database downloaded from M.J. Carr's website: http://www.rutgers.edu/~carr, June 2004). The size for each rectangle (dashed lines) represents one standard error on the regression parameters, derived from the $(C^{La}/C^{i})_E$ – $(C^{La})_E$ diagrams (Figure 12 for SCN; CAVA diagram are not shown).

elements is to be expected in natural systems with a minimal effect on trace element compositions in the set of cogenetic magmas (Ormerod *et al.* 1991).

The inverse modelling method applied to the SCN primary magmas is the same as that proposed by Hofmann & Feigenson (1983). Relevant equations can be consulted in this paper as well as in Velasco-Tapia & Verma (2001b). La was used as the most incompatible element, because it shows, in general, lower bulk mineral/melt partition coefficients for olivine + orthopyroxene + clinopyroxene + spinel assemblage than other REE, LILE and HFSE (e.g., Rollinson 1993; Green 1994). The results of linear regression element-element $(C^{La} - C^{i})_E$ and element-element ratio $(C^{La} - C^{La}/C^{i})_E$ equations (where superscript *i* refers to a trace element other than La, and subscript *E* refers to normalisation against silicate earth-concentration values used, were those estimated by McDonough & Sun 1995) for the SCN near-primary magmas are presented in Appendix A14 and Figure 11. For REE with statistically valid correlations $(C^{La} - C^{i})_E$ at 95% confidence level and n ≥ 15, the incompatibility in $(C^{La} - C^{La}/C^{i})_E$ diagram decreases in the sequence from Ce (LREE) to Lu (HREE). For other trace-elements (n ³ 12), the incompatibility sequence is U > P ~ Ba > Ta ~ K > Rb > Th ~ Nb ~ Zr > Hf > Y.

For comparison, $(C^{La} - C^{i})_E$ and $(C_{La} - C_{La}/C_i)_E$ linear regressions (Appendix A15 and Figure 11) were prepared for near-primary magmas from the Central America Volcanic Arc database (downloaded from M.J. Carr's website: http://www.rutgers.edu/~carr, June 2004); CAVA petrogenesis has been clearly related to subduction of the

Cocos plate (Figure 1; Verma 2002 and references therein). REE incompatibility behaviour is similar to that observed in the SCN diagram, whereas the other trace elements show the incompatibility sequence P > K ~ Th > Nb > U ~ Zr > Ba > Sr > Hf ~ Pb > Y.

Intercept – slope (I^i – m^i) diagrams (Figure 12) were also prepared from SCN and CAVA $(C^{La} - C^{La}/C^i)_E$ linear regression models, in which:

$I^i = (C_0^{La} / C_0^i)(1 - P^i)$ and $m^i\ (D_0^i / C_0^i)$

where C_0^i refers to the concentration of element *i* in the mantle source, D_0^i the bulk distribution coefficient for source prior to melting, and P^i the bulk partition coefficient corresponding to the melting phases.

The slope values obtained from SCN linear regression models (Figure 12a) increase very slowly from Ce (0.0044) to Lu (0.053). For LREE (Ce and Nd), D_0^i ~0 and $(1 - P^i)$ ~1. The increase in the intercept value from LREE to HREE can be interpreted as a decrease in C_0^i, as a result of moderate compatibility in clinopyroxene (D^{cpx}= 0.5–0.6; Rollinson 1993). The large difference in I^{Ce} and I^{Yb} (ratio ~4; Appendix A14) implies an enriched source in LREE, with a mantle normalised ratio $(La/Yb)_N > 1$. However, positive intercepts of Tb to Lu are inconsistent with the presence of mineral phases with $D_0^i > 1$ for HREE, such as garnet in the source. On the other hand, LILE and HFSE display low slope values (m^i < 0.03), except for Y (m^i= 0.104). Note that HFSE elements (Y, Ta, Hf, Th, and Zr) are not as depleted as LREE and LILE, because they show low slope values (m^i= 0.009–0.030) combined with intercepts (I^i= 0.81–1.09) comparable to Ce (Nb showing lower intercept value). This behaviour contrasts with that observed in subduction-related magmas, because the latter are generally characterised by low concentrations of HFSE (Tatsumi & Eggins 1993), as also confirmed from the inverse modelling of CAVA data (see below).

Slope values of REE in the CAVA near-primary magmas increase very rapidly from Ce to Yb, reaching m^i= 0.12, whereas intercepts show a slight variation from Ce to Dy (I^i= 0.75–0.90) and increase their values in HFSE (Figure 12b). An I^{Yb}/I^{Ce} ~1.4 is indicative of a peridotitic source enriched in LREE but less than the mantle source of the SCN magmas. The remaining trace elements display low slope values (m^i= 0–0.04). However, LILE (K, Ba, and Sr) show lower intercept values (I^i= 0.1–0.2) than HFSE (Nb, Zr, Hf, and Th; I^i= 1.0–1.5). This decoupling is a typical characteristic of subduction-related magmas, reflecting depletion of HFSE in the mantle source compared to LILE (Ormerod *et al.* 1991).

6.2. Origin of high-Mg intermediate magmas

The origin of *HMI* magmas has been generally attributed to an arc setting derived from partial melting of the subducted oceanic plate (e.g., Yogodzinski *et al.* 1994; Kelemen 1995). According to Castillo (2006), such magmas display high $SiO_2 \geq 56$ %, $Al_2O_3 \geq 15\%$, Sr > 300 ppm, Sr/Y > 20, and La/Yb > 20, with no Eu anomaly in REE chondrite-normalized patterns and low Y < 15 ppm, Yb < 1.9 ppm, and $^{87}Sr/^{86}Sr < 0.704$. *HMI* magmas in the central MVB have been interpreted as arc-related adakites (e.g., Martínez-Serrano *et al.* 2004; Gómez-Tuena *et al.* 2007b). However, these 'adakite' samples do not plot on or even close to the subducting Cocos plate ('Downgoing slab') in the Sr-Nd isotopic diagram (Figure 6a; data not plotted).

HMI magmas have been also observed in zones where the volcanic activity is produced in an extensional tectonic setting (e.g., Kirin Province, northeast China; Hsu *et al.* 2000; Nighzhen, east China, Xu *et al.* 2002). Therefore, the presence of such magmas alone cannot be used to unequivocally infer the tectonic setting. *HMI* magmas from the SCN do not have isotopic ratios similar to the Cocos plate (Figure 6a). However, these rocks have Sr and Nd isotopic ratios similar to the *M* magmas. Mafic magmas may interact with mantle peridotite (Fisk 1986) or lower continental crust (Kelemen 1995) rich in residual olivine and probably, to a lesser extent, other common minerals fractionated from earlier batches of mafic magmas. This interaction is likely to move their compositions towards higher MgO and Ni contents (Fisk 1986), and the resulting magmas are likely to become basaltic andesite (Kelemen 1995). The Sr and Nd isotopic composition of these high-Mg intermediate magmas (Figure 6a) supports this mechanism for their genesis.

6.3. Origin of the evolved magmas

E1 and *E2* evolved magmas are petrologically important as they represent ~65% of the present SCN database. A consistent model should explain their relevant geochemical features as compared to the mafic magmas (Verma 1999) including: (a) generally lower REE concentrations; (b) similar Pb isotopic ratios but slightly higher $^{87}Sr/^{86}Sr$ and somewhat lower $^{143}Nd/^{144}Nd$; and (c) lower Nb concentrations and higher Ba/Nb ratios. A consistent model would also explain why the mineral compositions of olivine, spinel, and plagioclase of the SCN mafic and evolved magmas do not show statistically significant differences. Two viable mechanisms for explaining the genesis of the SCN evolved magmas were also suggested; these are: (a) the partial melting (~50%) of a heterogeneous mafic granulite source in the lower crust, and (b) a magma mixing process between the most evolved andesitic and dacitic magmas generated in the lower crust and the mantle-derived mafic magmas. However, Márquez & De Ignacio (2002) considered, without any quantitative thermal estimates of their own and not taking into account the presence of partial melts in the lower crust (Campos-Enríquez & Sánchez-Zamora 2000), that anatexis is not an appropriate model for genesis of the most evolved

magmas, as a high degree of partial melting (~50%) would be required and discrepancies exist between the predicted and measured LILE concentrations. As an alternative, these authors proposed the possibility that some evolved magmas were the result of partial melting of underplated mantle-derived magmas in the mantle-crust boundary under low water fugacity. This could well be a viable model but is not significantly different from that proposed by Verma (1999). The combined Sr-Nd isotope data from the Mexican lower crust and crustal xenoliths from the Popocatépetl stratovolcano (Figure 6b) are in general consistent with a significant crustal involvment in the genesis of SCN evolved magmas.

As Verma (1999) and Márquez & De Ignacio (2002) used a limited geochemical and isotopic database in hypothesis evaluation, the origin of SCN evolved magmas is still problematic. In the present study, several hypotheses were tested to explain their genesis.

(7) Fractional crystallisation (FC) model – In Figure 13 Harker diagrams of major- and trace-elements for the SCN evolved magmas and *M* magmas are presented. As expected, MgO and compatible element (e.g., Ni) contents diminish, up to four times, with the increment of $\%SiO_2$ in the SCN evolved magmas (linear correlation coefficient r of –0.901 and –0.713 for MgO (n= 289) and Ni (n= 259), respectively; statistically significant at 99% confidence level; Bevington & Robinson 2003). Also, LILE composition (e.g., K_2O and Ba) is increased two or three times, as expected, for the most felsic rocks (r of 0.716 and 0.265 for K_2O (n= 289) and Ba (n= 268), respectively). Initially, these observations could be explained as a result of fractional crystallisation. During progressive magma crystallisation, compatible elements are concentrated in the solids and incompatible elements are continuously enriched in the residual liquid. However, REE (e.g., La) concentrations do not increase with SiO_2 (Figure 13; r of –0.237, n= 207), although these elements are, in general, incompatible with respect to the mineral assemblage observed in the evolved rocks. In fact, SCN dacites have lower concentrations than mafic magmas (Appendix A11; Figure 14). A similar situation is true for HFSE (e.g., Nb, r= –0.433, n= 204; Figure 13; for other elements Appendix A11 and Figure 14), which precludes simple fractional crystallisation as a viable process for generating evolved magmas in the SCN. Additionally, small but significant differences in $^{87}Sr/^{86}Sr$ and, to a lesser extent, in $^{143}Nd/^{144}Nd$ (Figure 6) rule out a simple fractional crystallisation of mafic magmas to generate the SCN evolved magmas. Although Schaaf *et al.* (2005) proposed (polybaric) fractional crystallisation as the dominant process for the genesis of magmas from Popocatépetl and the SCN and Valle de Puebla areas, they failed to explain their REE data from this simple process. Verma (1999) had already commented on this problem for the SCN magmas. Additionally, their isotopic data will also rule out their proposed polybaric fractional crystallisation process as the main mechanism.

Nevertheless, we calculated detailed FC models using the average composition of basalt (B in Appendix A11) as the starting composition and common as well as accessory minerals (Figure 14). Note that the basaltic and basaltic andesite mafic magmas show higher REE concentrations than the evolved andesitic and dacitic magmas (compare B and BA with A and D in Figure 14a). The FC models, irrespective of whether common or accessory minerals are involved, show just the opposite, i.e., the liquids remaining after the removal of minerals would contain higher REE concentrations than the original basaltic magma (compare B with all L-FC patterns in Figure 14b). The multi-element plot for the SCN magmas (Figure 14c) shows that the evolved magmas have higher LILE (e.g., Rb and Ba) and Th and lower HFSE (e.g., Ta, Nb, P_2O_5, Zr, TiO_2, and Y) and REE (e.g., Sm and Yb). The FC modelling (Figure 14d), on the other hand, shows that most elements would increase in concentrations and thus the depletions of most HFSE, such as Nb, P, Ti and Y, cannot be easily modelled.

(8) Assimilation-fractional crystallisation (AFC) model – Mantle-derived mafic magmas can underplate or stall within the lower and/or upper continental crust, cool, fractionally crystallise, and provide latent heat to cause assimilation of country rock. Consequently, the *AFC* process in the SCN has been tested using major elements, REE, LILE, HFSE and $^{87}Sr/^{86}Sr$ ratios, applying the equations proposed by DePaolo (1981). *M1* average compositional data (B in Appendix A11) were used as initial magma concentrations. To evaluate petrogenetic processes in the SCN, compositions of mafic meta-igneous xenoliths from the San Luis Potosí area (Schaaf *et al.* 1994) had to be used by Verma (1999) as assimilant, but now new compositional data for crustal xenoliths from the nearby Popocatépetl stratovolcano (Figure 1) are available (Schaaf *et al.* 2005), which can be used to test the AFC process.

The bulk partition coefficients were calculated for several different mineralogies from mineral-liquid partition coefficients compiled by Torres-Alvarado *et al.* (2003) and Rollinson (1993) and used for AFC modelling different assimilants and assimilant/FC ratios r from 0.1 to 0.5. We report only the results of one such calculation (Figure 15). Although for a realistic AFC model, we should use a weighted estimate of mean values, we decided to illustrate this process by using the assimilant with the most extreme concentration values, that would cause the maximum effect in each case. These assimilants were as follows: A-ms (metasandstone) for Figure 15a and A-sk (skarn) for Figure 15b. In spite of this choice, in the bivariate Y-Ba/Nb diagram the liquids resulting from the AFC process move away from the trend of the SCN

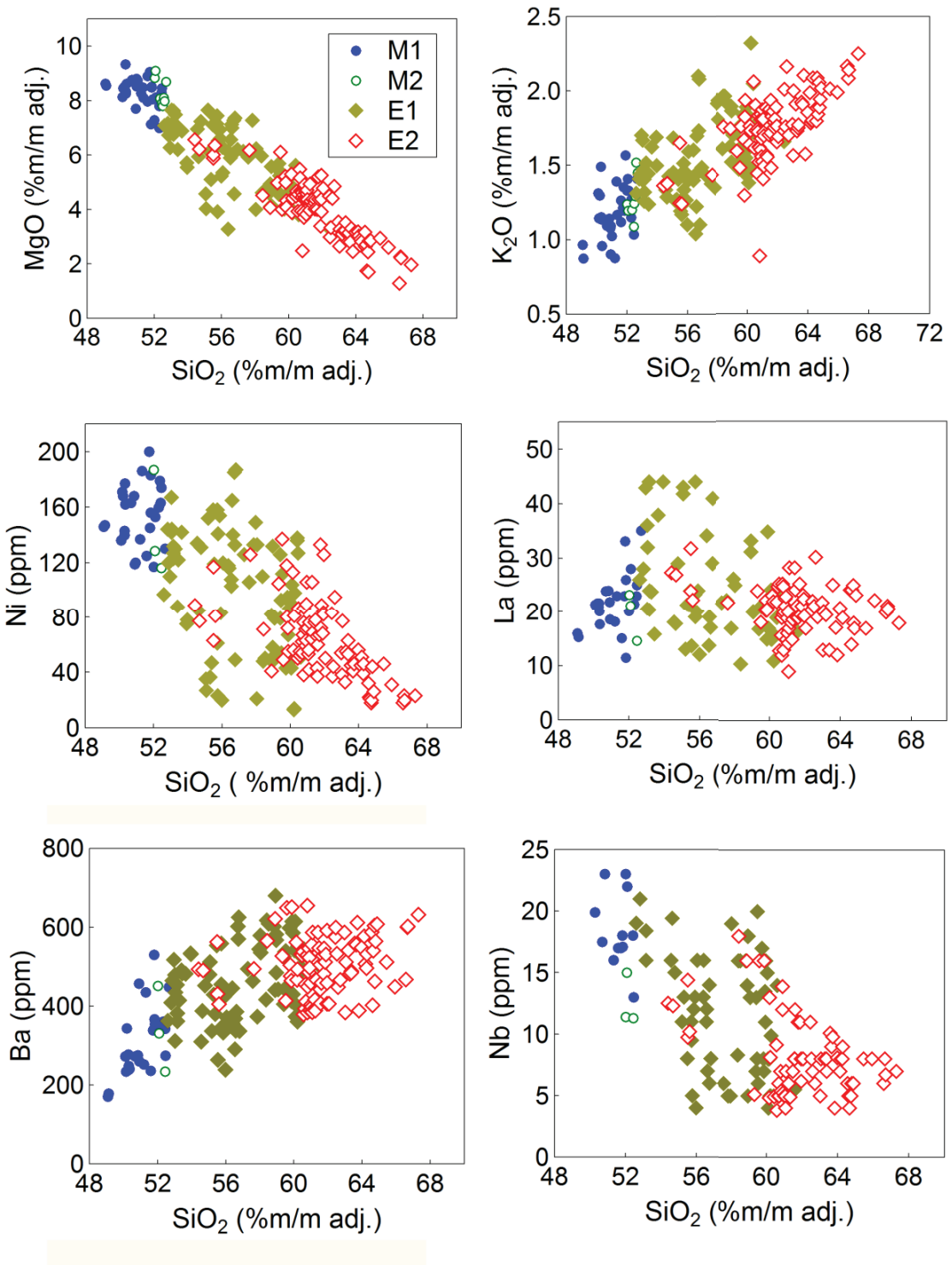

Figure 13. Harker diagrams for SCN mafic and evolved magmas. (**a**) MgO, (**b**) K_2O, (**c**) Ni, (**d**) La, (**e**) Ba, and (**f**) Nb.

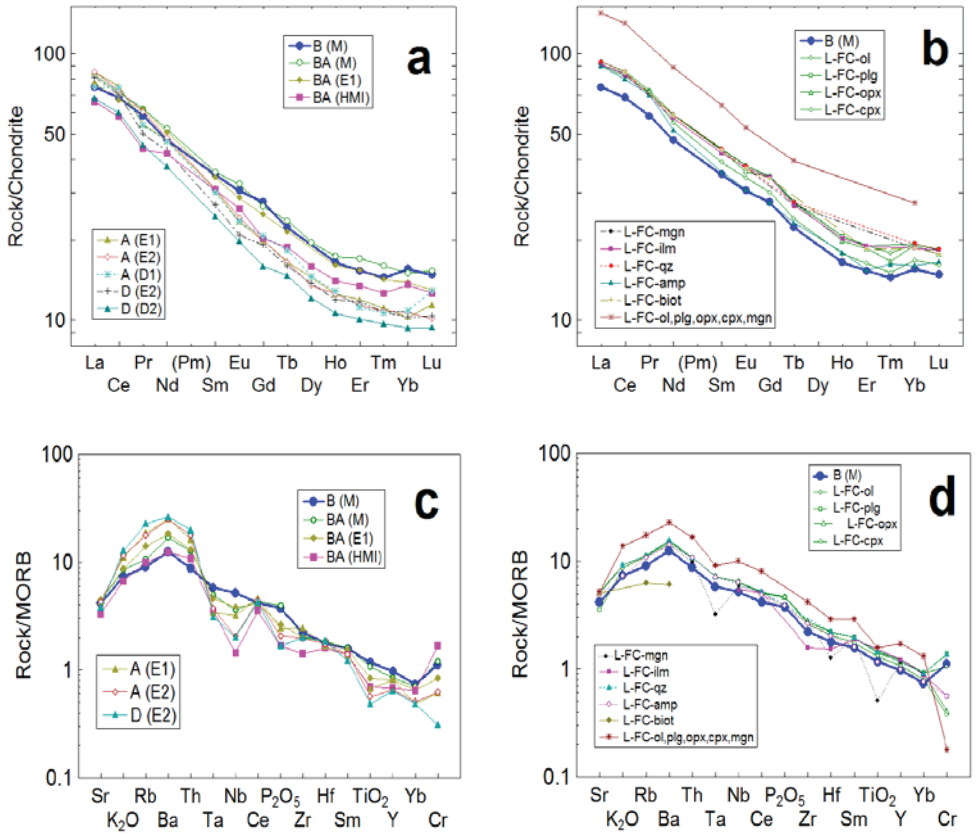

Figure 14. Chondrite-normalised REE and N-MORB-normalised multi-element diagrams for SCN average magma compositions and the FC models. The normalising values are as in Figures 4 and 5. For average compositions see Appendix A11. The partition coefficients were taken from the compilation by Torres-Alvarado *et al.* (2003) and Rollinson (1993). Although only equilibrium fractional crystallization curves are shown, the Rayleigh fractionation curves were also computed and observed to be very similar to those shown. The symbols are explained in the insets. (**a**) REE (B–basalt; BA– basaltic andesite; A– andesite; D– dacite; (M)– mafic; (E1)– evolved type 1; (HMI)– high-Mg intermediate; (E2)– evolved type 2; (Disq)– disequilibrium), (**b**) REE (the curves shown are for the equilibrium crystallization of 20% minerals from the original magma assumed to be B (M) type; the common minerals are ol– olivine, plg– plagioclase, opx– orthopyroxene, and cpx– clinopyroxene, whereas the accessory minerals modelled are mgn– magnetite, ilm– ilmenite, qz– quartz, amp– amphibole, and biot– biotite, an additional plausible FC model includes 50% crystallisation of olivine, plagioclase, orthopyroxene, clinopyroxene, and magnetite in the proportion of 0.30, 0.30, 0.20, 0.15, and 0.05), (**c**) multi-element plot for SCN (more information in **a**), and (**d**) multi-element plot for FC models (more information in **b**).

magmas (AFC curve with the fraction of remaining liquid F from 0.9 to 0.5 in Figure 15a), whereas in the chondrite-normalised diagram, all liquids remaining after AFC (corresponding to F from 0.9 to 0.7; Figure 15b) plot above the average basalt compositions away from the evolved SCN magmas, all of which plot below this mafic rock sample (see REE patterns for the andesite and dacitic rocks [A and D] in Figure 14a). Therefore, the AFC process does not seem to be appropriate to model the evolution of the SCN magmas.

(9) Continental crust partial melting – Information on the continental crustal structure along MVB has been provided essentially by gravimetric, seismic and magneto-telluric studies (e.g., Valdés *et al.* 1986; Molina-Garza & Urrutia-Fucugauchi 1993; Campos-Enríquez & Sánchez-Zamora 2000; Jording *et al.* 2000). Geophysical data analysis has revealed that the thickest continental crust is present around the Toluca and Mexico valleys (~47 km; ~14 kbars; 700–800°C for the lower crust), near the SCN volcanic field. Ortega-Gutiérrez *et al.* (2008) suggested

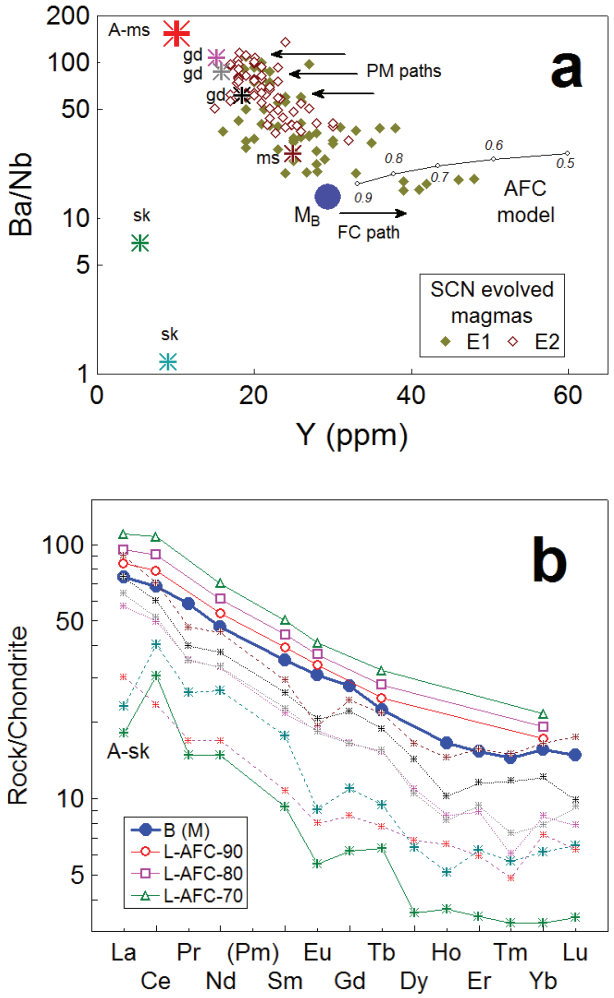

Figure 15. Evaluation of assimilation-fractional crystallisation (AFC) process for SCN magmas. AFC conditions: (1) Initial magma compositions: M_B– average composition of basalt (Appendix A11); (2) Assimilant/fractionated ratio (r) of 0.5 for fractions of liquid remaining (*F*) between 0.9 and 0.5; (3) FC mineral assemblages (solid line): 0.25 olivine + 0.40 plagioclase + 0.25 clinopyroxene + 0.10 magnetite; (4) Assimilant: Crustal xenolith (A-ms; meta-sandstone) from Popocatépetl (Schaaf *et al.* 2005) used for (a) and crustal xenolith (A-sk; skarn) for (b). Other crustal xenoliths are also shown in these plots. (**a**) Ba/Nb–Y plot, PM paths refer to partial melting of different xenoliths, whereas the FC path gives the possible trajectory of fractional crystallization of MB mafic magma; and (**b**) Chondrite-normalised plot, for symbols of crustal xenoliths see **(a)**.

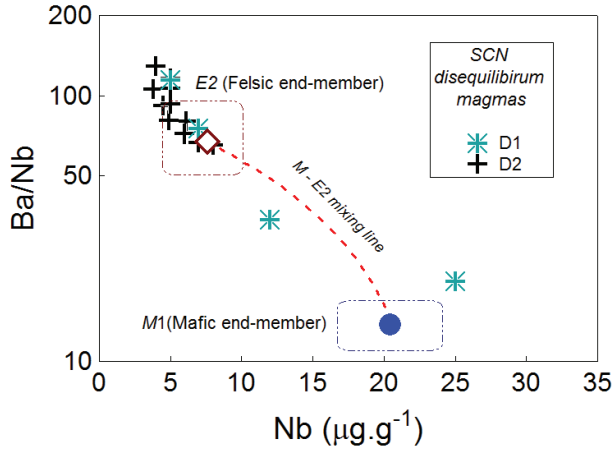

Figure 16. Nb-Ba/Nb bivariate diagram for SCN rocks. The symbols used are explained as an inset. A plausible mixing curve for *M-E2* magmas is included for reference to explain the origin of disequilibrium magmas.

that, under these physical conditions, garnet granulites of gabbroic composition and Mg# <60 should compose most of the lower crust underlying the central MVB.

From a seismic model, Fix (1975) interpreted a zone with ~20% partial melting below central Mexico in the crust-mantle interface. Ortega-Gutierrez *et al.* (2008) proposed that Mexican lower crust, even if wet, cannot melt at 700°C to produce andesitic magmas, but it certainly would do so for temperatures above 1000°C as modelled using temperature-stress dependent mantle rheologies. A periodic basaltic intrusion over a sustained but geologically short period could be a plausible mechanism to reach temperature above 1000°C at the crust-mantle interface in continental arc and other tectonic settings. Underplating of basaltic magma at the Moho and intrusion of basalt into the lower crust have been advocated for supplying heat for crustal anatexis (e.g., Bergantz 1989; Petford & Gallagher 2001). These mechanisms would result in heat transfer from the mantle to the lower crust, thus promoting melting. According to numerical simulations by Gallagher & Petford (2001), emplacing new basalt intrusions on top of earlier ones maximizes the amount of melt generated in the overlying protolith, and reduces greatly the heat loss through the base of the pile. The degree of partial melting is governed by the initial intrusion temperature and the periodicity, and yields a maximum predicted average melt fraction of 0.38. Dufek & Bergantz (2005) have modelled this process in 2-D for 30 to 50 km crusts in an arc environment. They pointed out that dacitic and rhyodacitic magmas can be generated in the crust although such magmas may not easily erupt at the surface. However, the eruption of such crustal melts may be facilitated in an extensional environment such as that inferred in the SCN (Márquez *et al.* 1999b).

The origin of some SCN felsic magmas has been interpreted as a product of partial melting of continental crust (Verma 1999). Because Mexican crust (e.g., Patchett & Ruiz 1987; Ruiz *et al.* 1998a, b; Roberts & Ruiz 1989; Heinrich & Besch 1992; Schaaf *et al.* 1994, 2005; Aguirre-Díaz *et al.* 2002) is highly heterogeneous both chemically

and isotopically, as is the crust elsewhere (Taylor & McLennan 1985; Rudnick *et al.* 1998), the magmas generated from its partial melting should also be similarly heterogeneous (Figure 6). Migration of SCN *M* and *HMI* melts upwards would result in crustal heating above the initial melting regions, and ultimately lead to assimilation and melting at shallower crustal levels. These petrological processes might be restricted to the middle crust (average worldwide composition: SiO_2= 60.6%, Al_2O_3= 15.5%, MgO= 3.4%, Rudnick & Gao 2003; depth in MVB= 10–25 km, Ortega-Gutiérrez *et al.* 2008), because SCN evolved magmas display little or no negative Eu anomaly in chondrite-normalized REE patterns. Evidence of entrapment of melt inclusions has been reported from upper to middle crust in central Mexico (1-6 kbar or less; Cervantes & Wallace 2003).

As revealed by xenoliths in volcanic rocks from the central part of the MVB, the crust is highly heterogeneous, because it consists of orthoquarzite sandstone, metasandstone, metasiltstone, xenocrystic quartz, calc-silicate skarn, foliated fine-grained granodiorite, coarse-grained pyroxene diorite to gabbro, fine-grained hornblende-biotite granodiorite, and marble (Márquez *et al.* 1999b; Siebe *et al.* 2004; Schaaf *et al.* 2005; Ortega-Gutiérrez *et al.* 2008). Partial melting of crustal xenoliths (gd in Figure 15a) can generate intermediate andesitic and dacitic SCN magmas (see PM paths in Figure 15a). The REE (Figure 15b) and Sr-Nd isotopic data (Figure 6a, b) of these xenoliths are also fully consistent with this partial melting model, because such melts are likely to have REE patterns below the B curve, i.e., similar to the evolved magmas (Figure 14a) and isotopic compositions similar to the SCN evolved magmas.

6.4. Origin of the disequilibrium magmas

DISQ magmas amounting to only ~7% represent incomplete mixing of at least two different types of magmas. Similar rock types with disequilibrium textures have also been observed in the nearby Iztaccíhuatl and Popocatépetl stratovolcanoes (Nixon 1988a, b; Straub & Martin del Pozzo 2001; Schaaf *et al.* 2005). Magma mixing is evaluated from one bivariate diagram (Figure 16). Mafic magmas show higher Nb concentrations than most other evolved magma varieties. Because Nb is an incompatible element in most common rock-forming minerals (e.g., Rollinson 1993), SCN magmas cannot be related to simple fractional crystallisation processes. Thus, the origin of the SCN evolved rocks with disequilibrium features could be explained as a result of the mixing of olivine-bearing mafic (*M*) magmas with evolved andesitic and dacitic (*E1* and *E2*) magmas generated by partial melting of the crust.

7. Conclusions

Compilation of 289 samples from the SCN shows that of the basaltic to dacitic magmas erupted, about 15% were mafic magmas. The $^{87}Sr/^{86}Sr$ and $^{143}Nd/^{144}Nd$ of these mafic magmas are 0.7035–0.7043 and 0.51279–0.51294. In comparison, the evolved magmas have Sr and Nd isotopic compositions of 0.7036–0.7048 and 0.51270–0.51230 (slightly higher and lower, respectively). All samples from the SCN plot on the 'mantle array' in the Sr-Nd isotope diagram. Spinel inclusions in olivines have compositions different from those in arcs. Some of the evolved magmas show abundant textural evidence of mineralogical disequilibrium, such as coexisting olivine and quartz, quartz with pyroxene reaction rims, and plagioclase with oscillatory or complex zoning. On multi-dimensional log-ratio transformed major-element discriminant function based diagrams, most (93–100%) mafic rock samples plot in the continental rift setting. Similar multi-dimensional immobile element based diagrams support this conclusion. Inverse modelling of trace-element data for the SCN mafic magmas shows a source enriched in LILE, HFSE and LREE and absence of residual garnet. This modelling also shows the following incompatibility sequence for the SCN: U > P ~ Ba > Ta ~ K > Rb > Th ~ Nb ~ Zr > Hf > Y. In comparison, the incompatibility sequence for the CAVA was as follows: P > K ~ Th > Nb > U ~ Zr > Ba > Sr > Hf ~ Pb > Y. Evolved magmas from the SCN show a more complex history, although the involvement of the continental crust, particularly the lower crust, might be considered significant. Our preferred petrogenetic model for the SCN can be summarised as follows: (1) mantle-derived basic (basaltic) magmas intruded the base of the continental crust; (2) their periodic injection resulted in a significant increase in crustal temperatures to cause partial melting of the crust which produced evolved andesitic and dacitic magmas and their eruption was facilitated by an extensional regime beneath the SCN; and (3) fractional crystallisation of basic magmas and their incomplete mixing with the evolved magmas gave rise to disequilibrium magmas.

Acknowledgements

We are grateful to Gabriela Solís Pichardo and Juan Julio Morales Contreras (LUGIS, UNAM); Mirna Guevara (CIE, UNAM); and Rufino Lozano and Patricia Girón (IG, UNAM) for help with chemical and isotopic analyses, to Francisco Anguita, Álvaro Márquez and José González de Tánago (Facultad de Ciencias Geológicas, Universidad Complutense de Madrid) for making the microprobe determinations possible, and to Alfredo Quiroz Ruiz for maintaining our computers and helping us with the preparation of final electronic format of the Figures. Thanks are also due to Programa de Intercambio de Personal Académico UNAM-UANL. We are also grateful to three anonymous reviewers for critical reviews as well as the Editor-in-Chief Erdin Bozkurt for allowing us to improve our presentation.

References

Agostini, S., Corti, G., Doglioni, C., Carminati, E., Innocenti, F., Tonarini, S., Manetti, P., Di Vincenzo, G. & Montanari, D. 2006. Tectonic and magmatic evolution of the active volcanic front in El Salvador: insight into the Berlín and Ahuachapán geothermal areas. *Geothermics* **35**, 368–408.

Agrawal, S. 1999. Geochemical discrimination diagrams: a simple way of replacing eye-fitted boundaries with probability based classifier surfaces. *Journal of the Geological Society of India* **54**, 335–346.

Agrawal, S., Guevara, M. & Verma, S.P. 2008. Tectonic discrimination of basic and ultrabasic rocks through log-transformed ratios of immobile trace elements. *International Geology Review* **50**, 1057–1079.

Aguirre-Díaz, G.J., Dubois, M., Laureyns, J. & Schaaf, P. 2002. Nature and P-T conditions of the crust beneath the central Mexican Volcanic Belt based on Precambrian crustal xenolith. *International Geology Review* **44**, 222–242.

Aitchison, J. 1986. *The Statistical Analysis of Compositional Data.* Chapman and Hall, London.

Alaniz-Alvarez, S.A., Nieto-Samaniego, A.F. & Ferrari, L. 1998. Effect of strain rate in the distribution of monogenetic and polygenetic volcanism in the Transmexican Volcanic Belt. *Geology* **26**, 591–594.

Alvarado, G.E., Soto, G.J., Schmincke, H.-U., Bolge, L.L. & Sumita, M. 2006. The 1968 andesitic lateral blast eruption at Arenal volcano, Costa Rica. *Journal of Volcanology and Geothermal Research* **157**, 9–33.

Bardintzeff, J.M. & Deniel, C. 1992. Magmatic evolution of Pacaya and Cerro Chiquito volcanological complex, Guatemala. *Bulletin of Volcanology* **54**, 267–283.

Barnett, V. & Lewis, T. 1994. *Outliers in Statistical Data*. John Wiley & Sons, Chichester.

Bevington, P.R. & Robinson, D.K. 2003. *Data Reduction and Error Analysis for the Physical Sciences.* Mc-Graw Hill, Boston.

Bergantz, G.W. 1989. Underplating and partial melting: implications for melt generation and extraction. *Science* **245**, 1093–1095.

Blatter, D.L., Farmer, G.L. & Carmichael, I.S.E. 2007. A north-south transect across the Central Mexican Volcanic Belt at ~100°W: spatial distribution, petrological, geochemical and isotopic characteristics of Quaternary volcanism. *Journal of Petrology* **48**, 901–950.

Bloomfield, K. 1975. A late-Quaternary monogenetic volcano field in central Mexico. *Geologische Rundschau* **64**, 476–497.

Bolge, L.L., Carr, M.J., Feigenson, M.D. & Alvarado, G.E. 2006. Geochemical stratigraphy and magmatic evolution at Arenal volcano, Costa Rica. *Journal of Volcanology and Geothermal Research* **157**, 34–48.

Cabanis, B. & Lecolle, M. 1989. Le diagramme La/10-Y/15-Nb/8: un outil pour la discrimination des séries volcaniques et la mise en évidence des processus de mélange et/ou de contamination crustale. *Comptes Rendus Academie de Sciences Paris Serie II* **309**, 2023–2029.

Cameron, B.I., Walker, J.A., Carr, M.J., Patino, L.C., Matías, O. & Feigenson, M.D. 2002. Flux versus decompression melting at stratovolcanoes in southeastern Guatemala. *Journal of Volcanology and Geothermal Research* **119**, 21–50.

Campos-Enríquez, J.O. & Sánchez-Zamora, O. 2000. Crustal structure across southern Mexico inferred from gravity data. *Journal of South American Earth Sciences* **13**, 479–489.

Carr, M.J. 1984. Symmetrical and segmented variation of physical and geochemical characteristics of the Central American volcanic front. *Journal of Volcanology and Geothermal Research* **20**, 231–252.

Carr, M.J., Feigenson, M.D. & Bennett, E.A. 1990. Incompatible element and isotopic evidence for tectonic control of source mixing and melt extraction along the Central America arc. *Contributions to Mineralogy and Petrology* **105**, 369–380.

Castillo, P. 2006. An overview of adakite petrogenesis. *Chinese Science Bulletin* **51**, 257–268.

Cervantes, P. & Wallace, P.J. 2003. Role of H_2O in subduction-zone magmatism: New insights from melt inclusions in high-Mg basalts from central Mexico. *Geology* **31**, 235–238.

Córdova, C., Martin del Pozzo, A.L. & López, C.J. 1994. Paleolandforms and volcanic impact on the environment of Prehistoric Cuicuilco, southern Mexico City. *Journal of Archeology Science* **21**, 585–596.

De Cserna, Z., Fries, C., Rincón-Orta, C., Silver, T.L., Westley, H., Solorio-Munguía, J. & Schmitter-Villada, E. 1974. Datos geocronométricos terciarios de los Estados de México, Morelos y Guerrero. *Boletín de la Asociación Mexicana de Geólogos Petroleros* **26**, 263–273.

Deer, W.A., Howie, A.R. & Zusmann, J. 1997. *Rock Forming Minerals*. Longman, London.

Delgado, H., Molinero, R., Cervantes, P., Nieto-Obregón, J., Lozano-Santa Cruz, R., Macías-González, H.L., Mendoza-Rosales, C. & Silva Romo, G. 1998. Geology of Xitle volcano in southern Mexico City, a 2000-year old monogenetic volcano in an urban area. *Revista Mexicana de Ciencias Geológicas* **15**, 115–131.

Delgado-Granados, H. & Martín del Pozo, A.L. 1993. Pliocene to Holocene volcanic geology at the junction of Las Cruces, Chichinautzin and Ajusco ranges, southwest of Mexico City. *Geofísica Internacional* **32**, 511–522.

DePaolo, D.J. 1981. Trace element and isotopic effects of combined wallrock assimilation and fractional crystallisation. *Earth and Planetary Science Letters* **53**, 189–202.

Dick, H.J.B. & Bullen, T. 1984. Chromian spinel as a petrogenetic indicator in abyssal and alpine-type peridotites and spatially associated lavas. *Contributions of Mineralogy and Petrology* **86**, 54–76.

Doglioni, C., Carminati, E., Cuffaro, M. & Scrocca, D. 2007. Subduction kinematics and dynamic constraints. *Earth-Science Reviews* **83**, 125–175.

Droop, G.T.R. 1987. A general equation for estimating Fe^{+3} concentrations in ferromagnesian silicates and oxides from microprobe analyses, using stoichiometric criteria. *Mineralogical Magazine* **51**, 431–435.

Dufek, J. & Bergantz, GVW. 2005. Lower crustal magma genesis and preservation: a stochastic framework for the evaluation of basalt-crust interaction. *Journal of Petrology* **46**, 2167–2195.

Ego, F. & Ansan, V. 2002. Why is the Central Trans-Mexican Volcanic Belt (102°–99°W) in transtensive deformation? *Tectonophysics* **359**, 189–208.

Faure, G. 1986. *Principles of Isotope Geology.* Wiley, New York.

Ferrari, L. 2004. Slab detachment control on mafic volcanic pulse and mantle heterogeneity in central Mexico. *Geology* **32**, 77–80.

Ferrari, L., Petrone, C.M. & Francalanci, L. 2001. Generation of oceanic-island basalt-type volcanism in the western Trans-Mexican volcanic belt by slab rollback, asthenosphere infiltration, and variable flux melting. *Geology* **29**, 507–510.

Fisk, M.R. 1986. Basalt magma interaction with harzburgite and the formation of high-magnesium andesites. *Geophysical Research Letters* **13**, 467–470.

Fix, J.E. 1975. The crust and the upper mantle of central Mexico. *Geophysical Journal of the Royal Astronomical Society* **43**, 453–499.

Fries, C. 1960. Geología de Estado de Morelos y partes adyacentes de México y Guerrero, región central meridional de México. *Boletín del Instituto de Geología, UNAM* **60**, 1–236.

Gallagher, K. & Petford, N. 2001. Partial melting of mafic (amphibolitic) lower crust by periodic influx of basaltic magma. *Earth and Planetary Science Letters* **193**, 483–499.

Gamble, J.A., Wright, I.C., Woodhead, J.D. & McCulloch, M.T. 1995. Arc and back-arc geochemistry in the southern Kermadec arc-Ngatoro basin and offshore Taupo volcanic zone, SW Pacific. *In*: Smellie, J.L. (ed), *Volcanism Associated with Extension at Consuming Plate Margins*. Geological Society Special Publication **81**, 193–212.

García-Palomo, A., Macías, J.L. & Garduño, V.H. 2000. Miocene to Recent structural evolution of the Nevado de Toluca volcano region, Central Mexico. *Tectonophysics* **318**, 281–302.

García-Palomo, A., Macías, J.L., Arce, J.L., Capra, L., Garduño, V.H. & Espíndola, J.M. 2002. *Geology of Nevado de Toluca Volcano and Surrounding Areas, Central Mexico.* 1:100 000 Scale Geological Map and Explanatory Text. Geological Society of America Map and Chart Series **MCH089**, 1–26.

Gomberg, J.S. & Masters, T.G. 1988. Waveform modelling using locked-mode synthetic and differential seismograms: application to determination of the structure of Mexico. *Geophysical Journal* **94**, 193–218.

Gómez-Tuena, A., Langmuir, C.H., Goldstein, S.L., Straub, S.M. & Ortega-Gutiérrez, F. 2007b. Geochemical evidence for slab melting in the Trans-Mexican Volcanic Belt. *Journal of Petrology* **48**, 537–562.

Gómez-Tuena, A., Orozco-Esquivel, T. & Ferrari, L. 2007a. Igneous petrogenesis of the Trans-Mexican Volcanic Belt. *In*: Alaniz-Álvarez, S.A. & Nieto-Samaniego, A.F. (eds), *Geology of Mexico: Celebrating the Centenary of the Geological Society of Mexico*. Geological Society of America Special Paper **442**, 129–181.

Green, T.H. 1994. Experimental studies of trace-element partitioning applicable to igneous petrogenesis: Sedona 16 years later. *Chemical Geology* **117**, 1–16.

Guevara, M., Verma, S.P., Velasco-Tapia, F., Lozano-Santa Cruz, R. & Girón, P. 2005. Comparison of linear regression models for quantitative geochemical analysis: an example using X-Ray Fluorescence Spectrometry. *Geostandards and Geoanalytical Research* **29**, 271–284.

Haggerty, S.E. 1991. Oxide mineralogy of the upper mantle. *In*: Lindsley, D.H. (ed), *Oxide Minerals: Petrologic and Magnetic Significance*. Reviews in Mineralogy **25**, 355–416.

Haskin, L.A., Haskin, M.A., Frey, F.A. & Wildeman, T.R. 1968. Relative and absolute terrestrial abundances of the rare earths. *In*: Ahrens, L.H. (ed), *Origin and Distribution of the Elements*. Pergamon Press, Oxford, 889–912.

Hawkesworth, C.J., Hergt, J.M., Ellam, R.M. & McDermott, F. 1991. Element fluxes associated with subduction related magmatism. *Royal Society of London Philosophical Transactions* **335**, 393–405.

Hawkesworth, C.J., O'Nions, R.K., Pankhurst, R.J., Hamilton, P.J. & Evensen, E.M. 1977. A geochemical study of island-arc and back-arc tholeiites from the Scotia Sea. *Earth and Planetary Science Letters* **36**, 153–162.

Hazlett, R.W. 1987. Geology of San Cristobal volcanic complex, Nicaragua. *Journal of Volcanology and Geothermal Research* **33**, 223–230.

Heinrich, W. & Besch, T. 1992. Thermal history of the upper mantle beneath a young back-arc extensional zone: ultramafic xenoliths from San Luis Potosí, central Mexico. *Contributions to Mineralogy and Petrology* **111**, 126–142.

Henry, C.D. & Aranda-Gomez, J.J. 1992. The real southern Basin and Range: mid-to late Cenozoic extension in Mexico. *Geology* **20**, 701–704.

Hofmann, A.W. & Feigenson, M.D. 1983. Case studies on the origin of basalt. I. Theory and reassessment of Grenada basalts. *Contributions to Mineralogy and Petrology* **84**, 382–389.

Hoogewerff, J.A., van Bergen, M.J., Vroon, P.Z., Hertogen, J., Wordel, R., Sneyers, A., Nasution, A., Varekamp, J.C., Moens, H.L.E. & Mouchel, D. 1997. U-series, Sr-Nd-Pb isotope and trace-element systematics across an active island arc-continent collision zone: implications for element transfer at the slab-wedge interface. *Geochimica et Cosmochimica Acta* **61**, 1057–1072.

Hsu, C.-N., Chen, J.-C. & Ho, K.-S. 2000. Geochemistry of Cenozoic volcanic rocks from Kirin Province, northeast China. *Geochemical Journal* **34**, 33–58.

Husker, A. & Davis, P.M. 2009. Tomography and thermal state of the Cocos plate subduction beneath Mexico City. *Journal of Geophysical Research* **114**, B04306, doi: 10.1029/2008JB006039.

Jarosewich, E., Nelen, J.A. & Norberg, J.A. 1980. Reference samples for electron microprobe analysis. *Geostandards Newsletter* **4**, 43–47.

Johnson, C.A. & Harrison, C.G.A. 1990. Neotectonics in central Mexico. *Physics of Earth and Planetary Interiors* **64**, 187–210.

Jording, A., Ferrari, L., Arzate, J. & Jödicke, H. 2000. Crustal variations and terrane boundaries in southern Mexico as imaged by magnetotelluric transfer functions. *Tectonophysics* **327**, 1–13.

Jödicke, H., Jording, A., Ferrari, L., Arzate, J., Mezger, K. & Rüpke, L. 2006. Fluid release from the subducted Cocos plate and partial melting of the crust deduced from magnetotelluric studies in southern Mexico: implications for the generation of volcanism and subduction dynamics. *Journal of Geophysical Research* **111**, B08102, doi: 10.1029/2005JB003739.

Kamenetsky, V.S., Crawford, A.J. & Meffre, S. 2001. Factors controlling chemistry of magmatic spinel: an empirical study of associated olivine, Cr-spinel and melt inclusions from primitive rocks. *Journal of Petrology* **42**, 655–671.

Kay, S.M., Maksaev, V., Moscoso, R., Mpodozis, C. & Nasi, C. 1987. Probing the evolving Andean lithosphere: Mid-late Tertiary magmatism in Chile (29°–30°30'S) over the modern zone of subhorizontal subduction. *Journal of Geophysical Research* **92**, 6173–6189.

Kearey, P., Klepeis, K.A. & Vine, F.J. 2009. *Global Tectonics*. Wiley-Blackwell, New York.

Keith, M. 2001. Evidence for a plate tectonics debate. *Earth-Science Reviews* **55**, 235–336.

Kelemen, P.B. 1995. Genesis of high Mg# andesites and the continental crust. *Contributions to Mineralogy and Petrology* **120**, 1–19.

Kepezhinskas, P. 1995. Diverse shoshonite magma series in the Kamchatka arc: relationships between intra-arc extension and composition of alkaline magmas. *In:* Smellie, J.L. (ed), *Volcanism Associated with Extension at Consuming Plate Margins.* Geological Society Special Publication **81**, 249–264.

Le Bas, M.J. 2000. IUGS reclassification of the high-Mg and picritic volcanic rocks. *Journal of Petrology* **41**, 1467–1470.

Le Bas, M.J., LeMaitre, R., Streckeisen, A. & Zanettin, B. 1986. A chemical classification of volcanic rocks based on the total alkali-silica diagram. *Journal of Petrology* **27**, 745–750.

Luhr, J.F. 1997. Extensional tectonics and the diverse primitive volcanic rocks in the western Mexican Volcanic Belt. *Canadian Mineralogist* **35**, 473–500.

Luhr, J.F., Nelson, S.A., Allan, J.F. & Carmichael, I.S.E. 1985. Active rifting in southwestern Mexico: manifestations of an incipient eastward spreading-ridge jump. *Geology* **13**, 54–57.

Luhr, J.F., Allan, J.F., Carmichael, I.S.E., Nelson, S.A. & Hasenaka, T. 1989. Primitive calc-alkaline and alkaline rock types from the western Mexican Volcanic Belt. *Journal of Geophysical Research* **94**, 4515–4530.

Márquez, A. & De Ignacio, C. 2002. Mineralogical and geochemical constraints for the origin and evolution of magmas in Sierra Chichinautzin, Central Mexican Volcanic Belt. *Lithos* **62**, 35–62.

Márquez, A., Oyarzun, R., Doblas, M. & Verma, S.P. 1999a. Alkalic (ocean-island basalt type) and calc-alkalic volcanism in the Mexican Volcanic Belt: a case for plume-related magmatism and propagating rifting at an active margin? *Geology* **27**, 51–54.

Márquez, A., Oyarzun, R., de Ignacio, C. & Doblas, M. 2001. Southward migration of volcanic activity in the central Mexican Volcanic Belt: asymmetric extension within a two-layer crustal stretching model. *Journal of Volcanology and Geothermal Research* **112**, 175–187.

Márquez, A., Verma, S.P., Anguita, F., Oyarzun, R. & Brandle, J.L. 1999b. Tectonics and volcanism of Sierra Chichinautzin: extension at the front of the Central Trans-Mexican Volcanic belt. *Journal of Volcanology and Geothermal Research* **93**, 125–150.

Martín del Pozzo, A.L. 1982. Monogenetic volcanism in Sierra Chichinautzin, Mexico. *Bulletin Volcanologique* **45**, 9–24.

Martínez-Serrano, R.G., Schaaf, P., Solís-Pichardo, G., Hernández-Bernal, M.S., Hernández-Treviño, T., Morales-Contreras, J.J. & Macías, J.L. 2004. Sr, Nd and Pb isotope and geochemical data from the Quaternary Nevado de Toluca volcano, a source of recent adakitic magmatism, and the Tenango Volcanic Field, Mexico. *Journal of Volcanology and Geothermal Research* **138**, 77–110.

Martinod, J., Husson, L., Roperch, P., Guillaume, B. & Espurt, N. 2010. Horizontal subduction zones, convergence velocity and the building of the Andes. *Earth and Planetary Science Letters* **299**, 299–309.

McDonough, W.F. & Sun, S.-S. 1995. The composition of the Earth. *Chemical Geology* **120**, 223–253.

Meriggi, L., Macías, J.L., Tommasini, S., Capra, L. & Conticelli, S. 2008. Heterogeneous magmas of the Quaternary Sierra Chichinautzin volcanic field (central Mexico): the role of an amphibole-bearing mantle and magmatic evolution processes. *Revista Mexicana de Ciencias Geológicas* **25**, 197–216.

Meschede, M. 1986. A method of discriminating between different types of mid-ocean ridge basalts and continental tholeiites with the Nb-Zr-Y diagram. *Chemical Geology* **56**, 207–218.

Middlemost, E.A.K. 1989. Iron oxidation ratios, norms and the classification of volcanic rocks. *Chemical Geology* **77**, 19–26.

Molina-Garza, R. & Urrutia-Fucugauchi, J. 1993. Deep crustal structure of central Mexico derived from interpretation of Bouger gravity anomaly data. *Journal of Geodynamics* **17**, 181–201.

Molnar, P. & Sykes, L.R. 1969. Tectonics of the Caribbean and Middle America regions from focal mechanisms and seismicity. *Geological Society of America Bulletin* **80**, 1639–1684.

Moore, G., Marone, C., Carmichael, I.S.E. & Renne, P. 1994. Basaltic volcanism and extension near the intersection of the Sierra Madre volcanic province and the Mexican Volcanic Belt. *Geological Society of America Bulletin* **106**, 383–394.

Mooser, F., Montiel, A. & Zuñiga, A. 1996. *Nuevo mapa geológico de las cuencas de México, Toluca y Puebla. Estratigrafía, tectónica regional y aspectos geotérmicos.* Internal Report, Comisión Federal de Electricidad, Mexico City.

Mora Alvarez, G., Caballero Miranda, C., Urrutia Fucugauchi, J. & Uchiumi, S. 1991. Southward migration of volcanic activity in the Sierra de las Cruces, basin of Mexico? – A preliminary K-Ar dating and paleomagnetic study. *Geofísica Internacional* **30**, 61–70.

Morán-Zenteno, D.J., Alba-Aldave, L.A., Martínez-Serrano, R.G., Reyes-Salas, M.A., Corona-Esquivel, R. & Ángeles-García, S. 1998. Stratigraphy, geochemistry and tectonic significance of the Tertiary volcanic sequence of the Taxco-Tilzapotla region, southern Mexico. *Revista Mexicana de Ciencias Geológicas* **15**, 167–180.

Mori, L., Gómez-Tuena, A., Schaaf, P., Goldstein, S.J., Pérez-Arvizu, O. & Solís-Pichardo, G. 2009. Lithospheric removal as a trigger for flood basalt magmatism in the Trans-Mexican Volcanic Belt. *Journal of Petrology* **50**, 2157–2186.

Nakamura, N. 1974. Determination of REE, Ba, Fe, Mg, Na and K in carbonaceous and ordinary chondrites. *Geochimica et Cosmochimica Acta* **38**, 757–775.

Nelson, B.K. 1995. Fluid flow in subduction zones: evidence from Nd- and Sr-isotope variations in metabasalts of the Franciscan complex, California. *Contributions to Mineralogy and Petrology* **119**, 247–262.

Nixon, G.T. 1988a. Petrology of younger andesites and dacites of Iztaccíhuatl volcano, Mexico: I. Disequilibrium phenocrysts assemblages as indicators of magma chamber processes. *Journal of Petrology* **29**, 213–264.

Nixon, G.T. 1988b. Petrology of younger andesites and dacites of Iztaccíhuatl volcano, Mexico: II. Chemical stratigraphy, magma mixing, and the composition of basaltic magma influx. *Journal of Petrology* **29**, 265–303.

Ormerod, D.S., Rogers, N.W. & Hawkesworth, C.J. 1991. Melting in the lithospheric mantle: inverse modelling of alkali-olivine basalts from the Big Pine Volcanic Field, California. *Contributions to Mineralogy and Petrology* **108**, 305–317.

Ortega-Gutiérrez, F., Elías-Herrera, M. & Dávalos-Elizondo, M.G. 2008. On the nature and role of the lower crust in the volcanic front of the Trans-Mexican Volcanic Belt and its fore-arc region, southern and central Mexico. *Revista Mexicana de Ciencias Geológicas* **25**, 346–364.

Osete, M.L., Ruiz-Martínez, V.C., Caballero, C., Galindo, C., Urrutia-Fucugauchi, J. & Tarling, D.H. 2000. Southward migration of continental volcanic activity in the Sierra de las Cruces, Mexico: paleomagnetic and radiometric evidence. *Tectonophysics* **318**, 201–215.

Pacheco, J.F. & Singh, S.K. 2010. Seismicity and state of stress in Guerrero segment of the Mexican subduction zone. *Journal of Geophysical Research* **115**, doi:10.1029/2009JB006453.

Pardo, M. & Suárez, G. 1995. Shape of the subducted Rivera and Cocos plates in southern Mexico: seismic and tectonic implications. *Journal of Geophysical Research* **100**, 12357–12373.

Patchett, P.J. & Ruiz, J. 1987. Nd isotopic ages of crustal formation and metamorphism in the Precambrian of eastern and southern Mexico. *Contributions to Mineralogy and Petrology* **96**, 523–528.

Pearce, J.A. 1982. Trace element characteristics of lavas from destructive plate boundaries. *In:* Thorpe, R.S. (ed), *Andesites*. John Wiley & Sons, Chichester, 525–548.

Pearce, J.A. & Cann, J.R. 1973. Tectonic setting of the basic volcanic rocks determined using trace element analyses. *Earth and Planetary Science Letters* **19**, 290–300.

Pearce, J.A. & Peate, D.W. 1995. Tectonic implications of the composition of volcanic arc magmas. *Annual Review of Earth and Planetary Science* **23**, 251–285.

Pérez-Campos, X., Kim, Y., Husker, A., Davis, P.M., Clayton, R.W., Iglesias, A., Pacheco, J.F., Singh, S.K., Manea, V.C. & Gurnis, M. 2008. Horizontal subduction and truncation of the Cocos plate beneath central Mexico. *Geophysical Research Letters* **35**, L18303.

Petford, N. & Gallagher, K. 2001. Partial melting of mafic (amphibolitic) lower crust by periodic influx of basaltic magma. *Earth and Planetary Science Letters* **193**, 483–499.

Polat, A., Frei, R., Fryer, B. & Appel, P.W.U. 2009. The origin of geochemical trends and Eoarchean (ca. 3700 Ma) zircons in Mesoarchean (ca. 3075 Ma) ocelli-hosting pillow basalts, Ivisaartoq greenstone belt, SW Greenland: evidence for crustal contamination versus crustal recycling. *Chemical Geology* **268**, 248–271.

Rajesh, H.M. 2007. The petrogenetic characterization of intermediate and silicic charnockites in high-grade terrains: a case study from southern India. *Contributions to Mineralogy and Petrology* **154**, 591–606.

Reagan, M.K. & Gill, J.B. 1989. Coexisting calcalkaline and high-niobium basalts from Turrialba volcano, Costa Rica: implications for residual titanites in arc magma sources. *Journal of Geophysical Research* **94**, 4619–4633.

Righter, K., Chelsey, J.T. & Ruiz, J. 2002. Genesis of primitive, arc-type basalt: constraints from Re, Os, and Cl on the depth of melting and role of fluids. *Geology* **30**, 619–622.

Roberts, S.J. & Ruiz, J. 1989. Geochemistry of exposed granulite facies terrains and lower crustal xenoliths in Mexico. *Journal of Geophysical Research* **94**, 7961–7974.

Robin, C. 1982. Mexico. *In*: Thorpe, R.S. (ed), *Andesites*. John Wiley, Chichester.

Rodríguez Lara, V.C. 1997. *Evolución del conjunto volcánico Guespalapa y del volcán Chichinautzin, Distrito Federal-Morelos, México*. BSc Thesis, ESIA-Instituto Politécnico Nacional, México, D.F. [unpublished].

Rollinson, H.R. 1993. *Using Geochemical Data: Evaluation, Presentation, Interpretation.* Longman Scientific & Technical, Essex, England.

Rudnick, R.L. & Gao, S. 2003. Composition of the Continental Crust. *In:* Carlson, R.W., Holland, H.D. & Turekian, K.K. (eds), *Treatise of Geochemistry*. Elsevier, New York **3**, 1–64.

Rudnick, R.L., McDonough, W.F. & O'Connell, R.J. 1998. Thermal structure, thickness and composition of continental lithosphere. *Chemical Geology* **145**, 399–415.

Ruiz, J., Patchett, P.J. & Arculus, R.J. 1988a. Nd-Sr isotope composition of lower crustal xenoliths – evidence for the origin of mid-Tertiary felsic volcanics in Mexico. *Contributions to Mineralogy and Petrology* **99**, 36–43.

Ruiz, J., Patchett, P.J. & Ortega-Gutierrez, F. 1988b. Proterozoic and Phanerozoic basement terranes of Mexico from Nd isotopic studies. *Geological Society of America Bulletin* **100**, 274–281.

Ryder, C.H., Gill, J.B., Tepley III, F., Ramos, F. & Reagan, M. 2006. Closed- to open-system differentiation at Arenal volcano (1968–2003). *Journal of Volcanology and Geothermal Research* **157**, 75–93.

Sánchez-Rubio, G. 1984. *Cenozoic Volcanism in the Toluca – Amealco Region, Central Mexico.* MSc Thesis, University of London, London – United Kingdom [unpublished].

Schaaf, P., Heinrich, W. & Besch, T. 1994. Composition and Sm-Nd isotopic data of the lower crust beneath San Luis Potosí, central Mexico: evidence from granulite-facies xenolith suite. *Chemical Geology* **118**, 63–84.

Schaaf, P., Stimac, J., Siebe, C. & Macías, J.L. 2005. Geochemical evidence for mantle origin and crustal processes in volcanic rocks from Popocatépetl and surrounding monogenetic volcanoes, Central Mexico. *Journal of Petrology* **46**, 1243–1282.

Schellart, W.P. 2005. Influence of the subducting plate velocity on the geometry of the slab and migration of the subduction hinge. *Earth and Planetary Science Letters* **231**, 197–219.

Schellart, W.P. 2007. The potential influence of subduction zone polarity on overriding plate deformation, trench migration and slab dip angle. *Tectonophysics* **445**, 363–372.

Shervais, J.W. 1982. Ti-V plots and the petrogenesis of modern and ophiolitic lavas. *Earth and Planetary Science Letters* **59**, 101–118.

Sheth, H.C. 2007. 'Large Igneous Provinces (LIPs)': definition, recommended terminology, and a hierarchical classification. *Earth Science Reviews* **85**, 117–124.

Sheth, H.C. 2008. Do major oxide tectonic discrimination diagrams work? Evaluating new log-ratio and discriminant-analysis-based diagrams with Indian Ocean mafic volcanics and Asian ophiolites. *Terra Nova* **20**, 229–236.

Sheth, H., Torres-Alvarado, I.S. & Verma, S.P. 2000. Beyond subduction and plumes: A unified tectonic-petrogenetic model for the Mexican Volcanic Belt. *International Geology Review* **42**, 1116–1132.

Shurbet, D.H. & Cebull, S.E. 1984. Tectonic interpretation of the Trans-Mexican Volcanic Belt. *Tectonophysics* **101**, 159–165.

Siebe, C., Rodríguez-Lara, V., Schaaf, P. & Abrams, M. 2004. Geochemistry, Sr-Nd isotope composition, and tectonic setting of Holocene Pelado, Guespalapa and Chichinautzin scoria cones, south of Mexico City. *Journal of Volcanology and Geothermal Research* **130**, 197–226.

Slovenec, D., Lugović, B. & Vlahović, I. 2010. Geochemistry, petrology and tectonomagmatic significance of basaltic rocks from the ophiolite mélange at the NW external-internal Dinarides junction (Croatia). *Geologica Carpathica* **61**, 273–292.

Srivastava, R.K., Chandra, R. & Shastry, A. 2004. High-Ti type N-MORB parentage of basalts from the south Andaman ophiolite suite, India. *Proceedings of Indian Academy of Sciences (Earth and Planetary Sciences)* **113**, 605–618.

Stock, J.M. 1996. Plate tectonics. *Encyclopedia of Applied Physics* **14**, 273–294.

Straub, S.M. & Martin Del Pozzo, A.L. 2001. The significance of phenocryst diversity in tephra from recent eruptions at Popocatepetl volcano (central Mexico). *Contributions to Mineralogy and Petrology* **140**, 487–510.

Sun, S.-S. & McDonough, W.F. 1989. Chemical and isotopic systematics of oceanic basalts: implications for mantle composition and processes. *In*: Saunders, A.D. & Norry, M.J. (eds), *Magmatism in the Ocean Basins*. Geological Society Special Publication **42**, 313–345.

Suter, M., Quintero, O. & Johnson, C.A. 1992. Active faults and the state of stress in the central part of the Trans-Mexican Volcanic Belt, Mexico: 1. The Venta de Bravo fault. *Journal of Geophysical Research* **97**, 11983–11993.

Suter, M., Quintero, O., López, M., Aguirre, G. & Farrrar, E. 1995. The Acambay graben: active intra-arc extension in the Trans-Mexican volcanic belt, Mexico. *Tectonics* **14**, 1245–1262.

Swinamer, R.T. 1989. *The Geomorphology, Petrography, Geochemistry and Petrogenesis of the Volcanic Rocks in the Sierra de Chichinautzin, Mexico*. MSc Thesis, Queen's University, Kingston, Ontario-Canada [unpublished].

Tatsumi, Y. & Eggins, S. 1993. *Subduction Zone Magmatism*. Blackwell Science, Ann Arbor.

Taylor, S.R. & McLennan, S.M. 1985. *The Continental Crust: Its Composition and Evolution*. Blackwell Scientific, Oxford.

Taylor, R.N. & Nesbitt, R.W. 1998. Isotopic characteristics of subduction fluids in an intra-oceanic setting, Izu-Bonin Arc, Japan. *Earth and Planetary Science Letters* **164**, 79–98.

Thirwall, M.F., Graham, A.M., Arculus, R.J., Harmon, R.S. & Macpherson, C.G. 1997. Resolution of the effects of crustal assimilation, sediment subduction, and fluid transport in island arc magmas: Pb-Sr-Nd-O isotope geochemistry of Grenada, Lesser Antilles. *Geochimica and Cosmochimica Acta* **60**, 4785–4810.

Torres-Alvarado, I.S., Verma, S.P., Palacios-Berruete, H., Guevara, M. & González-Castillo, O.Y. 2003. DC_Base: a database system to manage Nernst distribution coefficients and its application to partial melting modeling. *Computers & Geosciences* **29**, 1191–1198.

UNAM & CENAPRED Seismology Group 1995. The Milpa Alta earthquake of January 21, 1995. *Geofísica Internacional* **34**, 355–362.

Valdés, C.M., Mooney, W., Singh, K., Meyer, S., Lomnitz, C., Luetgert, J., Hesley, C., Lewis, B. & Mena, M. 1986. Crustal structure of Oaxaca, México, from seismic refraction measurements. *Bulletin of Seismological Society of America* **76**, 547–563.

Vázquez-Sánchez, E. & Jaimes-Palomera, L.R. 1989. Geología de la Cuenca de México. *Geofísica Internacional* **28**, 133–189.

Velasco-Tapia, F. & Verma, S.P. 2001a. Estado actual de la investigación geoquímica en el campo monogenético de la Sierra de Chichinautzin: Análisis de información y perspectivas. *Revista Mexicana de Ciencias Geológicas* **18**, 1–36.

Velasco-Tapia, F. & Verma, S.P. 2001b. First partial melting inversion model for a rift-related origin of the Sierra de Chichinautzin Volcanic Field, Central Mexican Volcanic Belt. *International Geology Review* **43**, 788–817.

Verma, S.P. 1992. Seawater alteration effects on REE, K, Rb, Cs, Sr, U, Th, Pb and Sr-Nd-Pb isotopic systematics in Mid-Ocean Ridge Basalt. *Geochemical Journal* **26**, 159–177.

Verma, S.P. 1999. Geochemistry of evolved magmas and their relationship to subduction un-related mafic volcanism at the volcanic front of the Central Mexican Volcanic Belt. *Journal of Volcanology and Geothermal Research* **93**, 151–171.

Verma, S.P. 2000. Geochemistry of subducting Cocos plate and the origin of subduction-unrelated mafic volcanism at the volcanic front of the Central Mexican Volcanic Belt (Mexico). *In*: Delgado-Granados, G., Aguirre-Díaz, G. & Stock, J.M. (eds), *Cenozoic Tectonics and Volcanism of Mexico.* Geological Society of America Special Paper **334**, 195–222.

Verma, S.P. 2002. Absence of Cocos plate subduction-related mafic volcanism in southern Mexico: a unique case on Earth? *Geology* **30**, 1095–1098.

Verma, S.P. 2004. Solely extension-related origin of the eastern to west-central Mexican Volcanic Belt (Mexico) from partial melting inversion model. *Current Science* **86**, 713–719.

Verma, S.P. 2006. Extension-related origin of magmas from a garnet-bearing source in the Los Tuxtlas volcanic field, Mexico. *International Journal of Earth Sciences* **95**, 871–901.

Verma, S.P. 2009. Continental rift setting for the central part of the Mexican Volcanic Belt: A statistical approach. *Open Geology Journal* **3**, 8–29.

Verma, S.P. 2010. Statistical evaluation of bivariate, ternary and discriminant function tectonomagmatic discrimination diagrams. *Turkish Journal of Earth Sciences* **19**, 239–265.

Verma, S.P. & Agrawal, S. 2011. New tectonic discrimination diagrams for basic and ultrabasic volcanic rocks through log-transformed ratios of high field strength elements and implications for petrogenetic processes. *Revista Mexicana de Ciencias Geológicas* **28**, 24–44.

Verma, S.P. & Díaz-González, L. 2012. Application of the discordant outlier detection and separation system in the geosciences. *International Geology Review*, **DOI:**10.1080/00206814.2011.569402.

Verma, S.P., Guevara, M. & Agrawal, S. 2006. Discriminating four tectonic settings: five new geochemical diagrams for basic and ultrabasic volcanic rocks based on log-ratio transformation of major-element data. *Journal of Earth System Science* **115**, 485–528.

Verma, S.P., Torres-Alvarado, I.S. & Sotelo-Rodríguez, Z.T. 2002. SINCLAS: standard igneous norm and volcanic rock classification system. *Computer* & *Geosciences* **28**, 711–715.

Verma, S.P., Verma, S.K., Pandarinath, K. & Rivera-Gómez, M.A. 2011. Evaluation of recent tectonomagmatic discrimination diagrams and their application to the origin of basic magmas in Southern Mexico and Central America. *Pure and Applied Geophysics*, **168**, 1501–1525.

Walker, J.A., Carr, M.J., Feigenson, M.D. & Kalamarides, R.I. 1990. The petrogenetic significance of interstratified high- and low-Ti basalts in central Nicaragua. *Journal of Petrology* **31**, 1141–1164.

Walker, J.A., Patino, L.C., Carr, M.J. & Feigenson, M.D. 2001. Slab control over HFSE depletions in central Nicaragua. *Earth and Planetary Science Letters* **192**, 533–543.

Wallace, P. & Carmichael, I.S.E. 1999. Quaternary volcanism near the Valley of Mexico: implications for subduction zone magmatism and the effects of crustal thickness variations on primitive magma compositions. *Contributions to Mineralogy and Petrology* **135**, 291–314.

White, W.M. & Dupré, B. 1986. Sediment subduction and magma genesis in the Lesser Antilles: isotopic and trace element constraints. *Journal of Geophysical Research* **91**, 5927–5941.

Xu, J.F., Shinjo, R., Defant, M.J., Wang, Q. & Rapp, R.P. 2002. Origin of Mesozoic adakitic intrusive rocks in the Ningzhen area of east China: partial melting of delaminated lower continental crust? *Geology* **30**, 1111–1114.

Yavuz, F. 1999. A revised program for microprobe-derived amphibole analyses using IMA rules. *Computers* & *Geosciences* **25**, 909–927.

Yavuz, F. 2001. PYROX: A computer program for the IMA pyroxene classification and calculation scheme. *Computer* & *Geosciences* **27**, 97–107.

Yogodzinski, G.M., Volynets, O.N., Koloskov, A.V., Seliverstov, N.I. & Matvenkov, V.V. 1994. Magnesian andesites and the subduction component in a strongly calc-alkaline series at Piip volcano, far western Aleutians. *Journal of Petrology* **35**, 163–204.

Zhang, Z., Zhao, G., Santosh, M., Wang, J., Dong, X. & Shen, K. 2010. Late Cretaceous charnockite with adakitic affinities form the Gangdese batholith, southeastern Tibet: Evidence for Neo-Tethyan mid-ocean ridge subduction? *Gondwana Research* **17**, 615–631.

Zindler, A. & Hart, S. 1986. Chemical geodynamics. *Annual Review of Earth and Planetary Science* **14**, 493–571.

APPENDIX

Appendix A1. New major-element data for SCN volcanic rocks.

Sample	CHI20	CHI56	CHI18	CHI59	CHI64	CHI70	CHI69	CHI19	CHI42	CHI16
Sample	S Barbara	Cima	Atlapulco	Jumiltepec	Tetillas	Pelagatos	Agua	Pehualtepec	Jumento	Santa Fe
Locality	18°58.88'	19°07.33'	19°14.98'	18°44.50'	18° 52.50'	19° 06.00'	19° 00.50'	19° 13.07'	19°10.16'	19° 10.21'
Latitude (°N):	98°55.42'	99°11.50'	99°23.75'	99°11.83'	99° 07.00'	98° 55.99'	98° 58.50'	99° 24.17'	99°19.09'	99° 27.20'
Longitude (ªW):	1	1	1	1	1	1	1	2	1	1
Analytical method	BA	BA	BTA, sho	BA	BA	BA	BA	BA	BA	BA
Rock type	M	M	HB1	HMI	HMI	HMI	E1	E1	DISQ	E1
Major elements (% m/m; original composition)										
SiO_2	51.650	52.110	52.320	52.960	52.630	53.100	54.010	55.640	55.250	55.240
TiO_2	1.534	1.459	1.059	1.479	0.920	0.770	1.330	1.160	0.980	1.300
Al_2O_3	15.730	16.580	15.310	17.690	16.000	15.490	16.710	16.250	16.160	16.070
$Fe_2O_3^t$	8.810	9.000	7.800	8.960	7.990	7.580	7.680	7.100	6.970	7.910
MnO	0.134	0.134	0.129	0.128	0.120	0.120	0.120	0.130	0.110	0.120
MgO	8.760	7.850	8.300	6.420	8.510	9.500	5.980	7.390	7.040	6.250
CaO	8.090	7.650	8.770	7.460	7.900	7.700	7.120	7.600	7.320	7.330
Na_2O	3.620	3.910	3.530	3.580	3.500	3.270	3.700	3.910	4.040	3.880
K_2O	1.230	1.080	2.180	0.790	0.980	1.000	1.240	1.170	1.540	1.270
P_2O_5	0.430	0.280	0.710	0.390	0.190	0.740	0.390	0.250	0.370	0.360
LOI	0.190	0.030	0.140	1.110	0.160	0.150	0.570	0.290	0.470	0.180
Major elements (% m/m; adjusted composition)										
$(SiO_2)_{adj}$	52.018	52.455	52.576	53.414	53.644	53.815	55.296	55.618	55.679	55.738
$(Na_2O)_{adj}$	3.646	3.936	3.547	3.611	3.567	3.314	3.788	3.908	4.071	3.915
$(K_2O)_{adj}$	1.239	1.087	2.191	0.797	0.999	1.013	1.270	1.170	1.552	1.281

Analytical Method: (1) ICP-OES ('4LithoRes' methodology; ActLabs, Inc., Canada); (2) XRF (Guevara *et al.* 2005; Instituto de Geología, UNAM, Mexico). Rock-types are presented according to total alkalis versus silica diagram (Le Bas *et al.* 1986; Le Bas 2000) on an anhydrous 100% adjusted basis and Fe_2O_3/FeO ratio after Middlemost (1989) using the SINCLAS computer program (Verma *et al.* 2002). Group subdivision based in phenocryst assemblage and geochemical composition: (a) HMI– high-magnesian intermediate magmas; DISQ– evolved magmas with a ol + opx ± cpx ± plg assemblage; (b) E2– evolved magmas with a opx ± cpx + plg assemblage; and (c) E3– evolved magmas with textural evidences of mineralogical disequilibrium, such as coexisting olivine and quartz, phenocrysts of plagioclase and pyroxene with oscillatory or more complex zoning and twinning, the presence of biotite and hornblende phenocrysts, and quartz xenocrysts with pyroxene reaction rims.

Appendix A1. Continued.

Sample	CHI14	CHI24	CHI55	CHI58	CHI33	CHI63	CHI67	CHI22	CHI27	CHI31
Locality	Coatepec	Cocotitlán	Tlecuilco	Ajusco	Temixco	Pelado	Cajete	Cuatepetl	Texclacoyoqui	Tioca
Latitude (°N):	19°09.03'	19°14.18'	18°54.00'	19°13.67'	18°51.03'	19°07.00'	19°06.00'	19°05.15'	19°09.05'	19°12.52'
Longitude (ªW):	99°24.93'	98°52.55'	98°48.50'	99°13.00'	99°12.42'	99°16.50'	99°14.50'	98°51.62'	98°56.03'	99°05.67'
Analytical method	2	2	2	1	2	2	1	1	1	1
Rock type	BA	BTA, mug	BA	BA	BA	A	A	A	A	A
Group	E1	E1	HMI	DISQ	E1	DISQ	DISQ	E1	E1	E2
Major elements (% m/m; original composition)										
SiO_2	55.850	55.700	55.770	56.390	56.740	58.780	58.340	58.870	59.670	60.050
TiO_2	1.3100	1.280	1.030	0.976	1.180	1.270	0.810	0.934	1.120	0.836
Al_2O_3	15.770	16.800	14.870	16.470	16.220	16.180	16.130	16.180	15.830	15.830
$Fe_2O_3^t$	7.940	7.510	7.130	6.960	7.580	7.070	5.940	6.290	6.780	5.660
MnO	0.130	0.120	0.120	0.110	0.130	0.120	0.093	0.102	0.109	0.090
MgO	6.530	5.320	8.370	6.550	6.180	4.760	5.260	5.630	4.450	5.420
CaO	7.130	7.100	6.860	6.960	6.680	5.550	6.050	5.890	6.070	6.050
Na_2O	4.200	4.140	3.490	3.840	3.720	4.280	4.270	3.950	3.890	3.880
K_2O	1.460	1.580	1.270	1.140	1.480	1.680	1.600	1.500	1.810	1.430
P_2O_5	0.390	0.350	0.260	0.190	0.320	0.360	0.310	0.220	0.390	0.170
LOI	0.100	0.200	0.190	0.610	0.320	0.400	0.380	0.450	0.050	0.410
Major elements (% m/m; adjusted composition)										
$(SiO_2)_{adj}$	55.803	56.077	56.558	56.938	56.950	59.069	59.318	59.412	59.908	60.666
$(Na_2O)_{adj}$	4.196	4.168	3.539	3.877	3.734	4.301	4.342	3.986	3.906	3.920
$(K_2O)_{adj}$	1.459	1.591	1.288	1.151	1.485	1.688	1.627	1.514	1.817	1.445

Sample	CHI40	CHI71	CHI38	CHI30	CHI77	CHI79	CHI72	CHI47	CHI28	CHI21
Sample	Mateo	Xicomulco	Pocito	Cuahutenco	Teuhtli	Tabaquillo	Zompole	Tres Cruces	Tlacotenco	S. Matías
Locality	19°11.50'	19°12.14'	19°03.92'	19°12.02'	19°13.00'	19°12.50'	19°11.83'	19°12.50'	19°09.25'	19°04.50'
Latitude (°N):	99°19.67'	99°03.66'	99°19.67'	99°05.88'	99°02.50'	99°08.00'	99°06.00'	99°17.66'	98°58.67'	98°50.85'
Longitude (ªW):	1	1	1	2	1	1	1	1	1	1
Analytical method	A	A	A	A	A	D	D	D	D	D
Rock type	E2	E2	E2	E1	E2	DISQ	E2	E2	E2	DISQ
Major elements (% m/m; original composition)										
SiO_2	54.640	60.870	60.740	61.300	62.230	62.970	63.460	63.680	63.150	63.220
TiO_2	0.912	0.810	0.804	0.970	0.757	0.630	0.851	0.785	0.746	0.720
Al_2O_3	19.800	16.570	16.600	16.000	15.290	17.920	15.900	17.010	16.010	15.740
$Fe_2O_3^t$	5.430	5.670	5.350	5.930	5.565	4.740	5.460	4.970	4.820	4.690
MnO	0.092	0.090	0.088	0.100	0.099	0.090	0.091	0.081	0.082	0.079
MgO	2.230	4.650	4.270	3.250	4.820	1.880	3.130	2.450	3.120	3.330
CaO	2.660	5.870	5.660	5.090	5.240	5.260	4.840	4.720	4.710	4.700
Na_2O	3.470	3.940	4.200	4.040	3.760	4.250	4.300	4.680	4.380	3.950
K_2O	0.800	1.520	1.540	1.630	1.690	1.530	1.920	1.570	1.830	2.030
P_2O_5	0.220	0.210	0.210	0.330	0.190	0.230	0.280	0.190	0.220	0.170
LOI	8.950	0.160	0.710	0.980	0.310	0.870	0.070	0.030	0.060	1.070
Major elements (% m/m; adjusted composition)										
$(SiO_2)_{adj}$	60.819	61.012	61.320	62.431	62.721	63.509	63.568	63.827	63.973	64.324
$(Na_2O)_{adj}$	3.862	3.949	4.240	4.114	3.790	4.286	4.307	4.691	4.437	4.019
$(K_2O)_{adj}$	0.890	1.524	1.555	1.660	1.703	1.543	1.923	1.574	1.854	2.065

Appendix A1. Continued.

Sample	CHI29	CHI26	CHI49	CHI43	CHI39
Sample	Atocpan	Tezilo	Tabaquillo	Mesa Gloria	Huitzilac
Locality	19°12.22’	19°02.65’	19°06.34’	19°04.00’	19°01.50’
Latitude (°N):	99°02.22’	98°55.55’	99°17.50’	99°19.84’	99°17.08’
Longitude ([a]W):	2	2	1	1	1
Analytical method	D	D	D	D	D
Rock type	E2	E2	DISQ	DISQ	E2
Major elements (% m/m; original composition)					
SiO_2	64.47	64.70	64.66	65.97	66.06
TiO_2	0.74	0.74	0.64	0.60	0.572
Al_2O_3	16.45	16.14	15.86	16.23	15.92
$Fe_2O_3^t$	5.05	5.03	4.48	4.23	3.84
MnO	0.10	0.10	0.08	0.08	0.066
MgO	2.82	3.17	2.97	2.21	2.20
CaO	4.55	4.55	4.84	3.93	4.07
Na_2O	4.07	4.14	4.15	4.25	4.34
K_2O	2.09	1.80	1.89	2.23	2.12
P_2O_5	0.24	0.24	0.18	0.20	0.16
LOI	0.20	0.22	0.36	0.20	0.56
Major elements (% m/m; adjusted composition)					
$(SiO_2)_{adj}$	64.336	64.545	65.037	66.223	66.683
$(Na_2O)_{adj}$	4.062	4.130	4.174	4.266	4.381
$(K_2O)_{adj}$	2.086	1.796	1.901	2.238	2.140

Appendix A2. New trace-element data (in $mg.g^{-1}$) for volcanic rocks from the SCN.

Sample	CHI20	CHI56	CHI18	CHI59	CHI64	CHI70	CHI69	CHI42	CHI16	CHI58	CHI67	CHI22	CHI27
La	23.2	14.5	66.0	22.9	10.3	10.8	21.3	24.2	23.3	13.7	20.3	16.9	34.7
Ce	53.0	32.1	139.0	46.9	23.1	24.0	44.7	54.1	49.0	28.8	44.9	34.7	69.3
Pr	7.2	4.0	19.0	5.7	3.2	3.3	5.9	7.4	6.4	3.4	6.2	4.4	7.6
Nd	29.1	16.7	83.6	24.4	14.5	14.0	24.8	32.0	27.9	15.5	26.8	18.4	29.6
Sm	6.05	4.24	15.50	5.64	3.37	3.43	5.43	6.56	5.94	3.82	5.62	4.14	6.38
Eu	2.15	1.54	4.28	1.85	1.16	1.09	1.76	1.82	1.98	1.27	1.61	1.25	1.71
Gd	5.80	4.52	10.50	5.14	3.58	3.38	5.22	5.36	5.11	3.56	4.74	3.94	5.32
Tb	0.86	0.77	1.36	0.85	0.63	0.57	0.86	0.78	0.82	0.64	0.68	0.66	0.87
Dy	4.69	4.47	6.58	4.80	3.64	3.29	4.83	3.84	4.64	3.87	3.59	3.69	5.14
Ho	0.96	0.84	1.04	0.93	0.72	0.65	0.97	0.72	0.86	0.71	0.67	0.70	0.98
Er	2.76	2.50	2.89	2.48	2.08	1.90	2.67	1.90	2.41	2.08	1.75	2.04	2.66
Tm	0.39	0.38	0.40	0.36	0.30	0.27	0.39	0.26	0.34	0.30	0.24	0.31	0.40
Yb	2.36	2.32	2.44	2.39	1.90	1.76	2.44	1.66	2.03	1.91	1.50	1.87	2.65
Lu	0.36	0.36	0.33	0.37	0.28	0.25	0.34	0.25	0.32	0.28	0.21	0.29	0.39
Sc	22	22	23	21	23	23	20	18	19	19	-	17	16
V	160	157	163	150	152	156	144	130	134	117	101	116	113
Cr	307	267	283	192	410	488	192	248	206	269	190	235	157
Co	39	33	31	18	31	33	23	24	32	25	19	29	29
Ni	187	116	183	55	161	220	37	132	61	114	86	126	47
Cu	36	32	22	18	22	57	22	36	21	37	93	29	22
Zn	87	84	103	27	78	90	66	97	91	84	-	92	88
Ga	17	18	17	16	16	16	18	16	19	19	-	21	20
Rb	23	20	36	12	17	19	25	20	23	24	23	41	47
Sr	631	467	1511	517	350	371	470	682	646	414	608	442	450
Y	25	24	30	26	20	18	26	20	23	18	17	19	26
Zr	192	153	217	223	125	114	209	139	160	140	139	152	292
Nb	11.4	11.3	5.4	12.0	3.8	2.7	13.3	5.3	9.5	6.6	4.0	7.0	13.5
Cs	0.70	0.70	0.90	0.60	0.74	1.05	1.29	0.90	0.80	1.10	-	1.60	1.30
Ba	451	234	1424	463	247	247	429	571	455	314	515	405	615
Hf	4.40	3.80	5.60	4.60	3.41	3.16	5.22	3.81	4.20	3.60	4.02	3.90	6.10
Ta	0.79	0.71	0.29	0.89	0.31	0.25	0.98	0.41	0.69	0.34	0.40	0.44	0.93
Pb	-	-	15.0	-	7.4	11.6	11.3	14.8	-	6.0	-	6.0	7.0
Th	2.83	2.06	7.73	3.27	1.65	2.02	3.16	3.01	2.77	2.19	2.84	3.27	5.19
U	0.90	0.60	2.71	1.04	0.57	0.65	1.09	1.08	1.00	0.75	-	1.04	1.31

Rock-type and group classification as defined in Appendix A1. Trace-element analysis was carried out in ActLabs, Inc. (Ancaster, Canada) by ICP-MS applying the '4LithoRes' methodology (http://www.actlabs.com/geochemistry/america/lithogeochemistry.htm).

Appendix A2. Continued.

Sample	CHI31	CHI40	CHI71	CHI38	CHI77	CHI79	CHI72	CHI47	CHI28	CHI21	CHI49	CHI39
La	15.7	20.0	16.1	18.6	19.1	15.6	24.9	12.1	20.6	17.8	18.4	20.5
Ce	32.6	47.9	33.5	37.3	38.4	31.8	47.2	25.2	40.6	34.1	37.6	39.6
Pr	4.0	7.3	4.3	5.0	4.6	4.0	5.7	3.4	5.0	3.9	4.7	4.6
Nd	16.6	29.7	17.7	22.5	18.6	16.2	23.9	14.9	19.7	16.4	19.1	18.5
Sm	3.6	6.12	3.87	4.71	3.90	3.24	4.77	3.48	3.94	3.73	3.92	3.65
Eu	1.19	1.77	1.17	1.47	1.22	1.11	1.36	1.08	1.19	1.10	1.13	1.02
Gd	3.40	6.21	3.56	3.93	3.70	2.99	4.40	3.31	3.71	3.19	3.61	3.23
Tb	0.60	0.92	0.60	0.64	0.70	0.50	0.75	0.55	0.60	0.54	0.55	0.50
Dy	3.20	5.18	3.22	3.66	3.60	2.75	4.14	3.07	3.47	3.10	2.97	2.53
Ho	0.60	1.02	0.65	0.66	0.70	0.54	0.77	0.62	0.64	0.58	0.59	0.48
Er	1.80	2.74	1.88	1.92	1.90	1.61	2.18	1.73	1.82	1.61	1.72	1.38
Tm	0.24	0.37	0.27	0.29	0.26	0.24	0.32	0.24	0.26	0.24	0.25	0.20
Yb	1.50	2.18	1.80	1.83	1.70	1.62	1.98	1.52	1.64	1.53	1.58	1.40
Lu	0.24	0.32	0.25	0.26	0.26	0.24	0.29	0.24	0.26	0.22	0.23	0.19
Sc	15	10	-	14	15	6	12	10	11	11	12	8
V	107	43	123	77	106	66	89	79	81	83	93	51
Cr	205	28	172	119	337	-	160	56	92	120	87	74
Co	27	10	15	16	20	6.3	14	10	19	25	10	9.0
Ni	50	-	-	69	52	-	45	-	56	59	-	20
Cu	14	94	14	20	26	-	23	13	18	19	-	15
Zn	64	158	-	86	78.	88	94	64	83	83	72	70
Ga	19	22	-	20	20	18	21	18	21	20	18	22
Rb	38	3	-	20	42	34	54	26	49	50	37	57
Sr	481	306	562	677	382	623	413	484	425	408	555	439
Y	18	29	18	17	20	15	20	17	17	15	16	12
Zr	150	170	135	135	173	140	201	135	174	151	152	151
Nb	5.0	5.4	5.0	4.9	6.0	4.9	10.1	3.5	8.1	7.0	4.8	6.7
Cs	1.80	-	-	1.10	1.90	1.95	2.10	0.85	1.80	2.10	1.76	2.30
Ba	394	449	404	467	467	396	559	389	548	484	531	602
Hf	3.70	4.40	3.79	3.90	4.30	3.91	5.30	3.77	4.70	-	4.29	4.40
Ta	0.40	0.34	0.42	0.33	0.50	0.44	0.61	0.32	0.49	0.47	0.49	-
Pb	-	14.0	-	7.0	6.0	13.7	9.0	9.1	8.0	7.0	13.3	9.0
Th	3.90	3.21	3.64	3.00	4.50	3.43	4.60	2.24	-	3.82	3.65	4.84
U	1.30	1.32	-	0.98	1.60	1.29	1.59	0.92	1.34	1.33	1.43	1.61

Appendix A3. New Sr and Nd isotopic data for volcanic rocks from the SCN.

Sample	Locality	Rock type	Group	$(SiO_2)_{adj}$ (%m/m)	$^{87}Sr/^{86}Sr$	$^{143}Nd/^{144}Nd$
CHI64	Tetillas	BA	HMI	53.644	0.704164±41	0.512854±19
CHI70	Pelagatos	BA	HMI	53.815	0.704164±32	0.512813±22
CHI69	Agua	BA	E1	55.296	0.704334±39	0.512766±18
CHI42	Jumento	BA	DISQ	55.679	0.704103±38	0.512971±20
CHI27	Texclacoyoqui	A	E1	59.908	0.704759±39	0.512697±16
CHI31	Tioca	A	E2	60.666	0.703987±41	0.512751±18
CHI71	Xicomulco	A	E2	61.012	0.704065±36	0.512787±17
CHI77	Teuhtli	A	E2	62.721	0.704254±37	0.512815±23
CHI79	Tabaquillo	D	DISQ	63.509	0.704157±34	0.512756±21
CHI28	Tlacotenco	D	E2	63.973	0.704470±43	0.512809±15
CHI21	S. Matías	D	DISQ	64.324	0.704525±44	0.512825±16
CHI49	Tabaquillo	D	DISQ	65.037	0.703791±38	0.512846±13

Rock-types and group classification as defined in Appendix A1. Sr and Nd isotopic data from Laboratorio Universitario de Geoquímica Isotópica (LUGIS-UNAM; México, D.F.) using a FINNIGAN MAT-262 mass spectrometer (average $^{87}Sr/^{86}Sr$= 0.710233±17 for n= 208 in SRM987 standard; average $^{143}Nd/^{144}Nd$= 0.511880±21 for n= 105 in La Jolla standard). Sr isotopic ratios normalised to $^{86}Sr/^{88}Sr$= 0.11940 and adjusted to $^{87}Sr/^{86}Sr$= 0.710230 for SRM987 standard. Nd isotopic ratios normalised to $^{146}Nd/^{144}Nd$= 0.72190 and adjusted to $^{143}Nd/^{144}Nd$= 0.511860 for La Jolla standard.

Appendix A4. Representative compositional data and structural formula for olivine phenocrysts (cores) in volcanic rocks from the SCN.

Sample	CH164 (*HMI*: $(SiO_2)_{adj}$= 53.64 %, $(MgO)_{adj}$= 8.67 %)						CHI33 (*E1*: $(SiO_2)_{adj}$= 56.95 %, $(MgO)_{adj}$= 6.20 %)					
%												
SiO_2	40.839	40.255	40.299	40.725	40.537	40.303	39.901	40.005	40.537	39.395	39.615	39.651
TiO_2	0.031	0.000	0.000	0.000	0.008	0.000	0.021	0.014	0.000	0.056	0.057	0.000
Al_2O_3	0.016	0.022	0.031	0.067	0.034	0.031	0.039	0.045	0.032	0.045	0.015	0.025
FeO^t	10.542	10.741	11.609	10.607	11.719	11.002	13.771	13.236	13.060	14.254	13.336	14.001
MnO	0.149	0.195	0.129	0.163	0.134	0.148	0.216	0.188	0.214	0.227	0.210	0.149
MgO	48.316	48.725	48.722	48.743	48.579	48.033	47.033	47.276	46.992	46.272	46.458	46.547
CaO	0.117	0.105	0.129	0.139	0.138	0.154	0.136	0.134	0.112	0.134	0.149	0.135
NiO	0.000	0.000	0.001	0.007	0.013	0.000	0.014	0.016	0.026	0.000	0.000	0.046
Cr_2O_3	0.033	0.096	0.022	0.075	0.055	0.000	0.000	0.010	0.000	0.004	0.057	0.026
Total	100.043	100.139	100.942	100.526	101.217	99.671	101.131	100.924	100.973	100.387	99.897	100.580
Si	1.003	0.991	0.987	0.996	0.990	0.997	0.986	0.988	0.998	0.984	0.989	0.986
Al	0.000	0.001	0.001	0.002	0.001	0.001	0.001	0.001	0.001	0.001	0.001	0.001
Sum	1.003	0.992	0.988	0.998	0.991	0.998	0.987	0.989	0.999	0.985	0.990	0.987
Ti	0.001	0.000	0.000	0.000	0.000	0.000	0.000	0.000	0.000	0.001	0.001	0.000
Cr	0.001	0.002	0.000	0.001	0.001	0.000	0.000	0.000	0.000	0.000	0.001	0.001
Fe^{+2}	0.216	0.221	0.238	0.217	0.239	0.227	0.285	0.273	0.269	0.298	0.279	0.291
Mn	0.003	0.004	0.003	0.003	0.003	0.003	0.005	0.004	0.004	0.005	0.004	0.003
Mg	1.769	1.787	1.780	1.778	1.770	1.771	1.733	1.740	1.725	1.722	1.730	1.726
Ca	0.003	0.003	0.003	0.004	0.004	0.004	0.004	0.004	0.003	0.004	0.004	0.004
Ni	0.000	0.000	0.000	0.000	0.000	0.000	0.000	0.000	0.001	0.000	0.000	0.001
Sum	1.993	2.017	2.024	2.004	2.017	2.005	2.026	2.022	2.0021	2.030	2.019	2.026
%Fo	89.10	89.00	88.21	89.12	88.08	88.62	85.89	86.43	86.51	85.27	86.13	85.56
%Fa	10.90	11.00	11.79	10.88	11.92	11.38	14.11	13.57	13.49	14.73	13.87	14.44

Sample	CHI63 (*DISQ*: $(SiO_2)_{adj}$= 59.07 %, $(MgO)_{adj}$= 4.78 %)						CHI27 (*E1*: $(SiO_2)_{adj}$= 59.91 %,$(MgO)_{adj}$= 4.47 %)					
%												
SiO_2	39.694	39.532	38.801	39.029	38.954	39.105	39.145	38.887	39.322	39.004	38.887	38.924
TiO_2	0.000	0.000	0.000	0.019	0.000	0.012	0.028	0.000	0.000	0.010	0.023	0.010
Al_2O_3	0.038	0.043	0.018	0.012	0.015	0.021	0.000	0.038	0.041	0.003	0.012	0.000
FeO^t	16.733	16.783	18.046	17.081	18.001	18.126	17.055	19.147	17.954	17.125	17.384	17.156
MnO	0.236	0.263	0.276	0.265	0.275	0.268	0.220	0.263	0.280	0.291	0.263	0.313
MgO	42.533	43.270	42.348	42.744	42.308	42.458	44.433	41.877	43.776	43.896	43.958	43.884
CaO	0.119	0.107	0.105	0.201	0.184	0.163	0.136	0.154	0.159	0.134	0.187	0.110
NiO	0.000	0.000	0.015	0.032	0.014	0.008	0.022	0.020	0.023	0.021	0.016	0.017
Cr_2O_3	0.035	0.006	0.059	0.047	0.052	0.049	0.028	0.011	0.000	0.017	0.011	0.000
Sum	99.388	100.004	99.668	99.430	99.803	100.210	101.067	100.397	101.555	100.501	100.741	100.414
Si	1.010	1.001	0.993	0.997	0.995	0.995	0.983	0.993	0.987	0.986	0.982	0.985
Al	0.001	0.001	0.001	0.000	0.001	0.001	0.000	0.001	0.001	0.000	0.001	0.000
Sum	1.011	1.002	0.994	0.997	0.996	0.996	0.983	0.994	0.988	0.986	0.983	0.985
Ti	0.000	0.000	0.000	0.000	0.000	0.000	0.001	0.000	0.000	0.000	0.000	0.000
Cr	0.001	0.000	0.001	0.001	0.001	0.001	0.001	0.000	0.000	0.000	0.000	0.000
Fe^{+2}	0.356	0.355	0.386	0.365	0.385	0.386	0.358	0.409	0.377	0.362	0.367	0.363
Mn	0.005	0.006	0.006	0.006	0.006	0.006	0.005	0.006	0.006	0.006	0.006	0.007
Mg	1.613	1.633	1.616	1.627	1.611	1.611	1.664	1.594	1.638	1.654	1.655	1.656
Ca	0.003	0.003	0.003	0.005	0.005	0.004	0.004	0.004	0.004	0.004	0.005	0.003
Ni	0.000	0.000	0.000	0.001	0.000	0.000	0.000	0.000	0.000	0.000	0.000	0.000
Sum	1.978	1.997	2.012	2.005	2.008	2.008	2.032	2.013	2.025	2.027	2.034	2.029
%												
Fo	81.92	82.13	80.71	81.69	80.73	80.68	82.28	79.59	81.30	82.05	81.85	82.02
Fa	18.08	17.87	19.29	18.31	19.27	19.32	17.72	20.41	18.70	17.95	18.15	17.98

Appendix A4. Continued.

Sample	CHI69 (*E1*: $(SiO_2)_{adj}$= 55.30%, $(MgO)_{adj}$= 6.12 %)			CHI42 (*DISQ*: $(SiO_2)_{adj}$= 55.68 %, $(MgO)_{adj}$= 7.10 %)			CHI11 (*DISQ*: $(SiO_2)_{adj}$= 61.10 %, $(MgO)_{adj}$= 4.40 %) *		CHI08 (*DISQ*: $(SiO_2)_{adj}$= 61.60 %, $(MgO)_{adj}$= 4.20 %) *		
%											
SiO_2	39.900	39.629	40.204	41.76	41.20	40.75	40.15	39.89	39.460	39.487	39.291
TiO_2	0.000	0.055	0.024	0.02	0.01	0.00	0.00	0.03	0.059	0.000	0.050
Al_2O_3	0.001	0.024	0.012	0.04	0.05	0.03	0.01	0.04	0.011	0.009	0.018
FeO^t	15.249	14.628	16.463	6.34	12.23	16.55	12.13	12.49	16.243	15.383	18.022
MnO	0.203	0.187	0.282	0.12	0.16	0.26	0.12	0.18	0.246	0.254	0.286
MgO	43.779	45.138	43.480	51.76	47.89	44.71	47.15	47.63	43.014	43.439	42.406
CaO	0.203	0.146	0.149	0.16	0.10	0.00	0.26	0.18	0.132	0.114	0.137
NiO	0.000	0.010	0.004	0.04	0.10	0.00	0.26	0.18	0.329	0.330	0.241
Cr_2O_3	0.011	0.024	0.055	0.02	0.00	0.04	0.01	0.04	0.000	0.009	0.036
Total	99.346	99.841	100.673	100.260	101.74	102.34	100.09	100.66	99.494	99.025	100.487
Si	1.009	0.995	1.008	1.004	1.002	1.004	0.995	0.986	1.003	1.005	0.997
Al	0.000	0.001	0.000	0.001	0.002	0.001	0.001	0.001	0.000	0.000	0.001
Sum	1.009	0.996	1.008	1.005	1.004	1.005	0.996	0.987	1.003	1.005	0.998
Ti	0.000	0.001	0.000	0.000	0.000	0.000	0.000	0.001	0.001	0.000	0.000
Cr	0.000	0.000	0.001	0.000	0.000	0.001	0.000	0.001	0.000	0.000	0.000
Fe^{+2}	0.322	0.307	0.345	0.127	0.249	0.341	0.251	0.258	0.345	0.327	0.820
Mn	0.004	0.004	0.006	0.002	0.003	0.005	0.003	0.004	0.005	0.005	0.006
Mg	1.650	1.690	1.625	1.855	1.737	1.643	1.743	1.754	1.630	1.648	1.605
Ca	0.005	0.004	0.004	0.004	0.003	0.000	0.007	0.005	0.004	0.003	0.004
Ni	0.000	0.000	0.000	0.001	0.002	0.000	0.005	0.004	0.007	0.007	0.005
Total	1.982	2.007	1.982	1.990	1.993	1.990	2.009	2.026	1.992	1.990	2.003
%											
Fo	83.66	84.62	82.48	93.57	87.47	82.81	87.39	87.17	85.52	83.43	80.75
Fa	16.34	15.38	17.52	6.43	12.53	17.19	12.61	12.83	17.48	16.57	19.25

*Geochemical and Sr-Nd isotopic whole-rock composition reported by Verma (1999).

Appendix A5. Representative compositional data and structural formula for spinel in volcanic rocks from the SCN.

Sample	CHI64 (*HMI*: $(SiO_2)_{adj}$= 53.64%, $(MgO)_{adj}$= 8.67%)										CHI70 (*HMI*: $(SiO_2)_{adj}$= 53.82%, $(MgO)_{adj}$= 9.63%)	
%												
Fo	89.10	89.00	88.21	89.12	88.08	88.62	89.00	88.21	88.83	89.10	90.39	87.10
SiO_2	0.074	0.073	0.101	0.145	0.114	0.099	0.124	0.101	0.128	0.113	0.140	0.100
TiO_2	0.563	0.666	0.894	0.730	1.315	1.261	0.638	1.008	1.016	0.651	0.490	0.510
Al_2O_3	21.345	21.066	20.540	19.042	19.161	18.724	21.343	20.086	20.327	22.558	19.280	18.510
Cr_2O_3	40.813	41.032	36.682	39.757	35.897	37.487	40.758	37.472	36.903	39.223	43.790	40.020
FeO^t	20.695	20.372	28.147	27.585	27.253	30.933	20.262	27.859	26.998	23.697	18.120	25.770
MnO	0.268	0.216	0.312	0.198	0.285	0.313	0.270	0.317	0.312	0.210	0.180	0.320
MgO	13.841	14.297	10.471	9.812	11.994	8.179	14.050	11.359	11.972	12.458	14.230	10.680
CaO	0.018	0.008	0.080	0.135	0.008	0.095	0.008	0.041	0.059	0.020	0.030	0.040
Total	97.617	97.730	97.227	97.404	96.027	97.091	97.453	98.243	97.715	98.930	96.260	95.950
Si	0.018	0.018	0.026	0.038	0.029	0.026	0.031	0.026	0.032	0.028	0.036	0.026
Ti	0.106	0.125	0.173	0.142	0.255	0.250	0.120	0.192	0.194	0.121	0.094	0.100
Al	6.282	6.182	6.215	5.818	5.828	5.808	6.281	5.999	6.066	6.592	5.777	5.708
Cr	8.058	8.078	7.446	8.149	7.325	7.801	8.047	7.508	7.388	7.689	8.802	8.279
Fe^{+3}	1.412	1.454	1.942	1.673	2.277	1.839	1.370	2.057	2.094	1.419	1.163	1.760
Fe^{+2}	2.910	2.788	4.101	4.307	3.605	4.970	2.861	3.847	3.623	3.494	2.689	3.878
Mn	0.057	0.046	0.068	0.043	0.062	0.070	0.057	0.068	0.067	0.044	0.039	0.071
Mg	5.153	5.308	4.008	3.792	4.615	3.210	5.231	4.292	4.520	4.606	5.393	4.166
Ca	0.005	0.002	0.022	0.037	0.002	0.027	0.002	0.011	0.016	0.005	0.008	0.011
Sum	24.001	24.001	24.001	23.999	23.998	24.001	24.000	24.000	24.000	23.998	24.001	23.999
Fe/(Fe + Mg)	0.46	0.44	0.60	0.61	0.56	0.68	0.45	0.58	0.56	0.52	0.42	0.58
Cr/(Cr + Al)	0.56	0.57	0.55	0.58	0.56	0.57	0.56	0.56	0.55	0.54	0.60	0.59
Fe^{+3}/ Fe	0.33	0.34	0.32	0.28	0.39	0.27	0.32	0.35	0.37	0.29	0.30	0.31

Sample	CHI63 (*DISQ*: $(SiO_2)_{adj}$= 59.07%, $(MgO)_{adj}$= 4.78%)		CHI33 (*E1*: $(SiO_2)_{adj}$= 56.95%, MgO= 6.20%)			CHI69 (*E1*: $(SiO_2)_{adj}$= 55.30%, MgO= 6.12%)		
%								
Fo	81.92	82.13	85.89	85.27	86.13	83.66	84.62	82.48
SiO_2	0.056	0.082	0.063	0.694	0.094	0.061	0.040	0.080
TiO_2	5.194	3.352	1.185	1.552	1.455	3.137	1.492	3.152
Al_2O_3	10.007	12.303	19.551	19.740	17.844	15.340	17.289	16.229
Cr_2O_3	35.305	34.192	39.222	37.423	39.903	32.822	40.009	32.941
FeO^t	38.590	37.903	24.676	25.801	26.718	34.915	27.419	34.419
MnO	0.342	0.181	0.281	0.292	0.201	0.316	0.271	0.212
MgO	7.068	9.138	12.155	11.857	11.367	8.392	11.173	9.957
CaO	0.040	0.000	0.033	0.009	0.000	0.054	0.009	0.000
Total	96.602	97.151	97.166	97.368	97.582	95.037	97.702	96.990
Si	0.015	0.022	0.016	0.177	0.024	0.017	0.010	0.021
Ti	1.080	0.675	0.227	0.297	0.282	0.640	0.290	0.622
Al	3.261	3.884	5.881	5.926	5.414	4.904	5.259	5.021
Cr	7.717	7.240	7.914	7.536	8.122	7.039	8.163	6.837
Fe^{+3}	2.831	3.482	1.718	1.590	1.852	2.745	1.978	2.856
Fe^{+2}	6.090	5.007	3.549	3.906	3.899	5.175	3.939	4.699
Mn	0.080	0.041	0.061	0.063	0.044	0.073	0.059	0.047
Mg	2.913	3.649	7.625	4.503	4.363	3.394	4.299	3.897
Ca	0.012	0.000	0.009	0.002	0.000	0.016	0.002	0.000
Total	23.999	24.000	27.000	24.000	24.000	24.003	23.999	24.000
Fe/(Fe + Mg)	0.75	0.70	0.53	0.55	0.57	0.70	0.58	0.66
Cr/(Cr + Al)	0.70	0.65	0.57	0.56	0.60	0.59	0.61	0.58
Fe^{+3}/ Fe	0.32	0.41	0.33	0.29	0.32	0.35	0.33	0.38

Appendix A6. Representative compositional data and structural formula for orthopyroxene in volcanic rocks from the SCN.

Sample	CHI63 (*DISQ*: $(SiO_2)_{adj}$= 59.07%,; $(MgO)_{adj}$= 4.78%)									
Analysis	Core	Rim	Core	Rim	Core	Rim	Core	Rim	Core	Rim
%										
SiO_2	55.284	55.022	55.546	54.447	55.418	54.785	55.010	54.685	56.039	54.500
TiO_2	0.141	0.231	0.182	0.300	0.034	0.225	0.190	0.284	0.109	0.121
Al_2O_3	2.234	1.527	1.282	1.833	1.094	1.598	2.369	1.570	1.477	2.430
FeO^t	9.289	10.151	10.653	12.199	12.947	10.637	10.439	10.828	9.911	10.505
MnO	0.170	0.276	0.241	0.257	0.196	0.180	0.175	0.229	0.194	0.219
MgO	31.430	30.371	30.192	28.013	28.821	29.890	29.494	29.970	30.943	29.453
CaO	1.085	1.219	1.276	1.742	0.504	1.150	1.550	1.244	1.131	1.190
Na_2O	0.037	0.032	0.040	0.051	0.013	0.061	0.069	0.000	0.031	0.073
NiO	0.020	0.009	0.018	0.000	0.080	0.000	0.000	0.038	0.000	0.000
Cr_2O_3	0.518	0.363	0.331	0.329	0.075	0.397	0.439	0.396	0.244	0.531
Total	100.208	99.201	99.761	99.171	99.182	98.923	99.735	99.244	100.079	99.022
Si	1.936	1.955	1.965	1.955	1.985	1.955	1.946	1.949	1.967	1.943
Al IV	0.064	0.045	0.035	0.045	0.015	0.045	0.054	0.051	0.033	0.057
Sum	2.000	2.000	2.000	2.000	2.000	2.000	2.000	2.000	2.000	2.000
Al VI	0.028	0.019	0.019	0.033	0.031	0.023	0.045	0.015	0.028	0.045
Ti	0.004	0.006	0.005	0.008	0.001	0.006	0.005	0.008	0.003	0.003
Cr	0.014	0.010	0.009	0.009	0.002	0.011	0.012	0.011	0.007	0.015
Fe^{+3}	0.024	0.009	0.000	0.000	0.000	0.004	0.000	0.014	0.000	0.000
Mg	1.641	1.609	1.593	1.500	1.539	1.590	1.556	1.593	1.619	1.565
Fe^{+2}	0.248	0.293	0.315	0.366	0.388	0.313	0.309	0.309	0.291	0.313
Mn	0.005	0.008	0.007	0.008	0.006	0.005	0.005	0.007	0.006	0.007
Ni	0.001	0.000	0.001	0.000	0.002	0.000	0.000	0.001	0.000	0.000
Ca	0.041	0.046	0.048	0.067	0.019	0.044	0.059	0.048	0.043	0.045
Na	0.003	0.002	0.003	0.004	0.001	0.004	0.005	0.000	0.002	0.005
Sum	2.008	2.003	2.000	1.995	1.990	2.001	1.996	2.005	1.998	1.998
% En	83.78	81.87	81.12	77.27	78.84	81.26	80.67	80.85	82.68	81.08
% Fs	14.14	15.77	16.42	19.28	20.17	16.50	16.29	16.74	15.15	16.56
% Wo	2.08	2.36	2.46	3.45	0.99	2.25	3.05	2.41	2.17	2.35

Sample	CHI27 (*E1*: $(SiO_2)_{adj}$ = 59.91%, $(MgO)_{adj}$ = 4.47%)									
Analysis	Core	Rim	Core	Rim	Core	Rim	Core	Rim	Core	Rim
%										
SiO_2	54.262	53.947	55.175	55.293	54.445	54.447	54.844	55.086	54.987	54.921
TiO_2	0.225	0.305	0.181	0.202	0.156	0.308	0.183	0.165	0.183	0.224
Al_2O_3	1.925	2.207	1.625	1.457	1.943	1.620	1.328	0.718	1.738	1.326
FeO^t	10.512	10.482	10.691	10.214	10.554	11.030	10.225	12.065	11.439	10.346
MnO	0.223	0.198	0.251	0.209	0.257	0.215	0.234	0.310	0.186	0.242
MgO	30.528	30.239	30.795	30.143	30.667	30.508	31.240	29.726	29.599	30.423
CaO	1.333	1.411	1.470	1.441	1.301	1.421	1.226	1.776	1.615	1.354
Na_2O	0.058	0.042	0.018	0.019	0.079	0.036	0.059	0.059	0.022	0.031
NiO	0.000	0.000	0.000	0.086	0.016	0.036	0.026	0.000	0.016	0.000
Cr_2O_3	0.390	0.451	0.375	0.276	0.519	0.357	0.463	0.136	0.263	0.292
Total	99.456	99.282	100.581	99.340	99.937	99.978	99.828	100.041	100.048	99.159
Si	1.930	1.923	1.941	1.962	1.928	1.932	1.941	1.962	1.949	1.955
Al IV	0.070	0.077	0.059	0.038	0.072	0.068	0.059	0.038	0.051	0.045
Sum	2.000	2.000	2.000	2.000	2.000	2.000	2.000	2.000	2.000	2.000
Al VI	0.011	0.015	0.008	0.023	0.009	0.000	0.000	0.001	0.022	0.011
Ti	0.006	0.008	0.005	0.005	0.004	0.008	0.005	0.004	0.005	0.006
Cr	0.011	0.013	0.010	0.008	0.015	0.010	0.013	0.004	0.007	0.008
Fe^{+3}	0.061	0.054	0.049	0.000	0.067	0.067	0.067	0.056	0.020	0.025
Mg	1.619	1.607	1.615	1.595	1.619	1.614	1.648	1.578	1.564	1.614
Fe^{+2}	0.252	0.259	0.266	0.303	0.245	0.260	0.236	0.303	0.320	0.283
Mn	0.007	0.006	0.007	0.006	0.008	0.006	0.007	0.009	0.006	0.007
Ni	0.000	0.000	0.000	0.002	0.000	0.001	0.001	0.000	0.000	0.000
Ca	0.051	0.054	0.055	0.055	0.049	0.054	0.046	0.068	0.061	0.052
Na	0.004	0.003	0.001	0.001	0.005	0.002	0.004	0.004	0.002	0.002
Total	2.020	2.018	2.016	1.999	2.023	2.023	2.026	2.019	2.007	2.008
% En	81.39	81.19	81.06	81.41	81.41	80.63	82.23	78.34	79.39	81.48
% Fs	16.06	16.09	16.16	15.79	16.10	16.67	15.45	18.30	17.49	15.91
% Wo	2.55	2.72	2.78	2.80	2.48	2.70	2.32	3.36	3.11	2.61

Appendix A6. Continued.

Sample	CHI31 (*E2*: $(SiO_2)_{adj}$= 60.67%, MgO= 5.48%)				CHI71 (*E2*: $(SiO_2)_{adj}$= 61.01%, MgO= 4.66%)				CHI03 (*E2*: $(SiO_2)_{adj}$= 61.96%, MgO= 5.25%)*			
Analysis	Core	Rim	Core	Rim	Core	Rim	Core	Rim	Core	Rim	Core	Rim
%												
SiO_2	56.102	55.254	56.461	55.659	56.093	55.276	53.952	54.748	55.615	55.808	56.374	55.327
TiO_2	0.133	0.170	0.119	0.126	0.064	0.211	0.166	0.161	0.152	0.194	0.129	0.166
Al_2O_3	1.543	1.198	0.740	1.189	1.692	1.386	3.320	1.793	1.408	1.388	0.646	0.690
FeO^t	7.289	8.428	8.230	8.882	7.426	11.452	6.980	10.889	8.276	10.816	9.474	10.505
MnO	0.181	0.246	0.175	0.203	0.163	0.240	0.158	0.285	0.164	0.230	0.244	0.188
MgO	33.240	32.191	32.880	32.187	32.979	30.343	32.263	30.385	31.414	28.845	31.033	30.273
CaO	0.948	1.286	1.313	1.233	0.941	1.170	1.162	0.996	0.962	1.562	1.335	1.541
Na_2O	0.026	0.022	0.049	0.033	0.048	0.015	0.068	0.058	0.055	0.030	0.048	0.073
NiO	0.000	0.000	0.000	0.022	0.020	0.000	0.000	0.000	0.126	0.097	0.089	0.079
Cr_2O_3	0.346	0.250	0.237	0.337	0.412	0.078	0.646	0.282	0.451	0.057	0.201	0.051
Total	99.808	99.045	100.204	99.871	99.838	100.171	98.715	99.597	98.620	99.030	99.570	98.890
Si	1.953	1.952	1.967	1.953	1.953	1.954	1.902	1.944	1.968	1.988	1.987	1.975
Al IV	0.047	0.048	0.033	0.047	0.047	0.046	0.098	0.056	0.032	0.012	0.013	0.025
Sum	2.000	2.000	2.000	2.000	2.000	2.000	2.000	2.000	2.000	2.000	2.000	2.000
Al VI	0.016	0.002	0.000	0.003	0.022	0.012	0.040	0.019	0.027	0.046	0.013	0.004
Ti	0.003	0.005	0.003	0.003	0.002	0.006	0.004	0.004	0.004	0.005	0.003	0.004
Cr	0.010	0.007	0.007	0.009	0.011	0.002	0.018	0.008	0.013	0.002	0.006	0.001
Fe^{+3}	0.025	0.047	0.038	0.045	0.020	0.031	0.053	0.038	0.000	0.000	0.000	0.022
Mg	1.725	1.696	1.708	1.684	1.712	1.599	1.696	1.608	1.657	1.532	1.630	1.611
Fe^{+2}	0.187	0.202	0.202	0.215	0.196	0.307	0.153	0.285	0.245	0.322	0.279	0.292
Mn	0.005	0.007	0.005	0.006	0.005	0.007	0.005	0.009	0.005	0.007	0.007	0.006
Ni	0.000	0.000	0.000	0.001	0.001	0.000	0.000	0.000	0.004	0.003	0.003	0.002
Ca	0.035	0.049	0.049	0.046	0.035	0.044	0.044	0.038	0.036	0.060	0.050	0.059
Na	0.002	0.002	0.003	0.002	0.003	0.001	0.005	0.004	0.004	0.002	0.003	0.005
Total	2.008	2.016	2.015	2.015	2.007	2.011	2.018	2.013	1.994	1.978	1.995	2.007
%												
En	87.22	84.75	85.32	84.32	86.99	80.39	86.96	81.31	85.27	79.76	82.88	80.99
Fs	11.00	12.81	12.24	13.35	11.23	17.38	10.79	16.78	12.85	17.14	14.56	16.05
Wo	1.79	2.43	2.45	2.32	1.78	2.23	2.25	1.92	1.88	3.10	2.56	2.96

Sample	CHI77 (*E2*: $(SiO_2)_{adj}$ = 62.72 %, MgO = 4.86%)				CHI28 (*E2*: $(SiO_2)_{adj}$ = 63.97 %, MgO = 3.16%)				CHI02 (*E2*: $(SiO_2)_{adj}$ = 63.73 %, MgO = 3.31%)*			
Analysis	Core	Rim	Core	Rim	Core	Rim	Core	Rim	Core	Rim	Core	Rim
%												
SiO_2	55.666	54.461	55.226	54.729	54.528	55.625	54.454	55.148	53.80	55.66	55.89	55.23
TiO_2	0.107	0.244	0.110	0.197	0.191	0.223	0.224	0.215	0.27	0.21	0.23	0.21
Al_2O_3	2.053	1.572	2.389	1.420	1.989	1.809	1.953	1.530	1.63	1.62	1.07	1.35
FeO^t	8.291	13.195	7.127	12.025	9.536	9.383	9.214	10.399	10.94	11.66	11.64	11.54
MnO	0.195	0.342	0.095	0.209	0.206	0.237	0.200	0.231	0.27	0.22	0.31	0.32
MgO	32.256	27.967	32.958	29.703	31.706	31.655	31.704	31.098	29.90	29.36	30.13	30.14
CaO	0.831	1.605	1.088	1.388	1.216	1.358	1.340	1.078	1.42	1.16	1.29	1.26
Na_2O	0.043	0.012	0.050	0.028	0.002	0.006	0.021	0.009	0.03	0.05	0.02	0.02
NiO	0.009	0.017	0.000	0.000	0.009	0.038	0.006	0.030	0.05	0.00	0.02	0.00
Cr_2O_3	0.633	0.150	0.544	0.192	0.377	0.386	0.403	0.360	0.35	0.27	0.25	0.28
Total	100.084	99.565	99.587	99.891	99.760	100.720	99.519	100.098	98.66	100.21	100.85	100.35
Si	1.942	1.957	1.928	1.949	1.924	1.941	1.924	1.944	1.935	1.967	1.965	1.953
Al IV	0.058	0.043	0.072	0.051	0.076	0.059	0.076	0.056	0.065	0.033	0.035	0.047
Sum	2.000	2.000	2.000	2.000	2.000	2.000	2.000	2.000	2.000	2.000	2.000	2.000
Al VI	0.026	0.023	0.026	0.008	0.007	0.015	0.006	0.008	0.004	0.034	0.009	0.009
Ti	0.003	0.007	0.003	0.005	0.005	0.006	0.006	0.006	0.007	0.006	0.006	0.006
Cr	0.017	0.004	0.015	0.005	0.011	0.011	0.011	0.010	0.010	0.008	0.007	0.008
Fe^{+3}	0.018	0.005	0.043	0.044	0.072	0.033	0.072	0.041	0.058	0.000	0.011	0.031
Mg	1.678	1.498	1.715	1.577	1.668	1.647	1.670	1.634	1.603	1.546	1.579	1.589
Fe^{+2}	0.224	0.391	0.165	0.314	0.209	0.241	0.201	0.266	0.271	0.344	0.331	0.310
Mn	0.006	0.010	0.003	0.006	0.006	0.007	0.006	0.007	0.008	0.007	0.009	0.010
Ni	0.000	0.000	0.000	0.000	0.000	0.001	0.000	0.001	0.001	0.000	0.001	0.000
Ca	0.031	0.062	0.041	0.053	0.046	0.051	0.051	0.041	0.055	0.044	0.049	0.048
Na	0.003	0.001	0.003	0.002	0.000	0.000	0.001	0.001	0.002	0.003	0.001	0.001
Total	2.006	2.002	2.014	2.015	2.024	2.011	2.024	2.014	2.020	1.992	2.004	2.011
%												
En	85.75	76.17	87.21	79.07	83.34	83.24	83.54	82.19	80.35	79.66	79.79	79.95
Fs	12.66	20.69	10.72	18.27	14.37	14.19	13.92	15.76	16.90	18.08	17.76	17.65
% Wo	1.59	3.14	2.07	2.66	2.30	2.57	2.54	2.05	2.74	2.26	2.45	2.40

Appendix A6. Continued.

Sample	CHI11 (*DISQ*: $(SiO_2)_{adj}$ = 61.20%, $(MgO)_{adj}$ = 4.43%)*		CHI08 (*DISQ*: $(SiO_2)_{adj}$ = 61.63%, $(MgO)_{adj}$ = 4.17%)*						CHI21 (*DISQ*: $(SiO_2)_{adj}$ = 64.32%, $(MgO)_{adj}$ = 3.39%)			
Analysis	Rim-ol	Rim-ol	Core	Rim	Core	Rim	Core	Rim	Core	Core	Core	Core
%												
SiO_2	53.44	54.15	55.442	53.278	56.261	55.061	54.316	55.118	53.476	55.171	53.670	54.480
TiO_2	0.24	0.26	0.221	0.255	0.102	0.120	0.132	0.154	0.263	0.168	0.237	0.198
Al_2O_3	2.29	2.65	1.471	3.063	0.953	1.827	2.414	1.589	3.302	1.689	1.864	1.291
FeO^t	16.79	15.36	9.316	14.014	8.394	8.891	11.773	9.653	9.288	13.029	12.322	13.561
MnO	0.32	0.33	0.214	0.686	0.189	0.222	0.311	0.208	0.172	0.220	0.311	0.316
MgO	24.22	23.21	30.754	26.732	31.990	31.406	28.995	31.054	30.673	28.849	28.514	28.797
CaO	1.76	1.36	1.577	1.221	1.097	1.111	1.299	1.232	1.795	1.109	1.788	1.598
Na_2O	0.28	0.33	0.048	0.034	0.014	0.034	0.079	0.040	0.075	0.057	0.049	0.051
NiO	0.03	0.06	0.082	0.096	0.186	0.143	0.024	0.149	0.058	0.013	0.000	0.032
Cr_2O_3	0.03	0.04	0.332	0.079	0.258	0.471	0.188	0.317	0.514	0.361	0.187	0.108
Total	99.400	97.750	99.46	99.46	99.44	99.29	99.53	99.51	99.62	100.67	98.94	100.43
Si	1.956	1.994	1.959	1.926	1.976	1.945	1.938	1.949	1.893	1.955	1.937	1.946
Al IV	0.044	0.006	0.041	0.074	0.024	0.055	0.062	0.051	0.107	0.045	0.063	0.054
Sum	2.000	2.000	2.000	2.000	2.000	2.000	2.000	2.000	2.000	2.000	2.000	2.000
Al VI	0.055	0.109	0.020	0.056	0.015	0.021	0.040	0.015	0.031	0.025	0.016	0.000
Ti	0.007	0.007	0.006	0.007	0.003	0.003	0.004	0.004	0.007	0.004	0.006	0.005
Cr	0.001	0.001	0.009	0.002	0.007	0.013	0.005	0.009	0.014	0.010	0.005	0.003
Fe^{+3}	0.000	0.000	0.005	0.007	0.000	0.026	0.023	0.032	0.078	0.008	0.048	0.066
Mg	1.322	1.274	1.620	1.440	1.675	1.654	1.542	1.637	1.619	1.524	1.534	1.533
Fe^{+2}	0.514	0.473	0.270	0.416	0.246	0.237	0.329	0.254	0.197	0.378	0.324	0.339
Mn	0.010	0.010	0.006	0.021	0.006	0.007	0.009	0.006	0.005	0.007	0.010	0.010
Ni	0.001	0.002	0.002	0.003	0.005	0.004	0.001	0.004	0.002	0.000	0.000	0.001
Ca	0.069	0.054	0.060	0.047	0.041	0.042	0.050	0.047	0.068	0.042	0.069	0.061
Na	0.020	0.024	0.003	0.002	0.001	0.002	0.005	0.003	0.005	0.004	0.003	0.004
Sum	1.997	1.953	2.002	2.002	1.999	2.009	2.008	2.011	2.026	2.003	2.016	2.022
%												
En	69.03	70.35	82.60	74.55	85.09	84.16	78.99	82.87	82.30	77.80	77.30	76.32
Fs	27.36	26.68	14.36	23.01	12.81	13.70	18.47	14.76	14.24	20.05	19.22	20.63
Wo	3.60	2.96	3.04	2.45	2.10	2.14	2.54	2.36	3.46	2.15	3.48	3.04

Sample	CHI79 (*DISQ*: $(SiO_2)_{adj}$ = 63.51%, $(MgO)_{adj}$ = 1.90%)		CHI49 (*DISQ*: $(SiO_2)_{adj}$ = 65.04%, $(MgO)_{adj}$ = 2.99%)						CHI10 (*DISQ*: $(SiO_2)_{adj}$ = 63.47%, $(MgO)_{adj}$ = 3.34%)*			
Analysis	Rim-bt	Rim-bt	Core	Rim	Core	Rim	Core	Rim	Core	Core	Core	Core
%												
SiO_2	53.580	53.743	55.32	56.53	55.08	54.77	54.94	54.95	55.936	55.127	56.014	55.739
TiO_2	0.473	0.462	0.13	0.18	0.16	0.10	0.18	0.18	0.144	0.155	0.179	0.151
Al_2O_3	1.891	1.902	1.94	2.21	1.69	1.85	2.13	2.06	1.459	1.867	1.761	1.678
FeO^t	10.102	10.302	9.56	10.05	10.17	9.36	9.43	11.18	7.416	7.783	8.204	7.623
MnO	0.298	0.243	0.13	0.19	0.31	0.25	0.20	0.27	0.144	0.139	0.144	0.142
MgO	30.075	30.259	30.64	28.46	30.53	30.01	30.85	29.43	33.080	32.679	32.221	32.819
CaO	1.841	2.068	1.18	1.17	1.30	1.20	1.29	1.24	1.106	1.159	0.935	1.004
Na_2O	0.057	0.047	0.05	0.26	0.05	0.04	0.06	0.04	0.066	0.026	0.027	0.032
NiO	0.047	0.051	0.00	0.04	0.00	0.01	0.00	0.00	0.060	0.045	0.037	0.041
Cr_2O_3	0.015	0.000	0.41	0.21	0.37	0.40	0.39	0.33	0.424	0.560	0.403	0.430
Total	98.379	99.077	99.360	99.300	99.660	97.990	99.470	99.680	99.835	99.540	99.925	99.659
Si	1.927	1.922	1.954	1.995	1.949	1.961	1.941	1.951	1.950	1.933	1.954	1.947
Al IV	0.073	0.078	0.046	0.005	0.051	0.039	0.059	0.049	0.050	0.067	0.046	0.053
Sum	2.000	2.000	2.000	2.000	2.000	2.000	2.000	2.000	2.000	2.000	2.000	2.000
Al VI	0.007	0.002	0.035	0.087	0.020	0.039	0.029	0.037	0.010	0.010	0.027	0.016
Ti	0.013	0.012	0.003	0.005	0.004	0.003	0.005	0.005	0.004	0.004	0.005	0.004
Cr	0.000	0.000	0.011	0.006	0.010	0.011	0.011	0.009	0.012	0.016	0.011	0.012
Fe^{+3}	0.066	0.081	0.000	0.000	0.024	0.000	0.021	0.000	0.038	0.052	0.000	0.028
Mg	1.612	1.613	1.614	1.497	1.611	1.602	1.625	1.557	1.719	1.708	1.676	1.709
Fe^{+2}	0.238	0.227	0.282	0.297	0.277	0.280	0.258	0.332	0.179	0.177	0.239	0.195
Mn	0.009	0.007	0.004	0.006	0.009	0.008	0.006	0.008	0.004	0.004	0.004	0.004
Ni	0.001	0.001	0.000	0.001	0.000	0.000	0.000	0.000	0.002	0.001	0.001	0.001
Ca	0.071	0.079	0.045	0.044	0.049	0.046	0.049	0.047	0.041	0.044	0.035	0.038
Na	0.004	0.003	0.003	0.018	0.003	0.003	0.004	0.003	0.004	0.002	0.002	0.002
Total	2.022	2.027	1.998	1.960	2.008	1.993	2.007	1.998	2.013	2.017	2.000	2.009
%												
En	80.77	80.34	82.98	81.21	81.75	82.75	82.98	80.09	86.79	86.10	85.75	86.60
Fs	15.67	15.71	14.72	16.39	15.75	14.87	14.53	17.48	11.13	11.71	12.46	11.50
Wo	3.55	3.95	2.30	2.40	2.50	2.38	2.49	2.43	2.09	2.19	1.79	1.90

* Geochemical and Sr-Nd isotopic whole-rock composition reported by Verma (1999).

Appendix A7. Representative compositional data and structural formula for clinopyroxene in volcanic rocks from the SCN.

Sample	CHI31 (*E2*: $(SiO_2)_{adj}$= 60.67%, $(MgO)_{adj}$= 5.48%)						CHI71 (*E2*: $(SiO_2)_{adj}$= 61.01%, $(MgO)_{adj}$= 4.66%)					
Analysis	Core	Rim	Core	Rim	Core	Rim	Core	Inter	Rim	Core	Inter	Rim
%												
SiO_2	53.022	51.857	53.078	51.958	52.075	51.170	51.769	52.911	52.528	53.261	52.134	52.445
TiO_2	0.397	0.463	0.370	0.443	0.450	0.737	0.736	0.453	0.394	0.354	0.395	0.403
Al_2O_3	1.706	2.496	1.622	2.393	1.727	3.257	3.320	2.113	2.018	1.311	1.964	1.985
FeO^t	5.099	5.247	4.466	4.677	5.170	6.443	5.941	5.629	5.634	4.740	5.295	5.393
MnO	0.187	0.089	0.118	0.161	0.112	0.129	0.181	0.101	0.112	0.187	0.176	0.136
MgO	17.663	17.515	17.645	17.295	17.342	16.947	16.148	16.901	17.071	18.502	17.139	16.900
CaO	21.533	21.337	22.117	21.639	21.979	20.313	21.655	22.207	22.063	21.085	22.215	21.962
Na_2O	0.252	0.291	0.263	0.247	0.231	0.296	0.329	0.304	0.308	0.208	0.240	0.228
NiO	0.073	0.000	0.020	0.000	0.006	0.006	0.000	0.000	0.004	0.118	0.015	0.041
Cr_2O_3	0.415	0.482	0.214	0.411	0.051	0.138	0.221	0.133	0.109	0.220	0.139	0.200
Sum	100.347	99.777	99.913	99.224	99.143	99.436	100.300	100.752	100.241	99.986	99.712	99.693
Si	1.937	1.908	1.943	1.918	1.929	1.893	1.900	1.930	1.927	1.946	1.923	1.932
Al IV	0.063	0.092	0.057	0.082	0.071	0.107	0.100	0.070	0.073	0.054	0.077	0.068
Sum	2.000	2.000	2.000	2.000	2.000	2.000	2.000	2.000	2.000	2.000	2.000	2.000
Al VI	0.010	0.016	0.013	0.022	0.004	0.035	0.043	0.021	0.014	0.002	0.008	0.019
Ti	0.011	0.013	0.010	0.012	0.013	0.021	0.020	0.012	0.011	0.010	0.011	0.011
Cr	0.012	0.014	0.006	0.012	0.001	0.004	0.006	0.004	0.003	0.006	0.004	0.006
Fe^{+3}	0.056	0.086	0.055	0.062	0.085	0.072	0.049	0.062	0.083	0.061	0.089	0.056
Mg	0.962	0.961	0.963	0.952	0.958	0.935	0.883	0.919	0.934	1.008	0.942	0.928
Fe^{+2}	0.100	0.075	0.082	0.083	0.075	0.128	0.133	0.110	0.090	0.084	0.074	0.111
Mn	0.006	0.003	0.004	0.005	0.004	0.004	0.006	0.003	0.003	0.006	0.005	0.004
Ni	0.002	0.000	0.001	0.000	0.000	0.000	0.000	0.000	0.000	0.003	0.000	0.001
Ca	0.843	0.841	0.867	0.856	0.872	0.805	0.851	0.868	0.867	0.825	0.878	0.867
Na	0.018	0.021	0.019	0.018	0.017	0.021	0.023	0.022	0.022	0.015	0.017	0.016
Total	2.019	2.029	2.018	2.021	2.028	2.024	2.016	2.021	2.028	2.020	2.030	2.019
%												
En	48.92	48.87	48.86	48.64	48.04	48.10	45.95	46.85	47.22	50.80	47.38	47.23
Fs	8.22	8.35	7.12	7.63	8.21	10.47	9.77	8.91	8.92	7.59	8.49	8.67
Wo	42.86	42.78	44.01	43.73	43.75	41.43	44.28	44.24	43.86	41.60	44.13	44.10

Sample	CHI03 (*E2*: $(SiO_2)_{adj}$= 61.96 %, $(MgO)_{adj}$= 5.25%)				CHI77 (*E2*: $(SiO_2)_{adj}$= 62.72 %, $(MgO)_{adj}$= 4.86%)		CHI29 (*E2*: $(SiO_2)_{adj}$= 64.34 %, $(MgO)_{adj}$= 2.81%)					
Analysis	Core	Core	Core	Core	Core	Core	Core	Rim	Core	Rim	Core	Rim
%												
SiO_2	53.103	52.686	51.898	52.548	53.197	51.382	50.660	50.709	51.202	52.427	52.462	52.184
TiO_2	0.369	0.453	0.374	0.385	0.281	0.739	0.532	0.599	0.574	0.406	0.524	0.287
Al_2O_3	1.362	2.175	1.936	1.908	1.686	2.407	4.142	4.001	2.952	1.734	2.360	2.024
FeO^t	5.566	5.553	5.019	5.074	5.780	7.623	7.844	8.241	7.681	6.401	7.158	6.242
MnO	0.137	0.212	0.126	0.207	0.138	0.158	0.247	0.206	0.195	0.209	0.204	0.163
MgO	17.432	16.598	16.398	16.999	16.937	16.006	14.199	14.493	15.591	16.258	15.532	15.786
CaO	20.732	21.978	21.861	21.677	21.786	20.685	20.664	20.630	21.157	21.324	21.588	21.103
Na_2O	0.271	0.298	0.262	0.235	0.349	0.274	0.645	0.578	0.349	0.303	0.383	0.403
NiO	0.047	0.047	0.026	0.000	0.047	0.032	0.000	0.032	0.000	0.000	0.000	0.017
Cr_2O_3	0.144	0.208	0.154	0.187	0.217	0.073	0.110	0.077	0.094	0.178	0.087	0.341
Total	99.160	100.210	98.050	99.220	100.418	99.379	99.043	99.566	99.795	99.240	100.298	98.550
Si	1.959	1.932	1.941	1.940	1.947	1.914	1.897	1.892	1.903	1.946	1.933	1.949
Al IV	0.041	0.068	0.059	0.060	0.053	0.086	0.103	0.108	0.097	0.054	0.067	0.051
Sum	2.000	2.000	2.000	2.000	2.000	2.000	2.000	2.000	2.000	2.000	2.000	2.000
Al VI	0.019	0.026	0.027	0.023	0.019	0.020	0.079	0.068	0.032	0.022	0.036	0.038
Ti	0.010	0.012	0.011	0.011	0.008	0.021	0.015	0.017	0.016	0.011	0.015	0.008
Cr	0.004	0.006	0.005	0.005	0.006	0.002	0.003	0.002	0.003	0.005	0.003	0.010
Fe^{+3}	0.025	0.047	0.038	0.039	0.055	0.062	0.056	0.070	0.082	0.039	0.039	0.025
Mg	0.959	0.908	0.914	0.936	0.924	0.889	0.792	0.806	0.864	0.900	0.853	0.879
Fe^{+2}	0.147	0.124	0.119	0.118	0.121	0.175	0.189	0.187	0.157	0.160	0.181	0.170
Mn	0.004	0.007	0.004	0.006	0.004	0.005	0.008	0.007	0.006	0.007	0.006	0.005
Ni	0.001	0.001	0.001	0.000	0.001	0.001	0.000	0.001	0.000	0.000	0.000	0.001
Ca	0.820	0.864	0.876	0.858	0.854	0.826	0.829	0.824	0.842	0.848	0.852	0.844
Na	0.019	0.021	0.019	0.017	0.025	0.020	0.047	0.042	0.025	0.022	0.027	0.029
Total	2.008	2.016	2.013	2.013	2.019	2.021	2.019	2.023	2.027	2.013	2.013	2.008
%												
En	49.06	46.59	46.86	47.83	47.16	45.43	42.27	42.55	44.28	46.07	44.15	45.70
Fs	9.01	9.08	8.25	8.34	9.25	12.39	13.52	13.92	12.55	10.51	11.74	10.40
Wo	41.93	44.33	44.89	43.83	43.59	42.19	44.21	43.53	43.18	43.42	44.10	43.90

Appendix A7. Continued.

Sample	CHI21 (*DISQ*: $(SiO_2)_{adj}$= 63.48%, $(MgO)_{adj}$= 3.51%)						CHI69 (*E1*: $(SiO_2)_{adj}$= 55.30%, $(MgO)_{adj}$= 6.12%)		CHI11 (*DISQ*: $(SiO_2)_{adj}$= 61.20%, $(MgO)_{adj}$= 4.43%)*		CHI08 (*DISQ*: $(SiO_2)_{adj}$= 61.63%, $(MgO)_{adj}$= 4.17%)*	
Analysis	Core	Rim	Core	Rim	Core	Rim	Core	Rim	Core	Rim	Core	Rim
%												
SiO_2	50.300	51.800	51.562	51.589	52.860	52.868	51.081	51.751	53.47	53.58	51.501	51.308
TiO_2	0.810	0.627	0.477	0.377	0.338	0.315	0.790	0.659	0.06	0.06	0.595	0.508
Al_2O_3	3.581	2.493	2.831	1.640	1.477	1.549	3.317	3.175	0.31	1.56	2.461	2.692
FeO^t	7.701	6.639	6.498	7.312	6.440	5.885	5.673	5.489	7.46	8.48	5.651	5.742
MnO	0.171	0.128	0.131	0.256	0.225	0.185	0.190	0.071	0.20	0.23	0.175	0.071
MgO	15.311	15.763	16.393	16.521	17.007	17.409	16.156	16.237	15.25	15.17	16.995	14.451
CaO	22.279	22.704	22.006	22.327	21.081	21.720	21.083	21.650	21.89	19.95	21.418	24.318
Na_2O	0.316	0.354	0.474	0.247	0.298	0.344	0.335	0.416	0.24	0.51	0.307	0.314
NiO	0.000	0.000	0.000	0.012	0.017	0.000	0.022	0.054	0.03	0.00	0.114	0.041
Cr_2O_3	0.090	0.106	0.106	0.030	0.070	0.145	0.674	0.733	0.00	0.00	0.219	0.009
Total	100.56	100.61	100.48	100.310	99.810	100.420	99.321	100.235	98.91	99.54	99.440	99.450
Si	1.865	1.908	1.898	1.913	1.949	1.937	1.893	1.899	2.000	1.987	1.907	1.913
Al IV	0.135	0.092	0.102	0.087	0.051	0.063	0.107	0.101	0.000	0.013	0.093	0.087
Sum	2.000	2.000	2.000	2.000	2.000	2.000	2.000	2.000	2.000	2.000	2.000	2.000
Al VI	0.021	0.016	0.021	0.015	0.013	0.004	0.038	0.037	0.013	0.055	0.014	0.031
Ti	0.023	0.017	0.013	0.011	0.009	0.009	0.022	0.018	0.002	0.002	0.017	0.014
Cr	0.003	0.003	0.003	0.001	0.002	0.004	0.020	0.021	0.000	0.000	0.006	0.000
Fe^{+3}	0.132	0.094	0.127	0.146	0.058	0.092	0.045	0.053	0.001	0.000	0.091	0.075
Mg	0.846	0.866	0.900	0.913	0.935	0.951	0.892	0.888	0.850	0.839	0.938	0.803
Fe^{+2}	0.107	0.110	0.073	0.081	0.141	0.088	0.131	0.115	0.232	0.263	0.083	0.104
Mn	0.005	0.004	0.004	0.008	0.007	0.006	0.006	0.002	0.006	0.007	0.005	0.002
Ni	0.000	0.000	0.000	0.000	0.001	0.000	0.001	0.002	0.001	0.000	0.003	0.001
Ca	0.885	0.896	0.868	0.887	0.833	0.853	0.837	0.851	0.877	0.793	0.850	0.971
Na	0.023	0.025	0.034	0.018	0.021	0.024	0.024	0.030	0.017	0.037	0.022	0.023
Total	2.044	2.032	2.043	2.049	2.019	2.031	2.015	2.018	2.000	1.995	2.031	2.025
%												
En	42.84	43.94	45.63	44.88	47.38	47.80	46.70	46.51	43.23	44.11	47.66	41.07
Fs	12.36	10.58	10.35	11.54	10.42	9.35	9.51	8.93	12.18	14.21	9.17	9.27
Wo	44.80	45.48	44.02	43.58	42.20	42.85	43.79	44.56	44.59	41.68	43.17	49.66

* Geochemical and Sr-Nd isotopic whole-rock composition reported by Verma (1999).

Appendix A8. Representative compositional data and structural formula for plagioclase in volcanic rocks from the SCN.

Sample	CHI64 (*HMI*: $(SiO_2)_{adj}$= 53.64 %, $(MgO)_{adj}$= 8.67%)								
%									
SiO_2	52.369	52.125	52.890	51.808	52.200	52.203	52.224	52.801	52.419
TiO_2	0.054	0.111	0.071	0.071	0.083	0.071	0.065	0.081	0.009
Al_2O_3	30.129	30.545	30.196	29.934	29.380	30.292	29.664	30.523	30.247
FeO^t	0.589	0.613	0.619	0.666	0.545	0.666	0.554	0.517	0.631
MnO	0.000	0.000	0.066	0.040	0.012	0.000	0.000	0.000	0.000
MgO	0.169	0.218	0.174	0.238	0.253	0.185	0.181	0.144	0.180
CaO	13.213	13.455	12.655	13.302	13.163	13.282	13.114	13.458	13.245
Na_2O	3.897	3.828	4.354	3.898	3.867	3.987	3.820	3.993	4.266
K_2O	0.126	0.116	0.145	0.115	0.167	0.118	0.125	0.121	0.125
BaO	0.000	0.000	0.000	0.000	0.000	0.000	0.000	0.000	0.000
SrO	0.041	0.000	0.033	0.000	0.000	0.000	0.000	0.000	0.033
Total	100.587	101.011	101.203	100.072	99.670	100.804	99.747	101.638	101.155
Si	2.368	2.350	2.377	2.359	2.382	2.358	2.380	2.363	2.362
Ti	0.002	0.004	0.002	0.002	0.003	0.002	0.002	0.003	0.000
Al	1.606	1.623	1.600	1.607	1.581	1.613	1.593	1.611	1.607
Fe^{+3}	0.020	0.021	0.021	0.023	0.019	0.023	0.019	0.017	0.021
Sum	3.997	3.997	4.000	3.991	3.985	3.997	3.994	3.994	3.990
Mg	0.011	0.015	0.012	0.016	0.017	0.012	0.012	0.010	0.012
Mn	0.000	0.000	0.003	0.002	0.000	0.000	0.000	0.000	0.000
Ca	0.640	0.650	0.609	0.649	0.644	0.643	0.640	0.645	0.639
Na	0.342	0.335	0.379	0.344	0.342	0.349	0.337	0.347	0.373
K	0.007	0.007	0.008	0.007	0.010	0.007	0.007	0.007	0.007
Sr	0.001	0.000	0.001	0.000	0.000	0.000	0.000	0.000	0.001
Total	1.002	1.006	1.012	1.017	1.013	1.011	0.997	1.009	1.032
%									
An	64.722	65.570	61.116	64.911	64.653	64.359	65.000	64.616	62.733
Ab	34.543	33.757	38.050	34.421	34.370	34.960	34.262	34.692	36.562
Or	0.735	0.673	0.834	0.668	0.977	0.681	0.738	0.692	0.705

Sample	CHI33 (*E1*: $(SiO_2)_{adj}$= 56.95%, $(MgO)_{adj}$= 6.20%)				CHI63 (*DISQ*: $(SiO_2)_{adj}$= 59.07%, $(MgO)_{adj}$= 4.78%)		CHI27 (*E1*: $(SiO_2)_{adj}$= 59.91%, MgO= 4.47%)	
%								
SiO_2	50.766	51.301	51.417	50.479	52.335	53.740	52.674	52.938
TiO_2	0.044	0.043	0.039	0.037	0.044	0.062	0.039	0.088
Al_2O_3	30.663	29.869	29.979	30.295	29.873	28.586	29.066	28.858
FeO^t	0.424	0.528	0.468	0.450	0.549	0.414	0.659	0.648
MnO	0.000	0.000	0.000	0.000	0.000	0.000	0.020	0.000
MgO	0.189	0.102	0.153	0.146	0.129	0.123	0.156	0.172
CaO	14.687	13.794	14.095	14.242	13.177	11.808	13.066	12.779
Na_2O	3.562	3.912	3.813	3.632	4.118	4.670	4.386	4.666
K_2O	0.111	0.148	0.117	0.131	0.175	0.183	0.234	0.257
BaO	0.035	0.017	0.000	0.007	0.000	0.000	0.000	0.022
SrO	0.000	0.000	0.038	0.023	0.000	0.000	0.009	0.012
Total	100.481	99.714	100.119	99.442	100.400	99.586	100.309	100.440
Si	2.311	2.348	2.345	2.320	2.373	2.443	2.394	2.403
Ti	0.002	0.001	0.001	0.001	0.002	0.002	0.001	0.003
Al	1.646	1.612	1.612	1.641	1.597	1.532	1.557	1.544
Fe^{+3}	0.015	0.018	0.016	0.016	0.019	0.014	0.023	0.022
Sum	3.973	3.980	3.974	3.978	3.990	3.992	3.975	3.972
Mg	0.013	0.007	0.010	0.010	0.009	0.008	0.011	0.012
Mn	0.000	0.000	0.000	0.000	0.000	0.000	0.001	0.000
Ca	0.716	0.677	0.689	0.701	0.640	0.575	0.636	0.622
Na	0.314	0.347	0.337	0.324	0.362	0.412	0.387	0.411
K	0.006	0.009	0.007	0.008	0.010	0.011	0.014	0.015
Ba	0.001	0.000	0.000	0.000	0.000	0.000	0.000	0.000
Sr	0.000	0.000	0.001	0.001	0.000	0.000	0.000	0.000
Total	1.051	1.040	1.044	1.043	1.021	1.006	1.048	1.059
An	69.067	65.532	66.693	67.915	63.238	57.666	61.397	59.359
Ab	30.311	33.631	32.648	31.341	35.762	41.270	37.294	39.220
Or	0.622	0.837	0.659	0.744	1.000	1.064	1.309	1.421

Appendix A8. Continued.

Sample	CHI79 (*DISQ*: $(SiO_2)_{adj}$= 63.51%, $(MgO)_{adj}$= 1.90%)		CHI69 (*E1*: $(SiO_2)_{adj}$= 55.30%, $(MgO)_{adj}$= 6.12%)		CHI10 (*DISQ*: $(SiO_2)_{adj}$ 63.47%, MgO= 3.34%)*		CHI49 (*DISQ*: $(SiO_2)_{adj}$= 65.04%, MgO= 2.99%)	
%								
SiO_2	53.012	53.037	51.928	51.091	55.643	56.436	61.63	61.48
TiO_2	0.117	0.072	0.044	0.078	0.037	0.045	0.00	0.00
Al_2O_3	29.184	28.983	30.078	30.710	26.718	26.471	23.85	24.40
FeO^t	0.733	0.688	0.632	0.630	0.582	0.125	0.14	0.10
MnO	0.000	0.000	0.000	0.030	0.000	0.000	0.04	0.00
MgO	0.084	0.091	0.121	0.136	0.021	0.011	0.02	0.01
CaO	12.064	11.842	13.330	13.550	9.758	9.053	5.55	5.73
Na_2O	4.497	4.595	3.759	3.741	6.007	6.269	8.61	7.96
K_2O	0.238	0.227	0.186	0.163	0.447	0.341	0.52	0.50
BaO	0.000	0.058	0.026	0.000	0.000	0.000	0.000	0.000
SrO	0.000	0.015	0.006	0.048	0.000	0.000	0.000	0.000
Total	99.929	99.608	100.110	100.177	99.213	98.751	100.360	100.180
Si	2.410	2.418	2.362	2.327	2.534	2.567	2.735	2.726
Ti	0.004	0.002	0.002	0.003	0.001	0.002	0.000	0.000
Al	1.564	1.558	1.613	1.649	1.434	1.420	1.248	1.276
Fe^{+3}	0.025	0.024	0.022	0.022	0.020	0.004	0.005	0.003
Sum	4.003	4.002	3.998	4.000	3.989	3.992	3.988	4.005
Mg	0.006	0.006	0.008	0.009	0.001	0.001	0.001	0.001
Mn	0.000	0.000	0.000	0.001	0.000	0.000	0.002	0.000
Ca	0.588	0.578	0.650	0.661	0.476	0.441	0.264	0.272
Na	0.396	0.406	0.332	0.330	0.530	0.553	0.741	0.684
K	0.014	0.013	0.011	0.009	0.026	0.020	0.029	0.028
Ba	0.000	0.001	0.000	0.000	0.000	0.000	0.000	0.000
Sr	0.000	0.000	0.000	0.001	0.000	0.000	0.000	0.000
Total	1.003	1.005	1.001	1.013	1.034	1.015	1.037	0.986
%								
An	58.892	57.972	65.492	66.054	46.115	43.517	25.518	27.642
Ab	39.725	40.705	33.420	33.000	51.370	54.531	71.635	69.486
Or	1.383	1.323	1.088	0.946	2.515	1.952	2.847	2.872

* Geochemical and Sr-Nd isotopic whole-rock composition reported by Verma (1999).

Appendix A9. Compositional data and structural formula for plagioclase phenocrysts with oscillatory zonation in volcanic rocks (*DISQ*-group) from the SCN.

(a) CHI10 ($(SiO_2)_{adj}$= 63.5%, $(MgO)_{adj}$= 3.34%; data from Verma 1999)

Analysis	1(Core)	2	3	4	5	6	7	8	9	10 (Rim)
%										
SiO_2	58.396	59.836	57.155	57.376	58.090	56.981	58.953	59.934	60.812	60.847
TiO_2	0.020	0.000	0.044	0.000	0.031	0.018	0.000	0.000	0.000	0.000
Al_2O_3	25.279	24.712	26.608	26.151	25.616	26.705	25.487	24.447	23.935	23.991
FeO^t	0.162	0.102	0.135	0.142	0.172	0.087	0.105	0.085	0.057	0.157
MnO	0.045	0.033	0.003	0.011	0.000	0.000	0.000	0.011	0.000	0.000
MgO	0.000	0.000	0.021	0.005	0.011	0.014	0.019	0.026	0.025	0.000
CaO	7.580	6.882	8.864	8.655	7.790	8.899	7.522	6.808	6.372	6.153
Na_2O	7.276	7.621	6.585	6.700	6.901	6.667	7.173	7.635	7.477	7.397
K_2O	0.336	0.361	0.225	0.391	0.671	0.233	0.384	0.451	0.918	1.014
Total	99.094	99.547	99.640	99.431	99.282	99.604	99.643	99.397	99.596	99.559
Si	2.638	2.682	2.574	2.591	2.623	2.569	2.644	2.690	2.722	2.724
Ti	0.001	0.000	0.001	0.000	0.001	0.001	0.000	0.000	0.000	0.000
Al	1.346	1.306	1.413	1.392	1.364	1.419	1.348	1.294	1.263	1.266
Fe^{+3}	0.006	0.003	0.005	0.005	0.006	0.003	0.004	0.003	0.002	0.005
Sum	3.990	3.991	3.993	3.988	3.994	3.991	3.995	3.987	3.987	3.996
Mg	0.000	0.000	0.001	0.000	0.001	0.001	0.001	0.002	0.002	0.000
Mn	0.002	0.001	0.000	0.000	0.000	0.000	0.000	0.000	0.000	0.000
Ca	0.367	0.331	0.428	0.419	0.377	0.430	0.362	0.327	0.306	0.295
Na	0.637	0.662	0.575	0.587	0.604	0.583	0.624	0.665	0.649	0.642
K	0.019	0.021	0.013	0.023	0.039	0.013	0.022	0.026	0.052	0.058
Total	1.025	1.015	1.017	1.029	1.021	1.027	1.009	1.020	1.009	0.995
%										
An	35.845	32.612	42.114	40.740	36.960	41.896	35.889	32.172	30.350	29.659
Ab	62.263	65.351	56.614	57.069	59.249	56.798	61.930	65.290	64.444	64.521
Or	1.892	2.037	1.273	2.191	3.791	1.306	2.181	2.538	5.206	5.820

(b) CHI79 ($(SiO_2)_{adj}$ = 63.51%, $(MgO)_{adj}$ = 1.90%)

Analysis	1 (Core)	2	3	4	5	6	7	8	9 (Rim)
%									
SiO_2	46.598	47.548	47.963	48.348	48.794	47.937	47.843	48.705	46.942
TiO_2	0.000	0.000	0.020	0.032	0.014	0.023	0.048	0.039	0.000
Al_2O_3	34.263	34.031	33.348	33.075	33.003	33.789	33.451	33.056	34.233
FeO^t	0.365	0.396	0.389	0.339	0.377	0.365	0.330	0.398	0.497
MnO	0.000	0.000	0.038	0.000	0.000	0.000	0.000	0.000	0.027
MgO	0.047	0.078	0.052	0.044	0.035	0.030	0.064	0.045	0.051
CaO	17.610	17.268	16.585	15.871	16.304	16.747	16.865	16.058	17.273
Na_2O	1.625	1.759	2.161	2.357	2.308	1.946	2.037	2.290	1.685
K_2O	0.035	0.019	0.034	0.036	0.054	0.041	0.044	0.049	0.039
BaO	0.000	0.060	0.000	0.000	0.051	0.000	0.000	0.003	0.028
SrO	0.000	0.022	0.016	0.000	0.000	0.000	0.001	0.010	0.012
Total	100.543	101.181	100.606	100.102	100.940	100.878	100.683	100.653	100.787
Si	2.135	2.161	2.189	2.211	2.217	2.181	2.183	2.216	2.144
Ti	0.000	0.000	0.001	0.001	0.000	0.001	0.002	0.001	0.000
Al	1.850	1.824	1.795	1.784	1.767	1.812	1.799	1.773	1.844
Fe^{+3}	0.013	0.014	0.013	0.012	0.013	0.012	0.011	0.014	0.017
Sum	3.998	3.999	3.998	4.008	3.997	4.006	3.995	4.005	4.005
Mg	0.003	0.005	0.004	0.003	0.002	0.002	0.004	0.003	0.003
Mn	0.000	0.000	0.001	0.000	0.000	0.000	0.000	0.000	0.001
Ca	0.864	0.841	0.811	0.778	0.794	0.816	0.824	0.783	0.845
Na	0.144	0.155	0.191	0.209	0.203	0.172	0.180	0.202	0.149
K	0.002	0.001	0.002	0.002	0.003	0.002	0.003	0.003	0.002
Ba	0.000	0.001	0.000	0.000	0.001	0.000	0.000	0.000	0.001
Sr	0.000	0.001	0.000	0.000	0.000	0.000	0.000	0.000	0.000
Total	1.014	1.004	1.010	0.992	1.003	0.992	1.012	0.991	1.002
%									
An	85.518	84.343	80.761	78.651	79.358	82.428	81.855	79.259	84.802
Ab	14.280	15.547	19.042	21.136	20.329	17.332	17.891	20.453	14.970
Or	0.202	0.110	0.197	0.212	0.313	0.240	0.254	0.288	0.228

Appendix A10. Compositional data and structural formula for biotite in volcanic rocks (CHI21: $(SiO_2)_{adj}$= 64.32%, $(MgO)_{adj}$= 3.39%) from the SCN.

Analysis	1	2
%		
SiO_2	42.988	42.885
TiO_2	2.163	2.157
Al_2O_3	10.552	10.549
FeO^T	15.747	15.658
MnO	0.250	0.260
MgO	19.385	19.298
CaO	8.583	8.562
Na_2O	1.700	1.705
K_2O	0.088	0.078
Total	101.460	101.150
Si	5.87	5.87
Al IV	2.13	2.13
Sum	8.00	8.00
Ti	0.22	0.22
Mg	3.95	3.94
Fe^{+2}	1.80	1.79
Mn	0.03	0.03
Total	6.00	5.98
Ca	1.26	1.26
Na	0.45	0.45
K	0.02	0.01
Total	1.72	1.72
Sum of cations	15.72	15.71
Fe^{+2} / (Fe^{+2} + Mg)	0.31	0.31

Appendix A11. Average compositions of the SCN volcanic rocks used in geochemical modeling.

Element	M (mafic magmas)												HMI (high-Mg intermediate magmas)					
	B			TB			BTA			BA			BA			BTA		
	n	$\bar{x}$	*s*	*n*	$\bar{x}$	*s*	*n*	$\bar{x}$	*s*	*n*	$\bar{x}$	*s*	*n*	$\bar{x}$	*s*	*n*	$\bar{x}$	*s*
$(SiO_2)_{adj}$	12	50.7	0.9	8	50.6	0.6	15	52.08	0.39	8	52.41	0.25	25	53.9	0.6	6	54.0	0.7
$(TiO_2)_{adj}$	12	1.76	0.11	8	1.84	0.13	14	1.67	0.09	8	1.60	0.15	26	1.04	0.31	6	1.03	0.17
$(Al_2O_3)_{adj}$	11	16.08	0.36	8	15.88	0.36	15	15.8	0.6	8	15.91	0.42	25	15.78	0.41	6	15.7	0.6
$(Fe_2O_3)_{adj}$	12	1.53	0.07	8	2.14	0.08	14	2.21	0.06	8	1.96	0.09	25	1.72	0.10	6	1.87	0.09
$(FeO)_{adj}$	12	7.67	0.33	8	7.12	0.25	14	6.32	0.16	8	6.55	0.29	25	5.74	0.33	6	5.33	0.26
$(MnO)_{adj}$	12	0.155	0.006	8	0.150	0.007	15	0.149	0.009	8	0.144	0.010	26	0.131	0.009	6	0.126	0.005
$(MgO)_{adj}$	12	8.57	0.34	8	8.1	0.5	15	8.1	0.6	8	8.3	0.5	26	8.9	0.8	6	8.7	0.8
$(CaO)_{adj}$	12	8.5	0.8	8	8.44	0.37	15	7.57	0.30	8	7.75	0.45	26	7.68	0.25	6	7.46	0.24
$(Na_2O)_{adj}$	12	3.56	0.27	7	3.88	0.13	15	4.32	0.20	7	3.56	0.08	26	3.61	0.30	6	4.35	0.17
$(K_2O)_{adj}$	12	1.10	0.23	8	1.20	0.10	15	1.26	0.11	8	1.28	0.14	26	1.01	0.13	6	1.17	0.28
$(P_2O_5)_{adj}$	12	0.45	0.06	8	0.55	0.07	14	0.48	0.11	8	0.47	0.10	24	0.20	0.05	6	0.270	0.032
Mg#	12	66.56	1.41	8	67.0	1.6	15	69.2	2.1	8	69.3	1.9	26	73.0	3.0	6	74.4	1.4
La	8	17.7	3.8	7	21.7	1.2	10	24	5	3	20	5	9	16	7	6	16.7	4.5
Ce	7	42	10	7	49.3	1.8	9	58	11	3	44	10	9	35	10	6	40	7
Pr	3	5.4	1.8				1	9.7		3	5.8	1.6	3	4.1	1.4			
Nd	7	22	6	7	26.4	3.8	1	41		3	24	6	7	19	5			
Sm	7	5.2	1.4	6	5.9	0.21	1	8.4		3	5.3	1.0	7	4.6	1.1			
Eu	8	1.72	0.39	7	1.92	0.13	2	2.20	0.36	3	1.83	0.31	7	1.48	0.33			
Gd	3	5.5	2.1				2	5.9	3.2	3	5.3	0.7	3	4.0	1.0			
Tb	8	0.80	0.17	7	0.87	0.08	3	0.87	0.39	3	0.85	0.08	7	0.68	0.15			
Dy							1	2.97		3	4.82	0.43	3	3.9	0.8			
Ho	3	0.90	0.34				2	1.0	0.6	3	0.95	0.10	3	0.77	0.15			
Er	3	2.5	0.9				2	2.7	1.4	3	2.73	0.21	3	2.15	0.30			
Tm	3	0.36	0.14				2	0.39	0.20	3	0.395	0.023	3	0.31	0.05			
Yb	7	2.5	0.6	7	2.90	0.27	1	4.36		3	2.41	0.13	7	2.18	0.40			
Lu	7	0.36	0.11	7	0.379	0.038	1	0.66		3	0.377	0.020	7	0.31	0.07			
Ba	8	250	60	8	325	110	12	350	60	3	339	110	23	248	16	6	370	90
Co	8	39	5	7	36.3	2.0	2	41	13	3	36.6	3.2	5	32.3	0.8			
Cr	8	281	38	7	281	8	4	247	35	3	301	31	22	420	100			
Hf	6	4.3	0.6	5	4.28	0.22	1	4.47		3	4.4	0.6	7	3.9	0.6			
Nb	3	18.2	1.5	1	23		10	20.3	5.7	3	12.6	2.1	16	5.0	1.2	6	6.5	2.6
Ni	8	146	14	8	153	21	12	162	26	3	144	38	23	213	38	6	197	43
Pb	2	8.5	0.7	3	9.7	4.2							2	8	5	1	6.0	
Rb	7	18.1	3.5	5	22.2	3.2	12	23.8	2.1	3	21.3	1.5	22	19.5	2.9	6	21	5
Sc	2	23.5	2.1							2	22		4	20.1	1.2			
Sr	8	502	50	8	507	39	11	506	26	3	520	90	19	395	24	6	560	100
Ta	6	1.05	0.32	7	1.07	0.24	1	1.19		3	0.90	0.26	7	0.64	0.33			
Th	6	1.74	0.25	6	1.87	0.08	1	2.78		3	2.53	0.41	7	2.2	0.6			
U	6	0.57	0.20	6	0.78	0.15	1	0.77		2	0.75	0.21	4	0.74	0.32			
V	6	157	18	7	149	16	3	148	17	3	157.7	2.0	22	154	7			
Y	7	29.4	2.6	8	30.8	1.8	11	31.9	3.9	3	25.3	1.5	23	20.5	3.6	5	23.4	0.5
Zr	8	199	20	8	228	30	12	240	50	3	183	27	17	128	8	6	150	25

Appendix A11. Continued.

Element	E1 (ol + opx ± cpx ± plg evolved-type magmas)												E2 (opx ± cpx ± plg evolved-type magmas)								
	BTA			BA			TA			A			BTA + TA + BA			A			D		
	n	$\bar{x}$	*s*	*n*	$\bar{x}$	*s*	*n*	$\bar{x}$	*s*	*n*	$\bar{x}$	*s*	*n*	$\bar{x}$	*s*	*n*	$\bar{x}$	*s*	*n*	$\bar{x}$	*s*
SiO_2	30	54.4	1.4	17	56.0	0.6	5	58.2	1.7	37	59.5	1.1	5	55.1	0.6	60	61.0	1.0	30	64.5	1.1
TiO_2	30	1.52	0.31	17	1.27	0.15	5	0.99	0.19	37	1.01	0.16	6	1.26	0.07	53	0.85	0.10	30	0.73	0.08
Al_2O_3	30	16.1	0.7	18	16.4	0.5	5	15.82	0.44	37	16.29	0.45	6	16.46	0.14	58	16.21	0.41	28	16.36	0.37
Fe_2O_3	30	2.05	0.24	16	1.63	0.05	5	1.73	0.22	37	1.57	0.13	6	1.81	0.13	55	1.41	0.08	30	1.26	0.13
FeO	30	5.9	0.7	16	5.42	0.18	5	4.3	0.5	37	4.49	0.37	5	5.55	0.09	55	3.16	0.33	30	3.16	0.33
MnO	30	0.138	0.017	17	0.125	0.007	4	0.109	0.009	36	0.106	0.010	6	0.115	0.005	60	0.096	0.010	30	0.083	0.010
MgO	30	6.4	1.2	18	6.4	0.7	5	5.9	0.9	37	4.9	0.8	5	6.20	0.27	60	4.4	0.6	30	2.7	0.5
CaO	30	7.19	0.30	18	7.11	0.38	5	6.2	0.5	37	6.13	0.45	5	7.40	0.27	59	5.66	0.45	30	4.58	0.30
Na_2O	30	4.25	0.27	17	3.89	0.12	4	4.598	0.030	37	4.08	0.29	6	4.28	0.28	59	4.19	0.20	30	4.36	0.24
K_2O	28	1.44	0.15	18	1.30	0.14	5	1.83	0.15	36	1.67	0.18	6	1.44	0.22	59	1.72	0.16	30	1.92	0.17
P_2O_5	30	0.57	0.25	17	0.32	0.07	5	0.30	0.07	37	0.29	0.09	6	0.44	0.06	58	0.25	0.05	30	0.203	0.030
Mg#	30	66	5	18	67.0	3.3	5	70.7	3.5	37	65.6	3.9	6	65.7	2.2	59	65.8	3.3	30	60.2	3.9
La	27	29	10	7	18.3	4.2	4	24	5	22	20	6	5	26.4	3.7	51	20.2	4.2	22	19.2	3.9
Ce	25	67	20	7	41	8	4	54	6	22	46	11	5	57	7	50	44	9	22	43	7
Pr	1	5.7		3	5.7	0.8				5	5.0	1.8	5	7.5	0.9	13	5.6	1.1	5	4.6	0.8
Nd	12	35	11	5	23.2	4.5				9	22	5	5	32.6	3.9	36	22	5	7	19.8	3.6
Sm	12	7.5	2.2	5	5.1	0.8				9	4.5	1.0	5	6.9	0.7	36	4.6	0.8	7	4.00	0.45
Eu	12	2.2	0.6	5	1.62	0.27				9	1.32	0.26	5	2.03	0.20	36	1.36	0.19	7	1.17	0.13
Gd	1	5.49		3	4.95	0.37				5	3.9	1.2	5	5.5	0.5	12	3.9	0.5	4	3.8	0.5
Tb	12	0.95	0.26	5	0.78	0.12				9	0.60	0.13	5	0.80	0.06	35	0.59	0.07	5	0.576	0.043
Dy				2	4.74	0.13				2	4.4	1.0	5	4.47	0.19	10	3.31	0.35	3	3.4	0.8
Ho	1	0.92		3	0.88	0.09				5	0.68	0.21	5	0.940	0.042	13	0.69	0.14	4	0.65	0.13
Er	1	2.57		3	2.46	0.19				5	1.9	0.6	4	2.17	0.11	13	1.82	0.36	4	1.87	0.36
Tm	1	0.35		3	0.352	0.033				5	0.27	0.10	4	0.320	0.014	13	0.27	0.05	4	0.27	0.05
Yb	13	3.1	0.9	5	2.24	0.30				8	1.66	0.36	5	2.23	0.12	37	1.73	0.21	7	1.66	0.24
Lu	12	0.43	0.12	4	0.319	0.028				9	0.28	0.06	5	0.340	0.025	35	0.249	0.036	7	0.25	0.07
Ba	29	450	90	14	370	60	5	500	70	36	500	90	6	480	60	60	500	80	28	530	70
Co	13	27	7	5	26.9	4.0				9	25	8	5	25.1	0.6	35	30	15	6	13.0	3.6
Cr	15	180	50	11	210	60	1	118		23	150	50	6	210	60	44	150	50	12	78	14
Hf	12	5.9	1.4	4	4.5	0.6				5	3.96	0.05				25	4.2	0.5	5	4.5	0.6
Nb	17	18	9	12	13	6	5	8.8	4.4	32	11	5	6	12.0	1.8	33	7.2	2.6	26	7.1	1.7
Ni	28	116	43	14	100	50	4	140	7	36	78	37	6	81	22	54	72	24	27	38	15
Pb	6	7.8	1.7							6	6.5	1.5				6	11.5	2.6	3	8.7	0.6
Rb	26	27	6	14	28.0	2.8	5	32.2	3.2	36	37	9	6	26	6	58	36	8	28	45	7
Sc	3	19.2	2.7	2	17.5	2.1				2	16.5	0.7				15	12.9	1.2	4	10.6	1.8
Sr	22	521	20	14	530	70	5	710	180	35	515	70	6	660	90	60	520	80	27	460	50
Ta	11	1.29	0.38	4	0.82	0.13				5	0.61	0.24				25	0.67	0.28	5	0.56	0.18
Th	12	2.9	0.7	4	2.6	0.6				5	3.23	0.19				30	3.5	0.6	5	4.0	1.2
U	11	0.89	0.28	3	0.97	0.06				6	1.16	0.16				28	1.20	0.29	5	1.37	0.29
V	14	137	11	11	138	8	1	99		23	116	12	6	133	16	43	105	13	12	85	7
Y	27	32	8	13	24.2	3.5	5	21.2	3.5	36	24	6	6	24.4	1.5	55	19.7	2.7	28	19.2	2.5
Zr	29	270	90	13	183	33	5	177	31	36	220	70	6	198	26	54	176	31	28	180	23

Appendix A11. Continued.

Element	DISQ (disequilibrium-type magmas)									HB (high-Ba-type magmas)					
	BTA + TA + BA			A			D			HB1			HB2		
	n	$\bar{x}$	s	n	$\bar{x}$	s	n	$\bar{x}$	s	n	$\bar{x}$	s	n	$\bar{x}$	s
SiO_2	5	56.0	1.2	8	60.0	1.5	7	64.5	1.0	4	52.1	1.4	7	57.3	4.4
TiO_2	5	1.15	0.32	8	0.90	0.21	7	0.67	0.05	4	1.00	0.07	7	1.25	0.43
Al_2O_3	5	16.6	0.6	8	16.0	0.5	7	16.7	0.8	4	14.9	0.6	7	15.66	0.44
Fe_2O_3	5	1.71	0.22	8	1.47	0.16	7	1.21	0.09	4	1.88	0.10	7	1.78	0.40
FeO	4	5.25	0.35	8	4.2	0.5	7	3.07	0.21	4	5.6	0.5	7	5.1	1.4
MnO	5	0.122	0.015	8	0.100	0.012	7	0.084	0.005	4	0.131	0.013	7	0.111	0.036
MgO	5	6.2	1.4	8	5.1	0.6	7	2.7	0.6	4	9.0	0.9	7	5.7	1.4
CaO	5	7.09	0.27	8	6.0	0.5	7	4.7	0.5	4	8.9	0.5	7	6.5	1.1
Na_2O	5	4.32	0.34	8	4.24	0.16	7	4.25	0.12	4	3.94	0.40	7	4.02	0.41
K_2O	5	1.37	0.19	8	1.69	0.12	7	1.87	0.24	4	1.92	0.33	7	1.98	0.29
P_2O_5	5	0.38	0.22	8	0.26	0.07	7	0.183	0.026	4	0.56	0.14	7	0.50	0.28
Mg#	4	71.1	0.6	8	68.1	3.0	7	61	5	4	74.1	0.5	7	66.4	3.1
La	3	18	6	7	17.7	2.3	6	16.1	2.8	4	52	13	4	31	6
Ce	3	43	13	7	46	7	5	36.7	4.2	4	116	25	5	75	19
Pr	2	5.4	2.8	3	5.0	1.3	3	4.19	0.45	2	18.4	0.9			
Nd	2	24	12	3	21	7	3	17.2	1.6	2	80.7	4.0	3	33	9
Sm	2	5.2	1.9	3	4.4	1.3	3	3.63	0.35	2	14.9	0.9	3	6.8	1.7
Eu	2	1.55	0.39	3	1.32	0.30	3	1.113	0.015	2	4.05	0.33	3	1.9	0.5
Gd	2	4.5	1.3	3	4.1	0.6	3	3.16	0.16	2	10.31	0.28			
Tb	2	0.71	0.10	3	0.66	0.05	3	0.530	0.026	2	1.30	0.08	3	0.80	0.20
Dy	2	3.855	0.021	1	3.59		3	2.97	0.19	2	6.2	0.6			
Ho	2	0.715	0.007	3	0.70	0.09	3	0.580	0.040	2	1.025	0.021			
Er	2	1.99	0.13	3	1.79	0.12	3	1.65	0.07	2	2.62	0.38			
Tm	2	0.282	0.030	3	0.263	0.021	3	0.2383	0.0029	2	0.36	0.05			
Yb	2	1.80	0.15	3	1.75	0.36	4	1.51	0.14	2	2.28	0.23	3	2.4	0.8
Lu	2	0.268	0.025	3	0.32	0.09	3	0.231	0.009	2	0.323	0.018	3	0.31	0.09
Ba	4	460	100	7	470	60	6	470	60	4	1140	250	5	800	50
Co	2	24.4	0.8	3	17.5	2.2	4	14	8	2	29.6	2.0	3	22	6
Cr	4	210	90	3	140	50	3	92	25	2	320	50	5	180	50
Hf	2	3.70	0.15	1	4.02		2	4.10	0.27	1	5.6		3	5.2	0.7
Nb	5	11	8	7	5.4	1.2	6	5.6	1.3	4	3.7	1.5	4	16	5
Ni	5	110	50	7	73	29	4	38	16	4	212	28	7	103	36
Pb	1	6					1	7.0		1	15.0		2	7.0	1.4
Rb	5	26	6	7	31	6	6	35	12	4	28	7	7	38	11
Sc	1	19					1	11		1	23				
Sr	5	570	110	7	660	50	6	560	90	4	1150	300	5	540	50
Ta	2	0.38	0.05	1	0.40		3	0.467	0.025	1	0.29		3	0.73	0.15
Th	2	2.6	0.6	1	2.84		3	3.63	0.20	1	7.73		3	4.0	1.5
U	1	0.75					1	1.33		1	2.71		3	1.20	0.26
V	4	121	6	3	93	15	4	73	19	2	155	11	5	120	19
Y	4	20.0	2.2	7	19.3	2.8	6	16.3	1.2	4	28.1	1.7	7	28	9
Zr	4	154	18	7	153	21	6	146	9	4	176	34	7	240	60

Appendix A12. Statistical data for the Nb anomaly ($[Nb/Nb^*]_{Primitive\text{-}mantle}$ with respect to Ba and La) for mafic rocks from the SCN and their comparison with arcs and rifts or extension-related area and continental break-up regions around the world as well as with other Mexican provinces (the comparison data from Verma 2006).

Area	n	*m*	*x*±s	95% CL	99% CL
SCN (Mexico)	12	0.69	0.69±0.13	0.61–0.77	0.58–0.81
			Arcs		
Aleutian arc	13	0.11	0.19±0.08	0.14–0.24	0.12–0.26
	* 11	0.15	0.17±0.06	0.13–0.21	0.11–0.22
Burma arc	4	0.09	0.09±0.02	0.05–0.13	0.02–0.16
Central American Volcanic Arc (CAVA)	55	0.13	0.17±0.13	0.14–0.21	0.13–0.22
Izu-Bonin arc	18	0.09	0.16±0.21	0.06–0.27	0.02–0.31
	* 16	0.09	0.10±0.05	0.07–0.13	0.06–0.14
Japan arc	7	0.14	0.19±0.15	0.05–0.33	–
	* 6	0.14	0.15±0.09	0.05–0.24	–
Kamchatka arc	14	0.21	0.34±0.35	0.14–0.54	0.07–0.62
	* 12	0.21	0.22±0.11	0.15–0.29	0.12–0.32
Lesser Antilles arc	45	0.31	0.32±0.12	0.28–0.35	0.28–0.36
Luzon arc	4	0.31	0.30±0.10	0.14–0.47	0.01– 0.60
Marianas arc	8	0.07	0.07±0.04	0.04–0.11	0.02–0.12
New Hebrides arc	10	0.14	0.16±0.04	0.12–0.19	0.11–0.20
Papua - New Guinea arc	3	0.11	0.09±0.02	0.04–0.15	–
Philippines arc	20	0.22	0.21±0.07	0.18–0.25	0.17–0.26
Sangihe arc	3	0.16	0.16±0.01	0.13–0.19	0.09–0.23
Sunda-Banda arc	23	0.15	0.15±0.08	0.11–0.18	0.10–0.20
Tonga-Kermadec arc	8	0.14	0.15±0.08	0.08–0.22	0.05–0.26
Vanuatu arc	5	0.06	0.06±0.02	0.03–0.09	0.01–0.11
			Rift and extension-related areas: with negative Nb anomaly		
Basin and Range	34	0.64	0.69±0.33	0.58–0.81	0.54–0.85
Colorado Plateau-Transition	39	0.63	0.63±0.19	0.57–0.69	0.50–0.74
Rio Grande rift	35	0.81	0.77±0.43	0.62–0.91	0.57–0.97
Western USA	30	0.68	0.73±0.39	0.58–0.88	0.53–0.93
North China	8	0.85	0.84±0.08	0.77–0.90	0.74–0.93
Northeast China	22	0.79	0.78±0.22	0.69–0.88	0.65–0.91
Gregory rift–Kenya	4	0.74	0.77±0.08	0.64–0.90	0.53–1.01
			Continental break-up regions: with negative Nb anomaly		
Columbia River	3	0.37	0.41±0.12	0.12–0.70	–
Deccan - India	12	0.59	0.61±0.19	0.49–0.73	0.44–0.78
Greenland	3	0.79	0.82±0.09	0.59–1.05	0.29–1.36
Paraná - Brazil	1	–	0.49	–	–
			Other Mexican Provinces		
Eastern Alkaline Province	97	0.76	0.80±0.27	0.74–0.85	0.72–0.86
Los Tuxtlas Volcanic Field	22	0.61	0.62±0.20	0.53–0.71	0.50–0.74
Eastern Mexican Volcanic Belt	94	0.49	0.53±0.22	0.48–0.57	0.46–0.59

n= number of samples; *m*= median; *x*= mean; s= standard deviation; 95%CL= 95% confidence limit of the mean; 99%CL= 99% confidence limit of the mean. For CAVA, some basalts from the back-arc Yohoa volcano showing significant positive Nb anomaly were not included in the statistical calculations, otherwise the statistic were not meaningful. *= When the median (m) and mean (x) values for the Nb anomaly showed significant differences, the data were checked for discordant outliers (Barnett & Lewis 1994); in these cases, the statistical data are also presented after outlier detection and elimination. – = means that the 95% or 99% confidence limits were not meaningful for these more dispersed parameters because of the very small number of samples.

Appendix A13. Synthesis of inferred tectonic setting results for Sierra de Chichinautzin (SCN) and Central American Volcanic Arc (CAVA) basic magmas from new multi-dimensional discriminant function based diagrams.

Area of application	Diagram reference	Figure code	Total no. of samples (%)	Number of samples (%) discriminated as					Diagram type
				IAB (1)	CRB+OIB (2+3)	CRB (2)	OIB (3)	MORB (4)	
SCN	VGA2006	Fig_1234m2	28 (100)	2 (7)		**26 (93)**	0	0	
		Fig_123m2	28 (100)	0		**28 (100)**	0		
		Fig_124m2	28 (100)	0		**28 (100)**		0	
		Fig_134m2	28 (100)	2			5	21	Inapplicable
		Fig_234m2	28 (100)			**28 (100)**	0	0	
				Before and after DODESSYS					
SCN	VA2011	Fig_1234t2	4	0	2			2	
		Fig_123t2	4	0		**4**	0		
		Fig_124t2	4	0		**3**		1	
		Fig_134t2	4	0			0	4	Inapplicable
		Fig_234t2	4			**3**	0	1	
CAVA	VGA2006	Fig_1234m2	84 (100)	**67 (80)**		3 (3)	0	14 (17)	
		Fig_123m2	84 (100)	**64 (76)**		12 (14)	8 (10)		
		Fig_124m2	84 (100)	**66 (79)**		5 (6)		13 (15)	
		Fig_134m2	84 (100)	**67 (80)**			2 (2)	15 (18)	
		Fig_234m2	84 (100)			61	0	23	Inapplicable
				Before DODESSYS					
CAVA	VA2011	Fig_1234t2	41 (100)	**26 (64)**	1 (2)			14 (34)	
		Fig_123t2	41 (100)	**35 (85)**		6 (15)	0		
		Fig_124t2	41 (100)	**26 (64)**		1 (2)		14 (34)	
		Fig_134t2	41 (100)	**24 (59)**			1 (2)	16 (39)	
		Fig_234t2	41 (100)			2 (5)	0	39	Inapplicable
				After DODESSYS					
CAVA	VA2011	Fig_1234t2	38 (100)	**24 (63)**	1 (3)			13 (34)	
		Fig_123t2	38 (100)	**33 (87)**		5 (13)	0		
		Fig_124t2	38 (100)	**24 (63)**		1 (3)		13 (34)	
		Fig_134t2	38 (100)	**22 (58)**			1 (3)	15 (39)	
		Fig_234t2	38 (100)			1	0	37	Inapplicable

In Figure code, numbers 1 to 4 refer to the tectonic settings (1–IAB, 2–CRB, 3–OIB, 4–MORB); m2 and t2 are for, respectively, the diagrams proposed by Verma *et al.* (2006) and Verma & Agrawal (2011). Computer program DODESSYS is by Verma & Díaz-González (2012).

Appendix A14. Linear regression coefficients for trace-element inverse modelling results for mafic magmas (SiO_2 < 52%; Mg# > 63) from the SCN, using La as a reference element (the most highly incompatible element).

Elem	$(C^{La} - C^i)_E$ diagram							$(C^{La} - C^{La}/C^i)_E$ diagram					
(i)	*n*	m^i	se_{mi}	I^i	se_{Ii}	*r*	$P_{c(r,n)}$	m^i	se_{mi}	I^i	se_{Ii}	*r*	$P_{c(r,n)}$
Ce	24	0.78	0.07	4.2	2.5	0.920	< 0.0001	0.0044	0.0024	0.96	0.08	0.358	0.0860
Nd	15	0.55	0.05	1.7	2.0	0.950	< 0.0001	0.0042	0.0039	1.49	0.13	0.284	*0.3044**
Sm	15	0.308	0.044	4.2	1.5	0.891	< 0.0001	0.016	0.006	1.72	0.20	0.625	0.0127
Eu	17	0.196	0.034	5.7	1.2	0.827	< 0.0001	0.034	0.007	1.56	0.22	0.800	< 0.0001
Tb	17	0.158	0.030	3.5	1.0	0.805	< 0.0001	0.040	0.013	2.45	0.44	0.622	0.0080
Yb	15	0.123	0.025	2.3	0.8	0.809	< 0.0001	0.044	0.022	3.7	0.7	0.488	0.0647
Lu	15	0.119	0.031	1.9	1.1	0.724	0.0023	0.053	0.031	4.0	1.0	0.421	0.1178
Ba	26	1.12	0.26	10	9	0.667	0.0002	0.003	0.009	0.63	0.13	0.155	*0.4480**
Hf	14	0.23	0.06	8.2	1.8	0.762	0.0015	0.030	0.007	1.09	0.23	0.765	0.0014
Nb	12	0.45	0.16	14	6	0.660	0.0196	0.017	0.007	0.55	0.25	0.631	0.0277
Rb	23	0.46	0.14	20	5	0.568	0.0047	0.0134	0.0044	0.51	0.16	0.549	0.0066
Sr	26	0.06	0.06	23.7	2.6	0.200	*0.3267**	0.0361	0.0029	0.10	0.09	0.9327	< 0.0001
Ta	14	0.62	0.25	9	8	0.584	0.0283	0.009	0.008	0.86	0.30	0.2542	*0.3806**
Th	14	0.41	0.16	11	5	0.607	0.0214	0.016	0.007	0.81	0.23	0.550	0.0413
U	13	0.80	0.35	8	11	0.570	0.0417	0.0010	0.0013	0.98	0.43	0.010	*0.9689**
Y	24	0.047	0.014	5.5	0.5	0.580	0.0030	0.104	0.010	1.21	0.35	0.910	< 0.0001
Zr	24	0.39	0.06	8.3	2.1	0.806	< 0.0001	0.018	0.005	0.96	0.15	0.632	0.0005
Ti	26	-0.004	0.017	8.8	0.6	0.049	*0.8010**	0.117	0.007	-0.04	0.26	0.955	< 0.0001
P	26	2.7	0.5	39	17	0.732	< 0.0001	0.0024	0.0011	0.186	0.037	0.410	0.0371
K	26	0.60	0.18	39	6	0.561	0.0029	0.0102	0.0017	0.22	0.06	0.783	< 0.0001

n= number of data pairs considered in the trace-element diagrams; m^i= slope of the linear model; I^i= intercept value of the linear model; *r*= correlation coefficient of the linear model; $P_{c(r,n)}$= probability that the variables are not correlated (i.e. 1 - $P_{c(r,n)}$ is the probability that the two variables are correlated); se_{mi}= standard error for slope in $(C^{La} - C^i)_E$ or $(C^{La} - C^{La}/C^i)_E$ diagrams; se_{Ii}= standard error for intercept in $(C^{La} - C^i)_E$ or $(C^{La} - C^{La}/C^i)_E$ diagrams; subscript *E* refers to normalisation with respect to Silicate Earth values. All concentration data are normalised against Silicate Earth values (in $mg.g^{-1}$) by McDonough & Sun (1995): La= 0.648; Ce= 1.675; Pr= 0.254; Nd= 1.250; Sm= 0.406; Eu= 0.154; Gd= 0.544; Tb= 0.099; Dy= 0.674; Ho= 0.149; Er= 0.438; Tm= 0.068; Yb= 0.441; Lu= 0.0675; Ba= 6.600; Cs= 0.021; Hf= 0.283; Nb= 0.658; Pb= 0.150; Rb= 0.600; Sr= 19.9; Ta= 0.037; Th= 0.0795; U= 0.0203; Y= 4.30; Zr= 10.5; Ti= 1205; P= 90; K= 240. Asterisk "*" denotes statistically invalid correlations even at the 95% confidence level (italicized $P_{c(r,n)}$ values).

Appendix A15. Linear regression coefficients for trace-element inverse modelling results for mafic magmas (SiO_2 < 52%; Mg# > 63) from the CAVA, using La as a reference element (the most highly incompatible element).

Elem (*i*)	$(C^{La} - C^i)_E$ diagram							$(C^{La} - C^{La}/C^i)_E$ diagram					
	n	m^i	se_{mi}	I^i	se_{Ii}	*r*	$P_{c(r,n)}$	m^i	se_{mi}	I^i	se_{Ii}	*r*	$P_{c(r,n)}$
Ce	20	0.651	0.026	2.48	0.43	0.986	< 0.0001	0.0133	0.0019	0.900	0.031	0.860	<0.0001
Nd	20	0.440	0.017	3.69	0.27	0.987	< 0.0001	0.0275	0.0028	0.83	0.05	0.920	<0.0001
Sm	20	0.224	0.019	4.37	0.32	0.940	< 0.0001	0.0584	0.0038	0.77	0.06	0.964	<0.0001
Eu	20	0.198	0.014	4.40	0.24	0.955	< 0.0001	0.063	0.005	0.78	0.08	0.948	<0.0001
Gd	20	0.165	0.014	4.52	0.23	0.942	<0.0001	0.073	0.005	0.75	0.08	0.964	<0.0001
Dy	20	0.135	0.015	3.70	0.25	0.904	<0.0001	0.091	0.008	0.90	0.14	0.934	<0.0001
Er	20	0.150	0.017	2.96	0.28	0.904	<0.0001	0.089	0.011	1.19	0.18	0.890	<0.0001
Yb	20	0.100	0.009	2.74	0.15	0.934	< 0.0001	0.120	0.009	1.25	0.15	0.949	<0.0001
Ba	20	0.46	0.28	29	5	0.364	*0.1152**	0.0209	0.0021	0.100	0.035	0.918	0.0111
Cs	12	0.007	0.10	5.8	2.0	0.020	*0.9468**	0.151	0.038	1.3	0.8	0.766	0.1091
Hf	12	0.36	0.05	3.2	0.7	0.928	0.0011	0.036	0.012	1.03	0.19	0.687	0.0135
Nb	20	1.46	0.14	-2.2	2.4	0.922	0.3728	0.008	0.011	1.18	0.19	0.152	*0.5230**
Pb	13	0.31	0.08	9.6	1.5	0.762	0.0020	0.0394	0.0034	0.33	0.07	0.961	0.0005
Rb	20	0.45	0.10	7.8	1.6	0.733	0.0002	0.024	0.005	0.61	0.09	0.698	<0.0001
Sr	20	0.49	0.07	13.9	1.1	0.871	<0.0001	0.0260	0.0015	0.220	0.025	0.970	<0.0001
Th	13	0.60	0.05	1.3	1.0	0.959	0.2549	0.003	0.007	1.44	0.14	0.125	*0.6838**
U	13	0.69	0.18	9.6	3.5	0.756	0.0030	0.014	0.005	0.54	0.10	0.06	0.0184
Y	20	0.198	0.014	2.82	0.24	0.957	<0.0001	0.066	0.009	1.24	0.14	0.873	<0.0001
Zr	19	0.53	0.05	2.07	0.8	0.941	0.0160	0.015	0.012	1.23	0.20	0.301	*0.2098**
Ti	20	0.140	0.026	3.84	0.42	0.788	<0.0001	0.019	0.11	33.0	1.9	0.373	*0.1053**
P	20	2.11	0.07	0.7	1.2	0.989	*0.6057**	0.0001	0.0005	0.484	0.027	0.088	*0.7119**
K	20	3.18	0.16	10.2	2.7	0.977	0.0013	0.0023	0.0008	0.203	0.013	0.576	0.0079

For the explanation of variables and symbols see Appendix A14.